MULTIPHYSICS MODELLING OF OPERATIONAL STRESSES IN A 1.5 T SUPERCONDUCTING MAGNET FOR WHOLE-BODY CLINICAL MRI SCANNER

A Thesis Submitted
in Partial Fulfilment of the Requirements for the
Degree of

DOCTOR OF PHILOSOPHY

by

SANKAR RAM T
(Roll No. 2K17/PhD/ME/09)

Under the Supervision of

Dr. Vijay Gautam
Professor
Department of Mechanical Engineering

Dr. Soumen Kar
Scientist - G
Inter-University Accelerator Centre (IUAC)

to the
Department of Mechanical Engineering
DELHI TECHNOLOGICAL UNIVERSITY
(Formerly Delhi College of Engineering)
Shahbad Daulatpur, Main Bawana Road, Delhi-110042, India

ACKNOWLEDGMENT

This PhD dissertation marks the culmination of a long and challenging journey, and I am deeply grateful to everyone who supported me along the way.

First and foremost, I would like to express my deepest gratitude to my wife, Poornima, for her unwavering love, patience, and encouragement. Your support has been the greatest source of strength for me throughout this journey.

I am equally indebted to my parents, sister, and in-laws, who stood by me through every high and low, offering their constant support and understanding. Your faith in my abilities has been invaluable.

I am profoundly grateful to my supervisor, Prof. Vijay Gautam, and co-supervisor, Dr. Soumen Kar, for their invaluable guidance, wisdom, and patience. Your mentorship has been instrumental in shaping my research and academic growth.

A special tribute goes to my late supervisor, Prof. Vikas Rastogi. Though you are no longer with us, your vision and passion continue to inspire me. I am forever thankful for the foundation you laid during the early stages of my research.

I would also like to extend my sincere thanks to Prof. Arun Kumar Samantaray from IIT Kharagpur, whose development of the software Symbols Shakti and assistance with bond graph modelling was crucial to my work.

My heartfelt thanks go to my gurus in the field of Cryogenics & Superconductivity, Dr. R G Sharma and Dr. T S Datta. Your guidance and expertise have been pivotal in my understanding and growth in this specialized field. I am grateful to my friends and colleagues at Inter University Accelerator Centre, especially Vijay Soni, Navneet Suman, Ajit Nandawadekar, Mukesh Kumar, Suresh Babu, Joby Antony, Manoj Kumar, Rajesh Nirdoshi, and Rajesh Kumar. Your camaraderie and support have been a source of motivation and joy throughout my research.

I would also like to acknowledge the support of the current Director of IUAC, A C Pandey, and the previous Director, D Kanjilal, for their unwavering support of my research endeavours. Finally, I am thankful to the Ministry of Electronics and IT and SAMEER, Mumbai, for providing the financial support that made this research possible.

This thesis is as much a product of your contributions as it is of my own efforts. Thank you all for being an integral part of this journey.

CANDIDATE'S DECLARATION

I, Sankar Ram T, hereby certify that the work which is being presented in the thesis entitled 'Multiphysics Modelling of Operational Stresses in a 1.5 T Superconducting Magnet for Whole-Body Clinical MRI Scanner' in partial fulfilment of the requirements for the award of the Degree of Doctor of Philosophy, submitted in the Department of Mechanical Engineering of Delhi Technological University is an authentic record of my own work carried out during the period from Aug 2017 to Nov 2023 under the supervision of Prof. Vijay Gautam and Dr Soumen Kar.

The matter presented in the thesis has not been submitted by me for the award of any other degree of this or any other institute.

Candidate's Signature

This is to certify that the student has incorporated all the corrections suggested by the examiners in the thesis and the statement made by the candidate is correct to the best of our knowledge.

Signatures of Supervisors

Signature of External Examiner

Date:

CERTIFICATE BY THE SUPERVISORS

Certified that Sankar Ram T (Roll No. 2K17/PhD/ME/09) has carried out their research work presented in this thesis entitled 'Multiphysics Modelling of Operational Stresses in a 1.5 T Superconducting Magnet for Whole-Body Clinical MRI Scanner' for the award of Doctor of Philosophy from Department of Mechanical Engineering, Delhi Technological University, Delhi, under our supervision. The thesis embodies results of original work, and studies are carried out by the student himself and the contents of the thesis do not form the basis for the award of any other degree to the candidate or to anybody else from this or any other university/institution.

Dr. Vijay Gautam
Professor
Department of Mechanical Engineering
Delhi Technological University

Dr. Soumen Kar
Scientist - G
Inter-University
Accelerator Centre (IUAC)

Date:

ABSTRACT

Ministry of Electronics and Information Technology (MeitY), Government of India, has initiated a project to develop a 1.5 T superconducting MRI scanner in India. Inter- University Accelerator Centre (IUAC), New Delhi, is primarily responsible for the development of a 1.5 T superconducting magnet and an ever-cooled cryostat for the MRI scanner. An actively shielded 1.5 T superconducting MRI magnet has been designed for a whole-body clinical scanner. The MRI magnet generates a 1.5 T magnetic field in a 45 cm Diametrical Spherical Volume (DSV) with ±5.5 ppm homogeneity. The magnet has been wound by using braided polyethylene terephthalate (PET) insulated wire in channel (WIC) Niobium Titanium (Nb-Ti) (low-temperature superconductor) wire on the bobbin. MRI magnet operates at 4.2 K (liquid helium) temperature, and its operating current is 420 A.

Through this thesis, the operational stress and its effects on the magnetic field quality of the 1.5 T MRI magnet are studied. This includes the effects of Lorentz forces, cooldown to a cryogenic temperature of 4.2 K, and the winding tension experienced during the magnet winding process.

Initially, the composite material properties of the magnet are calculated to simplify the calculation. This allows the assumption that the magnet coils are a single homogeneous material instead of a composite made up of multiple materials. This is achieved by calculating the speared properties of a Representative Volume Element (RVE). Further, an analytical model is created to calculate the magnetic field, and based on the magnetic field values, the Lorentz forces are applied to the magnet. This information, along with the thermal boundary conditions and winding tension, is used to create a computational model to calculate the operational stresses in the magnet. In order to simulate the winding tension, a code is developed in APDL that utilizes initial stress states and the Element Death and Birth method.

Using the models, the design of the magnet is optimised for the required state of stress. The winding tension, number of layers of over-bind, and over-bind tension are taken as variable parameters and are used to compensate for the effect of Lorentz forces and thermal stresses. Through simulation, the final state of stress is identified, and the deformations of the coil due to various forces are calculated. This information is then used to calculate out the final field quality and variation in field homogeneity from the design.

By utilising a bond graph, a multi-physics model is created to study the operation of the superconducting magnet during an emergency shutdown/quench. The model constitutes two domains, i.e. thermal and electrical. The thermal domain looks at the thermal propagation of heat generated during the process and the associated quench propagation. In contrast, the electrical domain looks at the current flow in the circuit and the effect of various quench protection systems. The electrical domain is modelled using a pure bond graph, while the thermal domain is modelled as a pseudo bond graph. The model is then used to simulate the quench in a 6 T solenoid magnet, and the results are compared with the commercial software OPERA and experimental results.

LIST OF PUBLICATIONS

i. S R Thekkethil, S Kar, V Rastogi, (2023), "*Multi-physics modelling of quench in a superconducting magnet using bond graph*," Physica C: Superconductivity and its Applications, vol. 604, p. 1354179

ii. S R Thekkethil, V Rastogi, S Kar, (2023), "*Multiphysics Stress Analysis of a 1.5 T Superconducting MRI Magnet*," Journal of Superconductivity and Novel Magnetism, vol. 36, no. 2, pp. 467–476

iii. S R Thekkethil, V Rastogi, S Kar, (2022), "*Effect of Thermal Strain, Induced by Cryogenic Cooling, on a High Homogeneity Superconducting Magnet for MRI Applications*," Indian Journal of Engineering and Materials Sciences (IJEMS), vol. 29, no. 5, pp. 581–585

iv. S R Thekkethil, S Kar, M Kumar, V Soni, N K Suman, R G Sharma, V Rastogi, T S Datta (2018), "*Stress-Induced Magnetic Field Inhomogeneity in a 1.5 T Superconducting MRI Magnet*," IEEE Transactions on Applied Superconductivity, vol. 28, no. 4, pp. 1–5

v. S R Thekkethil, V Rastogi, N Suman, V Soni, A Nandawadekar, R G Sharma, T S Datta, S Kar, (2020), "*Multiphysics analysis of operational stresses in a 1.5 T MRI magnet*," Indian Journal of Cryogenics, vol. 45, no. 1, pp. 154–159,

vi. S R Thekkethil, S Kar, N Suman, M Kumar, V Soni, R G Sharma, T S Datta, (2018), "*Analysis of mechanical stress due to winding pretension in a 1.5T superconducting MRI magnet*," Indian Journal of Cryogenics, vol. 43, no. 1, p. 187

CONFERENCE PRESENTATIONS

i. S R Thekkethil, S Kar, M Kumar, V Soni, N K Suman, R G Sharma, R Harsh, T S Datta, "*Analysis of 3D-stress in a 1.5 T superconducting MRI magnet"*, National Symposium on Cryogenics and Superconductivity (NSCS-26), Variable Energy Cyclotron Centre, Kolkata (2017)

ii. S R Thekkethil, M Kumar, V Soni, N K Suman, R G Sharma, T S Datta, S Kar, "*Stress induced magnetic field in-homogeneity in a 1.5T superconducting MRI magnet"*, 13th European Conference on Applied Superconductivity, EUCAS , CERN, Geneva (2017)

iii. S R Thekkethil, S Kar, V Rastogi, N K Suman, V Soni, R G Sharma, T S Datta, "*Multi-physics Analysis of Operational Stresses in 1.5T MRI Magnet",* National Symposium on Cryogenics and Superconductivity (NSCS-27), IIT Bombay, Mumbai (2019)

iv. S R Thekkethil, S Kar, V Rastogi, "*Bond Graph Modelling of Quench in a Superconducting Magnet",* International Conference on Trends & Advances in Mechanical Engineering, J.C Bose University of Science and Technology, YMCA, Faridabad (2021)

v. S R Thekkethil, S Kar, V Rastogi, "*Bond graph as a tool for modelling superconducting magnet quench",* International Conference on Aerospace and Mechanical Engineering ICAME'21, TKM College of Engineering, Kerala (2021)

TABLE OF CONTENTS

LIST OF FIGURES

LIST OF TABLES

LIST OF SYMBOLS, ABBREVIATIONS AND NOMENCLATURE

- APDL - Ansys Programming Development Language
- Cu:SC ratio - Copper to superconductor ratio
- CICC - Cable in Conduit Conductor
- DSV - Diametrical Spherical Volume
- EM Forces – Electromagnetic Forces/Lorentz Forces
- FDA - Food and Drug Authority
- FEA - Finite Element Method
- FFT - Fast Fourier Transform
- FOV - Field of View
- HTS - High Temperature Superconductor
- IUAC - Inter-university Accelerator Centre
- LTS - Low Temperature Superconductor
- MgB_2 - Magnesium diboride
- MeitY - Ministry of Electronics and Information Technology
- MICE - International Muon Ionization Cooling Experiment
- MRI - Magnetic Resonance Imaging
- Nb-Ti - Niobium Titanium
- Nb_3Sn - Niobium Tin
- NMR - Nuclear Magnetic Resonance
- OFHC - Oxygen Free High Conductivity
- PCS - Persistent Current Switch
- PET - Polyethylene Terephthalate
- QPS - Quench Protection System
- ReBCO - Rare-earth Barium Copper Oxide
- RF- Radio Frequency
- RT – Room Temperature (300 K)
- RVE - Representative Volume Element
- SE - Source of Effort
- SF - Source of Flow
- SMES - Superconducting Magnetic Energy Storage
- SNR - Signal to Noise Ratio
- VPI - Vacuum Pressure Impregnation
- WIC - Wire in Channel
- YBCO - Yttrium Barium Copper Oxide
- ZBO System - Zero Boil Off System

- ω/ω_0 - Larmour frequency (Hz)
- γ - proton gyromagnetic ratio (Hz/T)
- B_z - Magnetic field on Z axis (T)
- T_C - Critical temperature (K)
- B_C - Critical field (T)
- J_C - Critical current density (A/m2)
- B_{max} - Maximum magnetic field (T)
- B_0 – Central magnetic field (T)
- L – Inductance (H)
- I – Current (A)
- J – Current Density (A/m^2)
- B_x, B_y, B_z - Components of the magnetic field vector (T)
- K(k) - the complete elliptic integral function, of the first kind
- E(k) - complete elliptic integral function, of the second kind
- a - radius of the loop
- μ_0 - permeability constant ($4\pi \times 10^{-7}$)
- x - distance in the axial direction from the centre of the current loop to the field measurement point.
- r - distance in the radial direction from the axis of the current loop to the field measurement point.
- P_n^m - Legendre polynomials,
- A_n^m, B_n^m - harmonic coefficients in the Spherical Series expansion
- F_L - Lorentz Force Density (N/m^3)
- f_L – Net Lorentz force
- σ_θ – Hoop Stress (MPa)
- C_p – Specific heat capacity (J/kg K)
- M - Mass of the body (kg)
- t - Temperature (K)
- f – flow
- e- effort

CHAPTER 1

INTRODUCTION

1.1 MRI Scanner

Magnetic resonance imaging (MRI) is based on the concepts of nuclear magnetic resonance (NMR) principles, where an atomic nucleus aligns with a strong axial magnetic field. In case of MRI, it is the proton, i.e. hydrogen nuclei found in abundance in the human body as water. In the background magnetic field B_0 created by the magnet, protons in the body tissues tend to align with the field, creating a net magnetic moment proportional to B_0 (Figure 1.1).

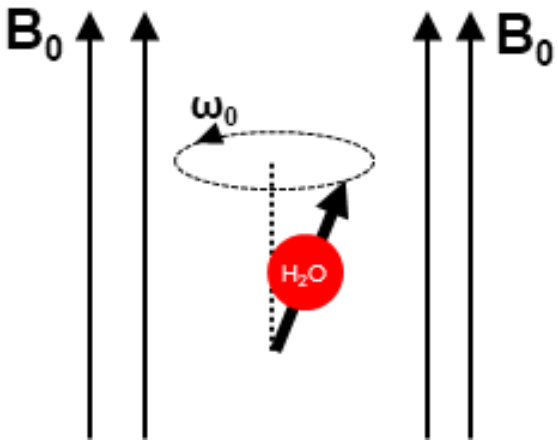

Figure 1.1 Precession of proton (^{1}H) in the presence of magnetic field. The frequency of precession (ω_0) is called the Larmour frequency.

When a radio frequency (RF) pulse of a specific resonant frequency is sent by the RF coil located in the magnet bore, the magnetised protons absorb the energy. This energy will cause the proton to move to a high-energy state by absorbing RF waves of Larmour frequency. The net magnetisation vector of the proton, which is now precessing at Larmour frequency (ω_0) is given by [1]

$$\omega_0 = \gamma B_0 \tag{1.1}$$

where, γ the proton gyromagnetic ratio for proton (^{1}H) is 42.576 MHz/T. The proton then relaxes back to its original state by emitting the absorbed energy, producing a detectable signal. These RF signals that are released back are measured and processed to allow an image to be created. This is achieved by runnning a Fast Fourier Transform (FFT) analysis of the frequencies emitted by resonating atoms comprising cell structures. Various tissues have distinct relaxation characteristics, which is an attribute that is utilized to produce contrast in images. Reconstructing an image involves picking up the resonate signal that the rotational magnetization vector emits using a receiver coil. To achieve spatial encoding, an array of X, Y, and Z gradient coils are placed inside the superconducting magnet's bore and the pulsed intermittently. They provide linear variation in the resonant frequency (ω_0) throughout the field of view (FOV) by overlaying a linearly varying field on top of the uniform background field (B_0) generated by the primary magnet. The received radio frequency

signal is then transformed into a picture using the Fast Fourier Transform (FFT) technique. Hence, by using a strong magnetic field and RF waves, cross-sectional pictures of any desired plane inside the human body can be taken. An extraordinary resolution of soft tissue is achieved without subjecting the patient to ionising radiation. MRI images have become a vital diagnostic tool for the detection and analysis of disease through the non-evasive magnetic field. It is especially effective for imaging tissues, such as in the head, spine and joints which are obstructed by bone since the contrast provided by the shadow-gram of x-rays is reduced because bone attenuates radiation considerably more than tissue does. In contrast to x-rays, which carry the risk of damaging human cells, MRI allows the physician to safely view the inside of the human body in 3D with high resolution imaging, various soft-tissue contrast mechanisms and as functional processes [1].

The field strength has to be extremely stable very uniform in the imaging volume both spatially and temporally. This is typically the cross-section of the human body, with spherical volume around 45 to 50 cm diameter at the centre of the magnet. The needed resolution, gradient coil power, acquisition duration, and resonance frequency determine the background field's volume, size, spatial homogeneity, and temporal stability. Hence, one of the essential requirements for a whole-body MRI scanner is stringent homogeneity, typically in the range of 10 ppm peak-to-peak over a large volume of 45-50 cm FOV. High inhomogeneity will interfere with the linear gradient field and thus distort the spatial information within the scan volume and degrade the image quality. The temporal stability of the field must at least be equal to the homogeneity during the period of image acquisition.

The quality of the image is directly dependent on the magnetic field strength. A field strength of more than 1 T can only be achieved practically through the use of superconducting magnets. Superconducting magnet technology has always been the limiting element in high-field MRI. The difficulty for magent designers has been to take care of magnet weight, cost, and stray fields while maintaining patient

access, temporal stability, and spatial homogeneity while increasing the field strength feasible with a large bore magnet.

Following the discovery of Nb-Ti alloy, the first superconducting magnets of practical use were built in the 1960s. However, the scientific laboratory to everyday use of superconductivity startted with the invention of Magnetic Resonance Imaging (MRI). MRI has transformed superconductivity from a scientific phenomenon to a technology a that improves people's lives.

1.2 Specification of MRI Magnet

High image quality during MRI requires stringent requirements regarding the performance of the superconducting magnet. The primary requirements are listed below [2], [3].

a. **Field strength (B_0):** The image resolution is directly proportional to the field strength because of the enhanced signal-to-noise ratio (SNR). Also, higher field strengths ensure lower scan times. Hence, higher magnetic field strengths are preferred despite the technical challenges.
b. **Imaging volume:** The larger the imaging volume, the better. However, a trade-off is required owing to the increased cost. The need for the high-performance gradient and RF-system, as well as the passive shim and covers, translates a patient bore with a 60 or 70 cm diameter into a typical warm bore diameter of the magnet of 85-95 cm. The diameter of maximum imaging volume (FOV) will be around half of the diameter of the magnet bore for a 1.5 m long magnet.
c. **Field homogeneity:** The higher the field uniformity, the clearer the scanned image. Typically, an inhomogeneity of up to 10 ppm peak-to-peak of the background field (B_0) within 45-50 cm FOV is permissible. For particular

imaging procedures, the surfaces of the smaller dimension and higher homogeneities may be specified.

d. **Long-term field stability:** The MRI magnet requires long-term stability in the central field (B_0). The temporal stability should be better than 0.1 ppm/hr, which is 0.09% per year. This order of stability will eliminate any further recharging of the magnet to restore the frequency in operating bandwidth. The desired order of the temporal stability is an order of magnitude higher than modern high-current power supplies can provide. Hence, the commercial MRI system is operated in persistent mode.
e. **Stray field shielding:** One of the most critical requirements for any MRI scanner is the 5 G stray footprint in maximum 5 m (axial) x 3 m (radial) elliptical region for safety reasons. This requirement is defined based on the Food and Drug Authority (FDA) regulations on medical equipment.
f. **Cryogenic cooling:** An ideal MRI magnet system needs minimum servicing. The cryogenic system of the MRI should be completely invisible to the user. The cryocooler-based Helium re-condensation technology has enabled minimising the Helium re-filling frequency and making it a zero-boil-off (ZBO) system.
g. **Reliability:** The MRI magnet system must be rugged, reliable, safe and fully self-protected. All the critical parameters of the magnet need to be monitored and logged continuously to report any abnormal situation. There should be an emergency shutdown mechanism which enables quick discharging of the magnet if necessary.
h. **Weight:** One of the driving parameters for cost reduction of an MRI machine is the metallic weight of the machine. Hence, the future technology is moving for lower and lower weight of the system for ease in transportation, installation in the site, etc. This is dependent on the design of each and every component that contributes towards the overall weight of the design.

The crossection view of a typical MRI magnet system incuding the cryostat and other ancillaries in

Figure 1.2. It can be seen the major componenet in the whole assembly is the magnet formed by the magnet coils and the bobbin.

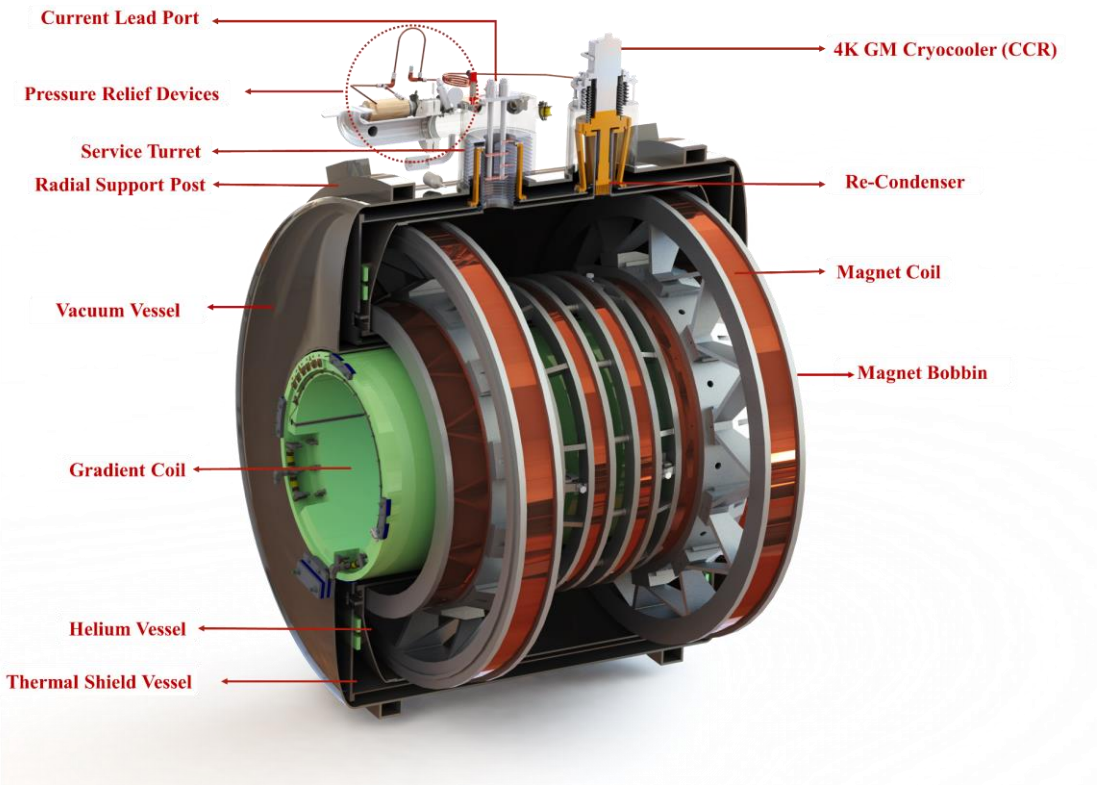

Figure 1.2 Crossection view of a typical MRI magnet system incuding the cryostat and other ancillaries.

1.3 Superconductivity

Superconductivity is defined as the complete disappearance of electrical resistance in materials when they are cooled below a characteristic temperature. This phenomenon was first observed in mercury below 4.2 K by K. Onnes in 1911[2]. This temperature, called the transition or critical temperature, varies for different materials but is generally below 25 K (-248 °C) for practical superconductors. Recent studies have discovered High Temperature Superconductors (HTS) that have a higher transition temperature and thus, the classical superconductors were termed Low-Temperature Superconductors (LTS). The general trend of resistance vs. temperature of LTS (Nb-Ti) and HTS (YBCO) compared to copper is shown in Figure 1.3 [3]–[6].

Note that in the normal state, i.e., above the critical temperature, the resistivity of the superconductors is much higher than that of copper.

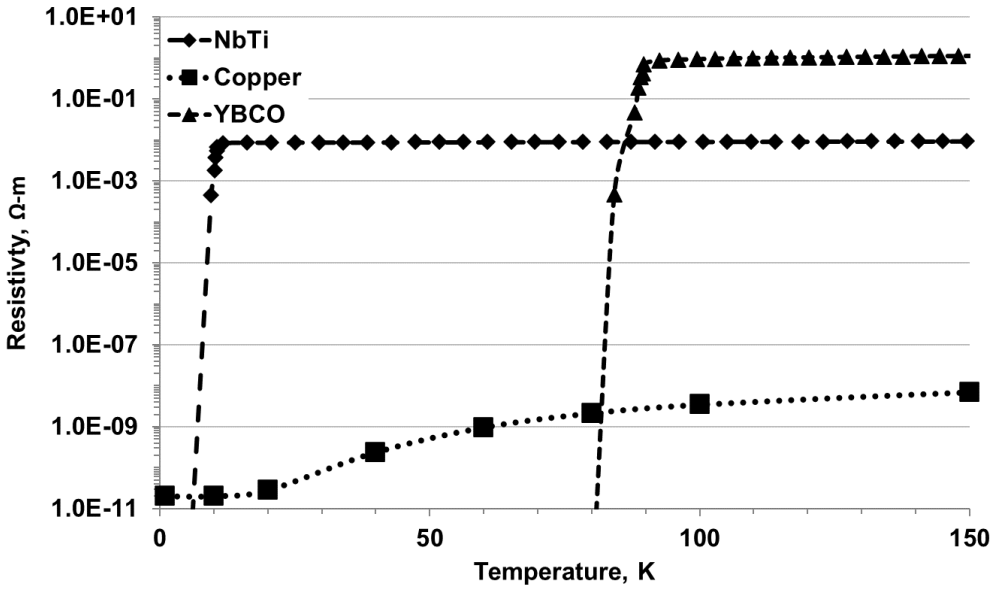

Figure 1.3 Typical Temperature vs. Resistance behaviour of Low-temperature Superconductors (LTS) (Nb-Ti), High-temperature superconductors (HTS) (YBCO) and copper.

The use of superconductors in magnets is limited by the fact that strong magnetic fields above the critical magnetic field (B_c) cause a superconductor to revert to its normal (resistive) state, even though the material is kept well below the transition temperature. This sudden transition in a magnet can lead to the magnet quenching. This increase in the magnetic field may be either externally produced or self-field produced due to the current flowing.

This limits the maximum current that a superconductor can bear, which is called Critical Current (I_c). Because of these limitations, though a plethora of materials exhibits superconductivity, a handful of them are suitable for magnet applications and are termed ‘Practical Superconductors’. The evolution of superconductor technology is shown in Figure 1.4 (Adapted from [7], [8]).

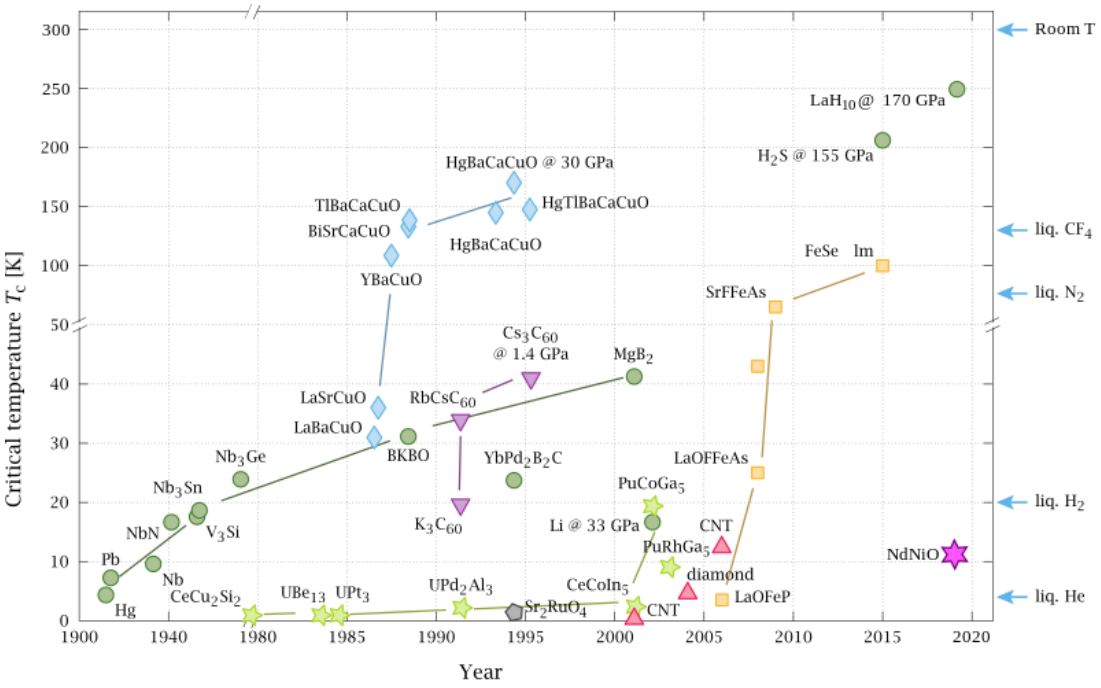

Figure 1.4 The development of some of the superconducting compounds identified. Additionally take note of the axes switch around at 1980 and T_c = 50 K.

1.4 Critical Surfaces of Nb-Ti

The superconductor's critical temperature (T_c) is interdependent on the conductor's current density (J) and the magnetic field (B) acting upon it. The three crucial parameters are interlinked through three-dimensional surface known as critical surface. The boundaries of the critical current density (J_c), critical temperature (T_c), and critical field (B_c) define these surfaces in a 3D B-J-T space. Provided three critical parameters: temperature, magnetic field and current density, all stay within the characteristic critical surface, shown in the Figure 1.5, a typical superconductor such as Nb-Ti would remain in the superconducting state [8].

When these parameters are within their critical values, the superconductor exhibits zero electrical resistance, effectively allowing the flow of electric current without energy loss. The interplay between these factors is delicate; exceeding any of the critical values—whether it be the temperature, magnetic field, or current density—can push the material out of the superconducting state and into a normal resistive state. This transition underscores the importance of maintaining these parameters within the critical surface to ensure the superconductor remains in its superconducting phase.

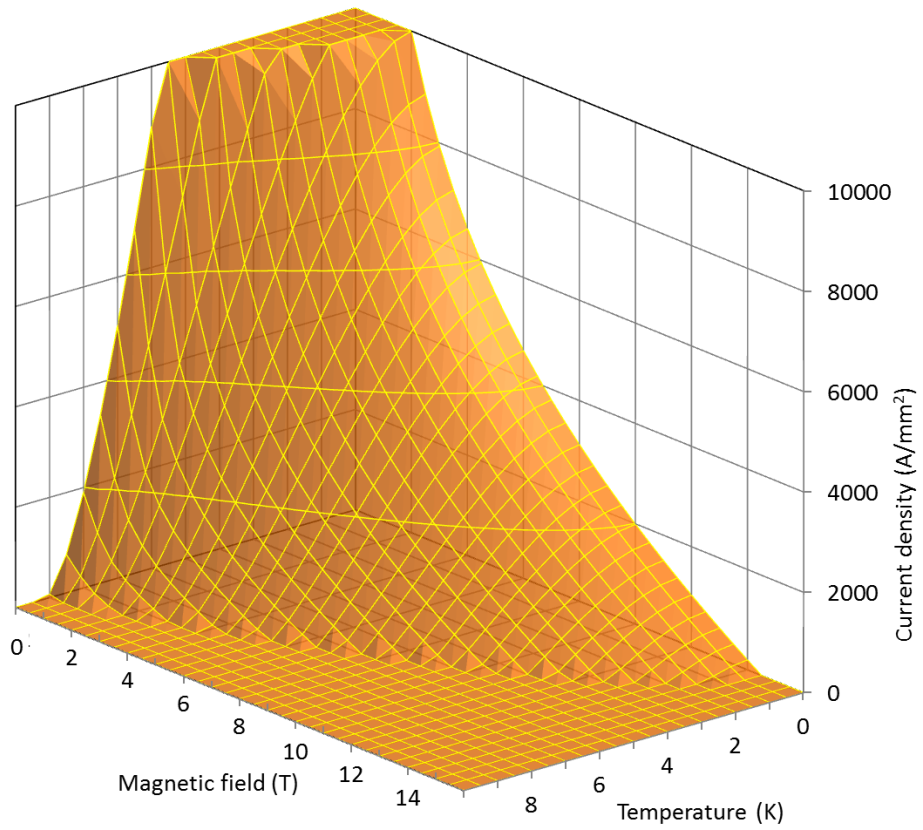

Figure 1.5 Critical surface of a Low-Temperature Superconductor. The three critical parameters, Critical Current, Critical Magnetic Field, and Critical Temperature, are interdependent and form the critical surface.

Figure 1.6 describes the mutual relationship between the critical temperature (*Tc*), critical field (*Bc*), and critical current density (*Jc*) for Nb-Ti superconductor. The alloy composition and the inherent physical properties of the superconducting material define the baseline of the critical surface, which describes the relation between B_c and T_c at zero current. The values of T_c and B_c are 9.2 K and 14.5 T, respectively for a practical Nb-Ti superconductor. Figure 1.6 also shows the intersection between the planes of $J_c - B_c$ at 4.2 K and the $J_c - T_c$ plane at 6 T magnetic field. The intersecting line (AB) would be helpful in choosing the operating current for a 6 T Nb-Ti magnet at 4.2 K, which eventually corresponds to the operational load line of a 6 T Nb-Ti magnet. This would also determine its current margin during the operation of the magnet.

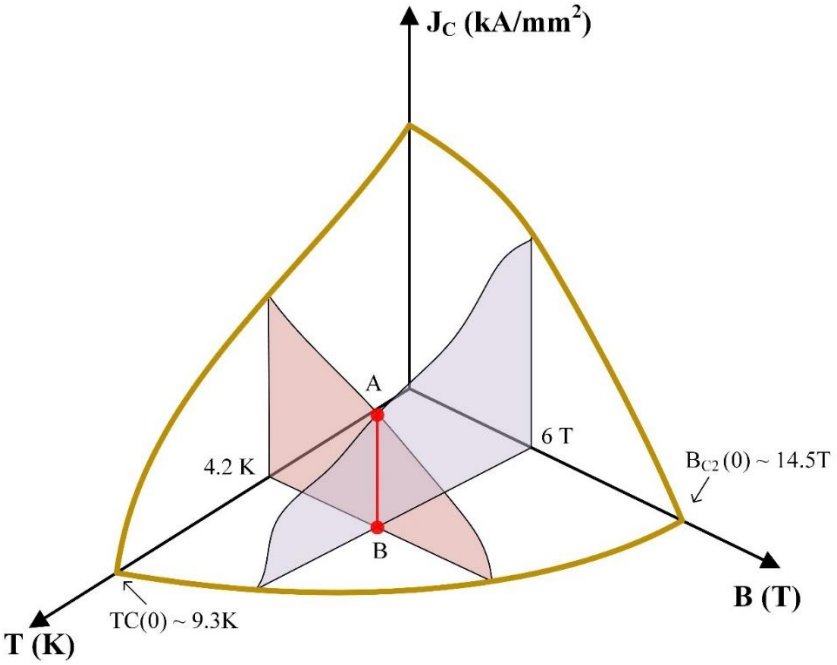

Figure 1.6 Current sharing temperature & thermal margin in a typical Nb-Ti Superconductor wire at a specified magnetic field (6 T) and temperature (4.2K).

1.5 Superconducting Wire

In most applications, the bulk superconductor is not of great use on its own. Because of their low electrical conductivity and poor thermal conductivity in their normal state, all superconductors experience thermal and electromagnetic instabilities. Superconducting magnets erratically quench as the consequence of these instabilities. Practical superconductors are created as tiny filaments placed in a high conductivity OFHC copper matrix in order to get around this issue. The most popular superconductor, Nb-Ti, had been produced this way by co-processing it with copper and used universally up to a field of 9 T. Significant advancements in production techniques have been developed in order to meet the demanding requirements of high *Jc* and low AC losses for accelerator and fusion reactor magnets. It has been possible to construct conductors with fine filaments (less than 1 μm), covered in diffusion barriers, low filament spacing to dia. ratio (less than 0.15), a resistive matrix to lessen filament coupling, and a low copper content. Rutherford and CICC (cable-in-conduit conductor) configuration big J_c conductors with a current of around 50 kA have also

been developed [9]. The critical current density vs. applied field for most common superconducting wires is shown in Figure 1.7 [10]. The different fabrication techniques used by various manufacturers provide wires of varying characteristics for a given superconductor. It may be noted that though Nb-Ti exhibits low I_c and B_c, it is the workhorse of some of the modern magnet systems due to its superior mechanical strength, ductility and well-established electrical characteristics.

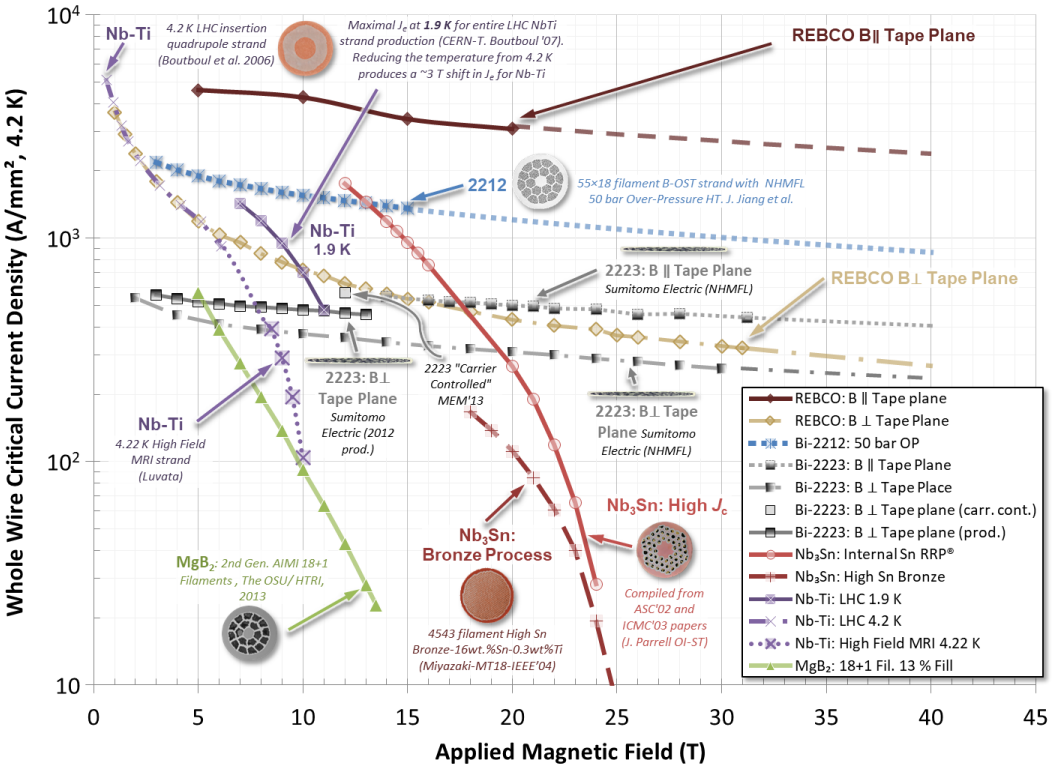

Figure 1.7 Critical Current vs. applied field for some of the superconducting cables used worldwide.

For MRI applications, various types of superconducting wires are used. The most common are round wire, rectangular monolith wire and Wire in Channel (WIC) conductor (Figure 1.8) (Courtesy WST - Western Superconducting Technologies Co., Ltd). Out of these, the most practical is WIC conductors since they have the advantages such as high strength, high packing factor, good mechanical strength, etc. The WIC conductor will have a copper to supercondutor (SC) ratio of 9:1 to 12:1. The critical current will in the range of 760 A.

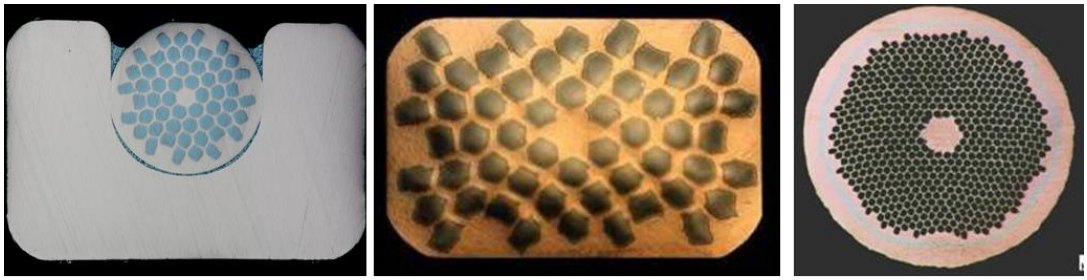

Figure 1.8 Most common superconducting wires used for MRI coils construction. In all cases, the superconductor (Nb-Ti) filaments are embedded in a copper matrix. (a) Wire in Channel (WIC) conductor, (b) Rectangular monolith conductor and (c) Round monolith conductor.

1.6 Quench of Superconducting Magnet

Quench is one of the crucial transient phenomena for any superconducting magnet. During a quench, one or more of the critical parameters (*J*, *T*, *B*) rise above their critical values, and the coils become normal. This increase in resistance causes Ohmic losses (I^2R losses), which generate heat at that point. The heat further quenches the neighbouring areas, spreading or propagating the quench. This process continues until all the stored energy is dissipated. The stored energy (*E*) in a magnet is given by the equation,

$$E = \frac{1}{2}LI^2 \tag{1.2}$$

where, *L* is the inductance of the magnet and *I* is the operating current. For an MRI magnet, quench is more crucial as the total stored energy is of the order of a few mega Joules [7]. During a quench, the entire stored energy will be either partially dissipated through dump resistors or adiabatically deposited on the coils, resulting in the rise of temperature in the magnet. Without proper protection, the magnet can be damaged in a quench. Hence, designing an efficient quench protection system for the MRI magnet is very crucial. A simple magnet system circuit, along with a Quench Protection System (QPS) and power supply, is shown in Figure 1.9. The Persistent Current Switch (PCS), being a superconductor, shortens the current leads from the

power supply, creating a closed loop for the magnet to run in persistent mode. Thus, the magnet current running in a full superconducting loop can theoretically be sustained without losses. In practice, however, there are small energy losses due to the resistance of superconducting joints, and the magnet current needs to be topped up every two to three years. The quench behaviour of the MRI magnet needs to be properly simulated to avoid any damage during a quench.

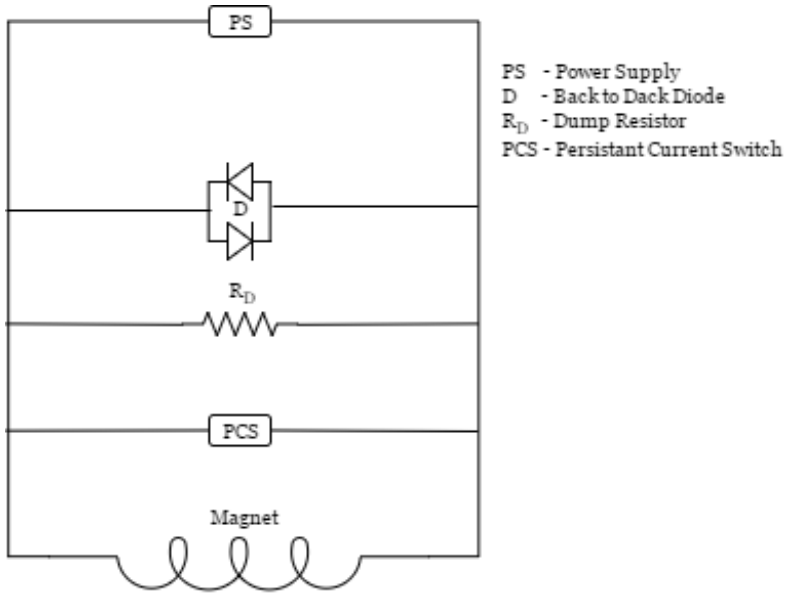

Figure 1.9 Circuit of a single coil superconducting magnet along with Quench Protection System (QPS) and power supply.

1.7 Bond Graph

Bond graphs are visual representations of power exchange between the system's basic elements and its subsystems. The most essential dynamic aspects of the system must be maintained in the focus when creating this graphical system. In this method, a physical system can be represented by symbols and lines, and the routes of power flow can be identified. Bonds and junctions connect the lumped parameter elements of resistance, capacitance, and inertance while obeying the overall energy conservation principles, resulting in a network structure. The derivation of system equations from the graphical representation of the bond network is so systematic that it may be automated using step-by-step algorithms.

The bond graph technique, developed by H. Paynter [11] in 1961, provides a generalised foundation for describing power-continuous models of multi-physical systems. Later, D. Karnopp, D. Margolis, and R. Rosenberg developed the notion into a physical systems modelling methodology that is now utilised by many researchers across the world in academia and industry[12], [13]. An early promoter, among others, of the new modelling technique was developed by J. Thoma [14]. In his PhD thesis [15], J. Granda developed a bond graph pre-processor that transformed the line code into equations for input into widely used simulation programs and then replaced the line code entry with a graphical editor.

The framework is built around bonds that carry two variables: flow and effort. The power exchange in each bond is described as the product of the flow and effort variables. As a result, the flow of energy in a system is represented by a bond graph model. Bond graphs are made up of different elements such as (i) a set of power-conserving structures such as 0 and 1 junctions, transformers, and gyrators; (ii) sources of flow and effort; (iii) energy storage elements; (iv) energy dissipative elements.

1.7.1 Power Variables of Bond Graphs

The concept of bond graphs aims to express physical systems through the exchange of power. The power in a bond graph is expressed as the product of a pair of conjugate variables, effort (e) and flow (f). When considering various physical domains, these power variables, i.e. effort and flow, have different interpretations. However, power can always be used as a common medium to model coupled systems residing in multiple energy domains.

For example, a system may be considered where a water-cooled engine running on fuel turns a generator to produce electricity. It can be seen in such a system the form of energy changes throughout the path of energy flow. However, the system may be split into multiple domains interacting with each other, such that each domain deals with only a single form of energy. Power variables of bond graphs may not always be realizable on non-physical domains and pseudo-bond graphs. These may encounter fictional power such as in bond graphs for economic systems. In the following table, effort and flow variables in some physical domains are listed in Table 1.1 [16].

Table 1.1 Power variables in a bond graph system for various physical and pseudo physical domains.

	Effort e	**Flow** f	**Momentum** $P = \int e$	**Displacement** $Q = \int f$
Electrical	Voltage	Current	Flux Density	Charge
Mechanical Linear	Force	Velocity	Momentum	Displacement
Mechanical Rotational	Torque	Angular Velocity	Angular Momentum	Angular Displacement
Thermal	Temperature	Entropy Flow	-	Entropy
Pseudo Thermal[1]	Temperature	Heat flow	-	Energy
Chemical	Chemical potential	Molar flow	-	Molar mass
Economics	Unit price	Flow of orders	Economic Momentum	Accumulation of order
Magnetic	Magnetomotive force	Magnetic flux rate	-	Magnetic Flux
Hydraulic	Total pressure	Volume flow	Pressure momentum	Volume

Table 1.1 adds two more physical quantities to the bond graph modelling equations. They are the two energy variables known as generalised momentum (P) and generalised displacement (Q), and they are calculated by integrating the power variables across time. The concepts of generalised momentum and generalised displacement have been used in bond graph modelling since the beginning. When solving the bond graph model, an iterative method is used to solve for the energy variables as a function of the power variables.

The tetrahedron of state is a graphical representation that describes the relationship between effort and flow. A diagrammatic representation of the tetrahedron of state is shown in Figure 1.10. While the tetrahedron may be modified depending on the energy domain, this form is the generalised representation of variable relationship.

[1] Pseudo thermal bond graphs are not true bond graphs, in the sense that the product of effort and flow doesn't give power. They however are useful as the variable provide more practical sense as the effort and flow are physical measurable quantities.

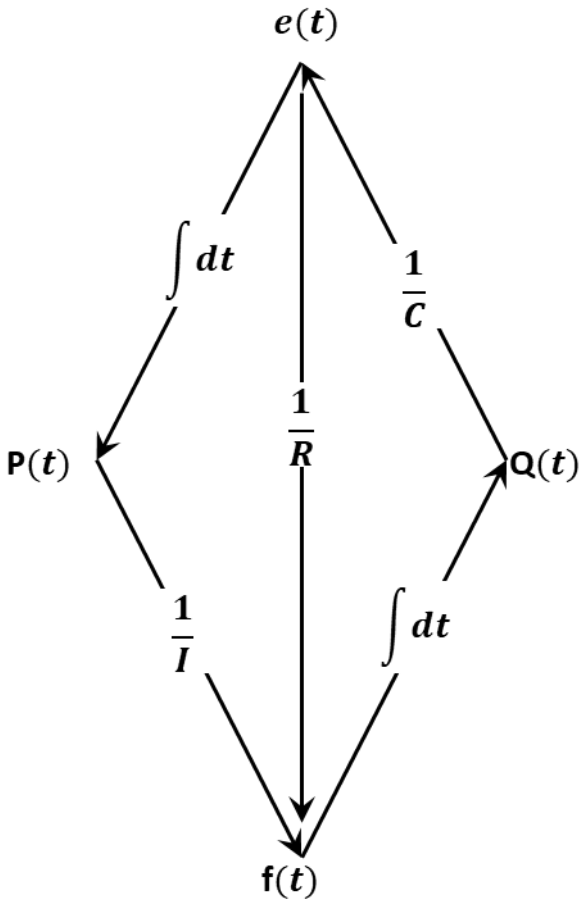

Figure 1.10 The tetrahedron of state defines the relationship between various power variables in the bond graph.

Any variable on the tetrahedron can have a mathematical relationship identified via the tetrahedron of state. To accomplish this, move around the graphic following the arrows and multiply any constants you encounter. For instance, if one wished to determine the link between generalized flow and generalized displacement, they would start with *f(t)* and integrate it to obtain *Q(t).*

1.8 Bond graph standard elements

When designing a bond graph model, one has to choose from the nine basic elements, which can be further grouped into four categories. These are two junction elements, three one-port passive elements, two two-port passive elements and two one-port active elements. Ports are classified as passive or active on the basis of whether

they introduce power into the system. Active elements can add or remove power from the system, while passive elements can only store energy or convert it to another usable form.

1.8.1 One-Port Passive Elements

A one-port passive element has a single power port and power transfer occurs through the port using a single pair of power variables (effort and flow).

1.8.2 R-Element

The one-port resistor is an element in which the effort and flow variables at the single port are related by a linear function. The R-elements dissipate energy. It may be noted that this dissipated energy is not usable within the frame of the model, and thus, the R-element is considered a one-port element. Examples of R-elements include electrical resistors, dampers in mechanical systems, restrictions in fluid flow paths, etc. The bond graph symbol for the resistive element is shown below.

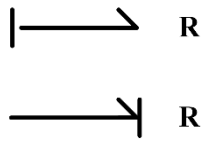

The half arrow pointing towards R denotes that the power, i.e., product of e and f, is positive and flowing into R. The constitutive relationship between e, f and *R* is given by:

$$e = R.f \tag{1.3}$$

$$Power = e.f = R.F^2 \tag{1.4}$$

The movement of energy in an R-element may be dictated by either the flow or the effort variable, and thus, the R-element doesn't have a fixed causality.

1.8.3 C-Element

A one-port C-element is a device which stores energy and can release it without any loss. In the bond graph, the C-element relates the effort to the generalized

displacement. A few examples of C-elements are springs, electrical capacitors, fluid accumulators, etc.

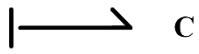

The displacement (Q) and the effort (e) at any moment are given by

$$Q = \int_{-\infty}^{t} f \, dt \tag{1.5}$$

$$e = K \int_{-\infty}^{t} f \, dt \tag{1.6}$$

Here, flow is the cause and displacement (and hence effort) is the consequence.

1.8.4 I-Element

The I-element is the second energy-storing one-port element in which the momentum, *P*, is related to the flow, *f*. The I-element is used to model inductance effects in electrical systems and mass/inertia effects in mechanical or fluid systems. we have;

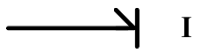

The momentum (*P*) and the flow (*f*) at any moment are given by

$$P = \int_{-\infty}^{t} e \, dt \tag{1.7}$$

$$f = \frac{1}{M} \int_{-\infty}^{t} e \, dt \tag{1.8}$$

Here, effort is the cause and flow (and hence momentum) is the consequence.

1.8.5 One-Port Active Elements

A one-port active element, also called as a source, has a single power port and power transfer occurs through the port using a single pair of power variables (effort and flow).

1.8.6 Source of Effort (SE)

The source of effort provides energy into the system in the form of a defined effort. For example, a force applied to a system, a voltage source, a pressure difference, etc., can be denoted using a source of effort. They are denoted as a half-arrow pointing away from the symbol.

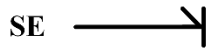

1.8.7 Source of Flow (SF)

The source of flow (SF) provides energy into the system in the form of a defined flow. For example, a velocity applied to a system, a current source, a source with a constant mass flow rate, etc., can be denoted using a source of flow. They are denoted with a half-arrow pointing away from the symbol.

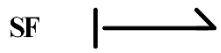

1.8.8 Two-Port Passive Elements

There are two two-port elements: Transformer (TF) and Gyrator (GY). As the name suggests, these elements have two bonds attached to them, and power can flow in and out through either port. These elements do not create, store or destroy energy but scale the power variables such that the net power is conserved, but the effort and flow are changed according to the modulus defined.

The transformer is used widely where the energy exchange doesn't involve multiple domains, such as an electrical transformer, a system of rigid massless levers, etc. A linear relationship can be established between power variables at both ports of the transformer, such as $e_2 = \frac{a}{b}\, e_1$ and $f_2 = \frac{b}{a}\, f_1$ so that finally, $e_1 f_1 = e_2 f_2$. The symbol for the transformer is shown below. The 'm' above the transformer denotes the

modulus of the transformer, which may be a constant or a function, and the arrow represents the direction in which the power flow is assumed.

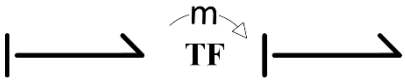

The Gyrator also establishes the power variables relationship, but unlike a transformer, the relation is flow to effort and effort to flow while keeping the net power conserved. Gyrators are used within an energy domain and across multiple domains, and a few examples of a gyrator would be an ideal electrical motor, a gyroscopic wheel, etc. A linear relationship can be established between power variables at both ports of the gyrator such that $e_2 = \frac{b}{a}\, e_1$ and $f_2 = \frac{a}{b}\, f_1$ so that finally, $e_1 f_1 = e_2 f_2$. The 'm' above the transformer denotes the modulus of the gyrator, which may be a constant or a function, and the arrow represents the direction in which the power flow is assumed.

1.8.9 Junction Elements

Junction elements can connect two or more elements through their respective bonds. There are two junctions used in the bond graph: the 1 junction and the 0 junction. They don't have a specific power direction and conserve power across bonds. The generalised equation, eqn (1.9), applies to both junctions.

$$\sum \boldsymbol{e_i f_i = 0} \tag{1.9}$$

The 1-junction is also known as a flow equalizing junction, as $f_1 = f_2 = f_3 = f_4$. This also means, $e_1 + e_2 + e_3 + e_4 = 0$ The 0-junction is also known as an effort equalizing junction, implying $e_1 = e_2 = e_3 = e_4$. Thus, it can be deduced that $f_1 + f_2 + f_3 + f_4 = 0$.

In a bond graph, the elements and bonds are numbered sequentially using integers starting at 1. The bond number also assigns the name of the element or junctions.

1.8.10 Causality

The cause-and-effect connections between the power elements are established by causality. The causal stroke in a bond graph characterizes the inputs and outcomes. The direction of the effort signal is indicated by the causal stroke (i.e., the flow signal is directed towards the end of the bond that does not have a causal stroke). Considering a prime mover with an intelligent speed governor, we can demonstrate the fundamental idea of causality. The load is driven by the prime mover; that is, power is transferred from the prime mover to the load. In addition to providing power, the prime mover determines, based on the governor's setting, what speed the load should run at. Therefore, it can be claimed that flow information that travels to the load is generated by the primary mover. The prime mover receives the torque (effort) information generated by the load and modifies its internal processes to compensate.

The subsequent discussion delves into causal relationships inherent in various storage elements within the world of bond graph theory, specifically focusing on inertance (I) and capacitive (C) types, alongside resistive or dissipative elements.

In the context of inertance elements, the flow (*f*) is intricately tied to the integral of effort (*e*) over time. This fundamental relationship finds practical illustration in physical phenomena such as the acceleration of a mass when subjected to a force.

Conversely, for capacitive elements, effort (*e*) manifests in proportion to the integral of flow (*f*) over time, symbolized by Examples of this dynamic include the charging of a capacitor or the deformation of a spring under the influence of an applied force. Notably, both inertance and capacitive elements exhibit bidirectional relationships between effort and flow, highlighting their dual nature in energy storage and release.

In contrast, resistive or dissipative elements lack a time-integral form of constitutive laws. Instead, their interaction is governed by $f=e/R$ or $e=Rf$, where effort and flow are algebraically linked, permitting varied causal structures within the system.

Expanding upon the conceptual framework, ideal sources within bond graphs, such as the effort source (SE) and flow source (SF), play pivotal roles in enforcing specific dynamics onto systems. The SE imposes effort onto the system, unaffected by flow variations, as exemplified by an electrical cell maintaining terminal voltage irrespective of load fluctuations. Conversely, the SF mandates flow onto the system, disregarding changes in effort, akin to scenarios involving road excitation or constant-displacement hydraulic pumps.

Further nuances emerge in the operational modes of transformers and gyrators within bond graphs. The transformer seamlessly accepts either flow or effort information in one bond and translates it into the other bond, dictated by its elemental relation. On the other hand, the gyrator serves as a conduit for bidirectional conversion between flow and effort across its ports, showcasing its inherent versatility in facilitating energy exchange within dynamic systems. These intricate relationships are encapsulated through constitutive equations, delineating the operational dynamics of these essential components within bond graph theory.

At 1 junction, just one bond, referred to as a strong bond, should carry the flow information; the other bonds should all be stroked. Similar to this, at a 0 junction, all other bonds should be stroked away and just one strong bond should be stroked closer to the junction. The effort at the junction, which the weak links carry around, is determined by this strong bond.

1.8.11 Activated bonds

A bond graph may contain bonds that are merely information carriers. These bonds are not power bonds. Such bonds, where one of the factors of the power is masked, are called activated bonds. For instance, a velocity pick-up only transmits velocity data to the amplifier, which is used by an electromagnetic exciter to apply force on the mass that is proportionate to velocity. The mass is subjected to a reactive force by the exciter, which does not carry the velocity information. Therefore, the force information must be absent on the bond that represents the velocity pick-up and the flow information must be absent on the bond that represents the exciter. On the bonds, a full arrow indicates that some of the data is hidden; the data being transferred may be written close to that full arrow.

The concept of activation is very significant in depicting feedback control systems. Paynter's concept was founded on the observation that an activated bond, while masking the information of a power variable on the other on one end can transfer unlimited power[11]. Further, an effort-activated C-element can measure the summation of flow with respect to time and consequently total flow in a system. In contrast, a flow-activated I-element would measure the generalized momentum and consequently effort. In a bond graph model, activated parts can therefore be thought of as virtual instrumentation since the corresponding terms are absent from the state equations and they have no effect on the dynamics of the system.

CHAPTER 2

LITERATURE REVIEW

2.1 Introduction

An MRI magnet is a complex structure consisting of many parts. Depending on the purpose and design, different materials will be used for the manufacturing of the magnet. Before the discovery of superconductivity (1911) by K. Onnes [69], electromagnets designed were of low magnetic field strength, and electromagnetic stress were not and area of concern. In most cases, the thick wires used to carry the current were enough to contain the Lorentz forces in the magnet. As high magnetic field research started taking more importance, pulsed magnets were used. These magnets didn't have the problem with thermal strains, but the effect of Lorentz forces began emerging. However, mechanical failure due to large EM forces started to become a problem as high-field solenoids started becoming an area of interest.

MRI technology is a closely guarded secret held by companies such as Siemens, General Electric, Philips, etc. Consequently, limited literature is available regarding the development of superconducting magnets for MRI scanners.

2.2 Analytical and Numerical Stress Analysis

The design of high-field superconducting magnets and, thus, higher-stress magnets started in the 1970s. M. Garrett (1963) has published some of the earliest works in the area of stresses in superconducting magnets [17]. He developed methods using a 2-D numerical integration involving elliptic integrals for the calculation of fields, Lorentz forces and inductances of magnets. The method based on this traditional approach was excellent for applications based on superconducting coils and was also extended to cover the case of conductors with a nonrectangular cross-section. S. J. Sackett (1975) later developed a code for the calculation of magnetic fields for coils of arbitrary geometry [18]. The code was later adopted for the commercial program EFFI. While the code took care of both arcs and straight lines, it only took care of electromagnetic (Lorentz) forces. Other conditions like thermal cooldown and winding tension are not considered. D. Melville and P. G. Mattocks (1972) also designed a program for the calculation of stresses in solenoid magnets due to Lorentz forces with different conditions, such as external and internal reinforcements [19]. The program, though designed originally for pulsed-field magnets, are also appropriate for other solenoid coils.

While several scientists had worked on the calculation and design of magnets; most notable of them were V. Arp and J. Caldwell, who had independently published a detailed analytical study of stress in large high-field magnets. V. Arp (1977) analytically calculated various stresses for solenoid magnets which are formed due to winding, cooldown and Lorentz forces [20]. The analytical techniques presented gave a reasonable means for relating anisotropic materials and fabrication parameters to macroscopic stresses and strains in superconducting solenoids. J. Caldwell (1982) obtained a mathematical model representing the stress distribution in magnet windings, but a number of simplifying assumptions were made when deriving the equations [21]. He also checked the accuracy of this method by comparing it with homogeneous thick cylinder theory, which involves the calculation of stresses by solving the Timoshenko stress equations, which were the standard during his time.

C. Minas and L. Salasoo (1991) examined and evaluated the three-dimensional thermal stresses in a solenoidal superconducting magnet using ANSYS FEA [22]. An orthotropic material with three planes of elastic symmetry is used for modelling the superconductor composite, with mechanical properties derived from experimental measurements at 293K and liquid nitrogen temperature adjusted according to the applied temperature range. He concluded that the thermal stresses are not only due to the anisotropic material properties but also due to the fact that more than one material with different properties is used.

In 1980, Oxford Instruments developed the world's first superconducting whole-body MRI magnet. In 1982, Oxford Magnet Technology (OMT) formed as a subsidiary to concentrate on commercial MRI magnet development, and it had done a lot of groundwork research for MRI development. D. G. Hawksworth et al. (1987) and F. J. Davies et al.(1991) published the works at OMT regarding the design of actively shielded superconducting magnets for MRI [23], [24]. They included sets of counter-running coils that cancel out the magnet fringe fields. These works form the basis for the further design of superconducting magnets for MRI scanners, and the same technology is used in modern MRI scanners.

Martin N. Wilson (1982), a key figure in the growth of superconducting technology, published his book on superconducting magnets [25]. His work is still considered one of the most concise and complete guides to superconductor magnet design. His book summarizes the analytical methods used for magnetic field calculation, force calculation and stress analysis of superconducting solenoid magnets. He also lists other technologies associated with the superconducting magnet operation, such as switch design, joint design, instrumentation, etc.

2.3 Material Property Calculation

The calculation of material properties is an essential part of the structural and thermal analysis. The properties for both structural and thermal analysis have to be calculated for the whole operating range of temperatures.

E. Marquardt et al. (2000) presented experimental data on the analysis of materials commonly used in superconducting magnet design [26]. The data was compiled from various published literature and was intended to update the then-outdated NIST material database.

T. Brandsberg (2004) presented details of the calculation of the smeared properties of composite materials for use in the analysis of SMES [27]. The technique involves creating a detailed model of a Representative Volume Element Volume (RVE) that represents the structural details of the various coil pack components and applying known deflections to produce reaction forces. These reaction forces are then used to estimate the multiple terms in the anisotropic property matrix of the composite coil cross-section. J. Chen and X. Jiang (2012) analysed stresses in a 7T superconducting magnet for animal MRI [28]. The epoxy-impregnated composite coils are modeled by the equivalent uniform windings, with their smeared material properties derived by a FEA-based homogenization method. This lowers the computational load by maintaining the mesh sizes within an acceptable level. This method was also applicable to the calculation of orthotropic material properties in epoxy-impregnated magnets.

A. Al Amin et al. (2017) used the method by J. Chen to analyse in detail the stresses in superconducting MRI magnets [29], [30]. They also extended the process to include parameters for thermal analysis, such as thermal conductivity and heat capacity. By creating three-dimensional FEA microstructure models and analysing the outcomes, this concept has been applied to four separate composite superconducting MgB_2 wires in order to extract the material properties of the

homogenized RVE. Comparing the computational homogenization with FEA to analytical methods, the former yields estimations of the material properties that are more accurate since it accurately accounts for the coil composite's geometric complexities. The analysis also makes it possible to take into account the composite wire's orthotropic material behaviour and the requirement for a FEA method in order to precisely estimate orthotropic elasticity.

2.4 Superconducting Magnet Design

K. Pieterman and H. Postma (1984, 1986) designed a 1.5 T MRI magnet for research purposes, and the details of the construction, cooling system and instrumentation were communicated [31], [32]. The papers gave insights into the fabrication of coils, bobbins and support structures.

With the founding of Philips Healthcare in 1891 and GE Healthcare in 1994, the market demand increased the importance of more economical, lighter and smaller systems. Y. Iwasa (1994) started large-scale academic research that was supported by MRI industries. The lab brought a lot of literature and understanding regarding the operation of MRI magnets, and the results were later published in his book [33]. The book, primarily based on actual laboratory and industry magnets, covered in detail the aspects of design and development and introduced the basic design of quench protection, cryostat design, etc.

Recently, the research for the International Muon Ionization Cooling Experiment (MICE) produced detailed literature regarding the practical problems in designing superconducting magnets (2005-2011). The magnetic field range is from 2-5 T at 200-250 A. The major contributors to the work were Michael A. Green and Steve Virostek. Detailed research on the fabrication, assembly, alignment, etc. were published [34]–[39]. The literature based on the MICE magnets gives details regarding which parameters have a direct impact on the magnet operation.

2.5 Superconducting MRI Magnet Design

The ISEULT/INUMAC Whole Body 11.7 T MRI Magnet project (2008-2017), as a collaboration of the University of Freiburg, Siemens Healthcare, Bruker BioSpin GmbH, CEA, France, also published detailed literature regarding the fabrication and winding of MRI magnets [40]–[49]. This is the highest field achieved for an MRI magnet to date. The literature, along with mechanical and thermal analysis, also lists various problems and solutions adopted during manufacturing [50].

Institute of Electrical Engineering, Chinese Academy of Sciences, led by Q. Wang, developed a 9.4 T high field MRI (2012-2017) for research purposes while working closely with industries in the country [51]–[54]. The magnet was not a split-type magnet but a concentric solenoid magnet. The papers cover stress analysis of such superconducting MRI magnets, along with the effect of various parameters, such as winding tension, on the final operational stresses.

H. Miyazaki et al. (2016) designed an HTS (REBCO) based high-field MRI system of a 9.4 T centre field. The paper discussed the design of the magnet coil and the design of the bobbin to withstand the massive Lorentz forces [55]. The paper also discussed AC losses in the magnet that happen during charging/discharging. The work asserted that there is a need to solve problems such as the generation of a stable magnetic field, shimming, and coil protection in order to realize a conduction-cooled 9.4 T MRI magnet. A. Al Amin et al. (2016) designed a 1.5T Superconducting MRI using MgB_2 superconductor [30], [56], [57]. The magnet is designed to be a conduction-cooled magnet operating at a slightly higher temperature of 10 K compared to the normal ‘wet’ magnets operating in a 4.2 K liquid helium bath. The magnet stresses were analysed for operational stresses but without a bobbin structure.

Few researchers also published review papers in the area of MRI magnets. Y. Lvovsky and P. Jarvis (2005) of GE Healthcare presented the basic design of superconducting magnets and specific design criteria for MRI magnet design [3]. They

also discussed current technologies involved and different solutions for the problems. The paper also lists the basic relation between the magnetic field and the geometry of the coils. J. Overweg (2006) of Philips Research also summarised the operation of modern MRI magnets with a brief introduction of each key technological area [58]. The paper gives an overview of the MRI magnet configurations and various ancillaries associated with MRI magnets.

Y. Lvovsky *et al.* (2013) summarised in their detailed review both non-traditional approaches and emerging trends in superconducting magnets for MRI, along with market trends and various cost reduction strategies [59]. The paper discusses the economic and market factors that drive the MRI industry and peaks into the non-traditional configurations, such as open magnets and walk-through magnets, which have emerged recently. The paper also discusses high-field magnets and advanced solutions for future MRI magnets. M. Parizh *et al.* (2017) reviewed recent advances in MRI magnet design, with specific interests in the use of HTS superconductors for MRI magnets [2]. They discussed the feasibility of new conductors that can be used for MRI magnets in terms of characteristics such as stability, conductor shape, ease of handling, insulation, and manufacturability. They concluded that though there are feasible alternatives, new developments need to be made before they can be commercially marketed.

2.6 Magnet Quench Analysis

Quench protection is a crucial task during the design of a superconducting magnet. During a quench, the coil voltages, local temperature, and stress can rise rapidly and damage the magnet. Therefore, to protect the magnet, certain precautions such as heater networks, circuit segmentation, and other conventional techniques are employed. Despite the widespread usage of quench protection systems (QPS) in superconducting magnets, technical information about QPS designs is lacking in the literature. Also, the calculations of quench for large-size magnets can be both time and computationally expensive.

Y. Li and Q. Wang (2012) presented the technical details of a passive quench protection system for a 1.5 T MRI magnet [60]. In this study, a numerical model is designed to simulate the heat conduction from the heater to the winding using the control volume method. With relation to the concerns to the quench time and other variables, various heater designs are compared and analysed. Y. Li *et al.* (2014) later expanded the use of a quench protection circuit to a 9.4 T MRI magnet [61], [62]. Due to the significant energy deposition in order of several mega Joules into the resistors, instead of adiabatic shunt resistors, heaters are used. A quench propagation circuit is also employed to quench the whole magnet in case only one coil is quenched, thus spreading the thermal energy.

R. J. Deissler (2016) presented the results of his work on a simple passive quench protection system for a 1.5 T conduction-cooled MRI magnet. [63], [64] The numerical simulations of the quench propagation and heat flow were performed using second-order finite differencing in the spatial dimensions and a fourth-order Runge Kutta integration in time. The simulations include the behaviour of the critical current as a function of the magnetic field and temperature and the inductive voltages developed as the magnet current decays.

M. Maciejewski and B. Auchmann (2017) presented their ideas on using the Port-Hamiltonian (bond graph) method to model the dynamics that occur during a magnet quench [65]–[67]. The work shows models for different components required for magnet analysis. However, a combined model was not considered, and an application to a practical scenario was not discussed.

2.7 Research Gaps

The development of MRI magnets was mainly constrained to industries or research institutes in close collaboration with the industry. Due to the intellectual property (IP) rights and the level of competition between industries, most of this data is not available in the public domain. The data available are either related to different

types of magnets, does not apply directly to MRI magnets, or are very concise. Thus, developing the models for analysing operational stresses is a crucial step towards the indigenous development of MRI magnets and, thus, MRI scanners. This includes

- Development of analytical models for calculation of Lorentz forces in MRI magnets.
- Simulation effects of various forces in MRI magnet, including Lorentz forces, Thermal Stress and winding tension.
- Study of effects of the stresses in final magnetic field homogeneity.

The quench of a superconducting magnet is an inevitable phenomenon during its operation. Typical simulations of magnet quenches are done using commercial software such as OPERA FEA or ANSYS Maxwell. However, the simulation of quench in a large and complex system such as an MRI magnet will be computationally intensive and take a long time, which is not practical for fast calculation to obtain a ballpark figure. Additional options using system simulation may provide quick results but are not practised widely. Based on the identified gaps, the following objectives have been defined

2.8 Research Objectives

i. To estimate material properties for MRI magnet modelling

The material properties of individual materials and composite properties, wherever required, have to be estimated for the full operating temperature range. Material properties for metals must be taken from literature, while those of non-standard materials, such as insulations, epoxy, etc., have to be obtained from manufacturers directly. The coil cross-section is a composite, and the composite properties have to be calculated wherever necessary. The properties to be estimated include Young's modulus, Poisson's ratio, shear modulus, thermal expansion coefficient, thermal conductivity, electrical resistivity, specific heat, etc.

ii. To develop an analytical framework for the calculation of forces acting on the magnet

The various forces acting on the magnet have to be identified and calculated. These include the Lorentz forces, forces due to thermal stresses, etc. Also,

quantities such as stored energy also have to be calculated. Based on the calculations, winding tension, banding tension, etc., have to be decided, and the forces that are due to those have to be evaluated.

iii. To develop a computational framework for the stress analysis of combined bobbin and coil structure

The bobbin has to be designed for the MRI magnet. The bobbin will bear the axial forces and hold the relative position of the coils. With the bobbin design fixed, the combined operational stresses in the bobbin and coils have to be calculated. If the stresses are beyond the allowable limits, the variable parameters, such as winding tension, etc., must be adjusted to reduce the stresses.

iv. To calculate the effect of coil strain, coil displacements and fabrication tolerances in the final magnetic field quality

The final magnetic field of the magnet has to be calculated and compared to the designed values. The movement of coils will induce some inhomogeneity in the field, which must be calculated. The machining tolerances during fabrication also have to be identified, and their effect on the magnetic field has to be calculated.

v. To develop an analytical model for fast calculation of magnet behaviour during an emergency shutdown.

The emergency shutdown of the MRI magnet is done by quenching a section of the magnet using an installed heater and letting the magnet run its normal quench behaviour. The stored energy of the magnet has to be dissipated through dump resisters as heat energy. The operation of the magnet during this quench has to be studied, as well as various parameters such as peak voltage, temperature rise, and local stresses have to be studied. A bond graph model to explore these would provide a fast and less computationally intensive calculation of the process.

CHAPTER 3

MATERIAL PROPERTY CALCULATION

3.1 Introduction

An MRI magnet is an electromagnet having a complex mechanical structure consisting of many components. Different materials will be used to manufacture the magnet depending on the purpose and design. Before the wide spread use of superconducting magnets and in particularly high field magnets, electromagnetic stress were not an area of concern in magnet design. In most cases, the thick wires used to carry the current were enough to contain the Lorentz forces in the magnet. As high magnetic field research started taking more importance, pulsed magnets were used. These magnets didn't have the problem with thermal strains, but the effect of Lorentz forces began emerging. However, the mechanical failure due to large EM forces started becoming a problem as high-field solenoids started becoming an area of interest.

Some of the first literature regarding the calculation of forces in a solenoid was by Cockroft [68]. They calculated the EM forces from the magnetic field components by solving the Maxwell equations. Superconducting magnets started

coming into the picture much later after the discovery of superconductivity. Yntema (1955) proposed an electromagnet using a superconductor wire and a Niobium Wire operating at 4.2K [69]. Later, a Niobium Tin (Nb_3Sn) based wire was proposed, where the brittle powdery Nb_3Sn was filled in a Niobium tube, creating a composite structure. Based on the theories of London, multi- filamentary wires were proposed, which can help in enhancing current carrying capacity and lower AC losses.

Typically, a force generated in a 1.5T MRI scanner is equated to hundreds of psi pressure in a pipe. The strongest MRI magnet to date, the INUMAC MRI at 11.7T, is expected to have an operational stress of ~400 MPa [42], [70].

Some of the critical components of the magnet in this design are the Helium vessel bore and cryostat made of SS304L and the bobbin that is made up of AA5083.

The conductor used for the coils has a copper to superconductor (Cu: SC) ratio of 9:1 and 11:1 and is in the form of a wire-in-channel (WIC) conductor. This conductor has a sheath of PET insulation and is impregnated using a cryogenic grade epoxy such as MY750. In order to accurately calculate the stress state, it is important to have the material properties of each material.

3.2 Modelling of Wire Material Properties

Superconductor wires commonly utilized are constructed as multi-filamentary structures, incorporating Nb-Ti superconductor within a copper matrix. These wires present with varying SC: Cu ratios, typically ranging from 1:1 to 1:5. The presence of the copper matrix serves to support the wire against forces generated during its operation and also safeguarding the delicate superconducting filaments from potential damage. Additionally, during quench events, the copper matrix assists in carrying a significant portion of the current and facilitates the dissipation of heat produced within the quenched zone. In applications like self-contained magnets, such as those found in MRI systems, a higher Cu:SC ratio is preferred, leading to the use of conductors like Wire in Channel (WIC) configurations. These alternative conductors can achieve substantially higher SC:Cu ratios, typically ranging from 8:1 to 15:1. To ensure electrical insulation, the superconducting wires are either coated with enamel or enclosed in a PET sleeve. The mechanical and thermal properties of these composite

coils can be orthotropic and notably distinct from those of their constituent materials, owing to various winding techniques such as wet winding, Vacuum Pressure impregnation (VPI), wax impregnation, and dry winding. Given the complex composite nature of these wires, traditional methods for estimating material properties, including elastic properties, thermal expansion coefficients, and thermal conductivities, prove challenging due to the absence of a statistically distributed component structure typical in most composite models. Consequently, numerical homogenization emerges as a viable approach for determining the overall material properties of the wire, albeit with an acceptable margin of error in estimation.

It is difficult to estimate the composite material properties, such as elastic properties, thermal expansion coefficients, thermal conductivities, using simple techniques. This may be due to a lack of statistical distribution of components that most composite models or their composite structure of high-volume fractions. Thus, a reasonable means to obtain material properties of the wire as a whole is numerical homogenization of composite wire with the only downside being an acceptable error in estimation.

3.2.1 Modelling of Elastic Properties

The use of composite superconductors in MRI magnets involves a complex interplay of repetitive microstructures, which play a crucial role in determining the material's overall performance. Numerical homogenization of this repetitive microstructure may provide effective elastic properties. By treating them as unit cells with appropriate boundary conditions for magnet modelling, valuable understanding of the material behaviour at different scales can be obtained.

One such method, asymptotic homogenization, relies on the superposition of global and periodic local perturbations to model the elastic properties of superconducting wire accurately. While this approach proves effective for microstructures exhibiting repetition, challenges arise when dealing with non-repetitive microstructures. In such cases, the elasticity bounds may vary depending on specific microstructural parameters, introducing complexities in the analysis.

The Voigt and Reuss models, originating from the pivotal works of Voigt and Reuss respectively, offer approximate solutions for estimating the elastic properties of composite materials. The difference between these two methods varies

under the assumption that either the strain or stress tensor remains constant throughout the scale of the microstructural constituent component of the composite, respectively. Voigt's method [71], often referred to as the "rule of mixture" provides an upper bound, while Reuss's method [72], known as the "inverse rule of mixture," offers a lower bound. The Voigt method to approximate the elastic properties is written as

$$\boldsymbol{C(v)} = \sum_{\boldsymbol{C=1}}^{\boldsymbol{N}} \boldsymbol{V(c)\, C} \tag{3.1}$$

Similarly, the Reuss method to estimate the elastic properties is written as

$$S(v) = \sum_{C=1}^{N} V(c)\, S(c) \tag{3.2}$$

In the equation, $V(c)$, $C(v)$ and $S(v)$ denotes volume fraction, elastic stiffness and elastic compliance tensors of the constituents respectively. However, it was Hill who proposed an improvement by suggesting that the composite's stiffness lies somewhere between these bounds, known as the Voigt-Reuss-Hill approximation [73]. This advancement paved the way for more refined approaches, incorporating factors such as polycrystal orientation distribution functions to enhance accuracy further [74]. In simple terms, Hill proposed the stiffness of a composite is the average of the Voigt and Reuss bounds.

$$S^{VRH} = \frac{1}{2}\,(S^{V} + S^{R}) \tag{3.3}$$

In the equation S^{VRH}, S^{V}, S^{R} are the elastic stiffness values of Voigt, Reuss and Voigt-Reuss-Hill approximation, respectively.

Subsequent refinements by researchers like Hashin and Shtrikman have led to improved models for property estimation, contributing to the ongoing development of composite material characterization[75]–[77]. Furthermore, modelling the nonlinear constitutive behaviour of these composites requires the identification of representative volume elements (RVEs) or representative unit cells (RUCs) with appropriate boundary conditions. Various methodologies, including Bishop and Hill's [78], [79] extension of Taylor's work and self-consistent methods

[80], have been proposed to address these complexities, providing valuable insights into the nonlinear behaviour of composite materials.

For estimating the linear elastic response of composite structures containing fibres and matrices, a systematic approach involving the application of unit strain in six directions simplifies the process. These techniques form the foundation for understanding the mechanical behaviour of composite materials. Additionally, the calculation of components of the stiffness tensor can be achieved using finite element analysis (FEA) techniques and Gauss-Legendre quadrature, or through commercially available FEA software like ANSYS, which streamlines the computational process.

3.2.2 Modelling of Thermal Expansion Coefficient

The modelling of thermal expansion coefficients in composites evolved quite later to the development of methodologies for assessing effective mechanical properties. Hashin's review on fundamental composite mechanical property estimation, while comprehensive, did not encompass the approximation of thermal expansion coefficients [81]. This gap persisted until Schapery introduced the energy principle method for approximating thermal expansion coefficients, thereby initiating more focused investigations in this domain [82]. Prior to Schapery's contribution, there was limited literature available on the estimation of thermal expansion coefficients for isotropic, particulate-filled composites.

Some of the earlier work on thermal expansion coefficients was conducted by Levin [83]. This approach represented an extension of Hill's method [84] and laid the groundwork for subsequent developments in this field. Central to Levin's formulation is the calculation of the overall thermal strain vector using the principle of virtual work, expressed as

$$\overline{\alpha_{ij}} = \frac{1}{V} \int B_{ijkl}^{T} \, \alpha_{ij} dV \tag{3.4}$$

where $\overline{\alpha_{ij}}$ and α_{ij} represent the average thermal expansion coefficient tensors at meso-scale and micro-scale, respectively, and B_{ijkl} is the stress influence function tensor. This tensor relates the uniform overall stress field σ_{kl}^{0} to local stress σ_{ij}^{r} [85]

$$\sigma_{ij}^{r} = B_{ijkl}\sigma_{kl}^{0} \quad (3.5)$$

As methodologies for estimating thermal expansion coefficients matured, they paved the way for the modelling of heterogeneous multiphase composites in various applications. Noteworthy advancements include Takao's formulation [86]of an effective thermal expansion coefficient for anisotropic short fibre-reinforced composites based on Eshelby's equivalent inclusion method [87], and Adams' introduction [88] of the first finite element analysis (FEA) approach to estimate effective thermal expansion coefficients for unidirectional composites. Subsequent efforts have saw the use of FEA-based methods, which have been applied to model a range of materials, including metal matrix composites and superconductors [89], [90].

In the context of this study, FEA methods are particularly advantageous, with ANSYS being the chosen approach for analysing the magnet and wires. When considering the stresses in coils, while a preliminary estimation can be made by assuming coil properties to be identical to copper, achieving a comprehensive understanding necessitates the determination of the coil's orthotropic properties. This entails accounting for the presence of copper, Nb-Ti, epoxy, and insulation materials. Notably, the coil exhibits greater strength in the azimuthal and winding directions, while its strength is comparatively weaker in the radial and axial directions. Thus, a thorough understanding of the orthotropic properties of the coil is essential for accurate stress analysis and design optimization.

3.3 Properties of Individual Materials

The properties of individual components were initially required to study their isolated properties. These properties are necessary for the whole temperature range of operation, i.e. 300-4.2 K. The properties are referred from literature and were referred from the NIST database whenever possible[26], [91]. The NIST material database is compiled based on experimental data and established interpolation techniques.

3.3.1 Stainless Steel SS304L

The most common steel grade used for cryogenic applications is SS304L. In this application, the helium vessel, outer vacuum vessel and the fasteners used will be made of SS304L. The Young’s modulus, Poisson’s ratio and the instantaneous

thermal expansion coefficient for SS304L is shown in Figure 3.1 [26], [51], [92]. It can be seen that stainless steel grade like most materials has a higher Young's modulus at low temperatures, however it attains a peak at around 50-60K.

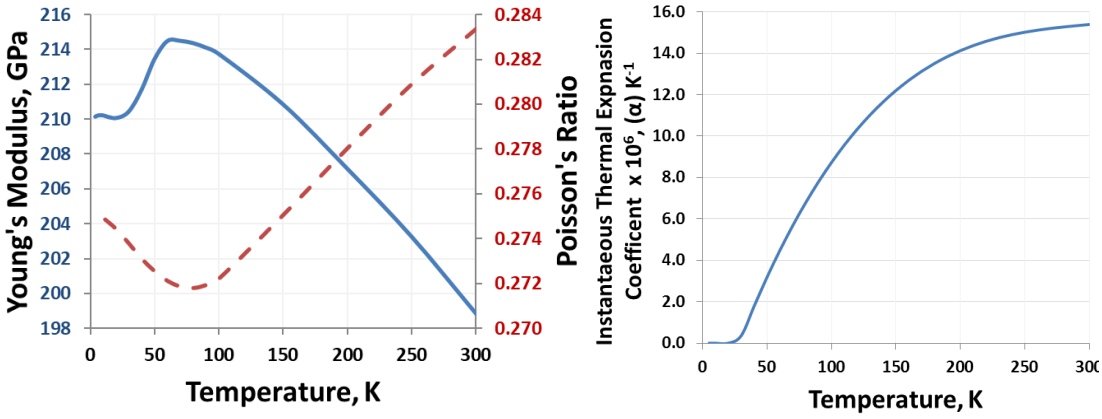

(a) (b)

Figure 3.1 (a) Young's modulus, Poisson's ratio and (b) instantaneous thermal expansion coefficient of SS 304L

3.3.2 Aluminium Alloys

While various alloys of aluminium are available, the AA 50xx series provides a good balance between strength, availability machinability and weldability. AA 50xx series provides good strength in the whole cryogenic range, similar to the 60xx series and 20xx series. It is also widely available in various forms, such as sheets, plates, rods, etc. The 50xx series has better weldability and machinability compared to the 20xx series. Out of the options, AA 5083 H32 aluminium alloy is selected for use in the bobbin., AA 5083 is as aluminium magnesium alloy traces of manganese and chromium. It is extremely resistant to industrial chemicals and saltwater damage. AA 5083 is incredibly strong even after welding. Among the non-heat treatable alloys, it possesses the highest strength. Moreover, AA 5083 is frequently employed in cryogenic applications due to its 77K (-196°C) cooling capability. The alloy shows outstanding fracture toughness at this temperature, with a 40% increase in ultimate tensile strength and a 10% yield strength increase. The alloy that has been stabilized by low-temperature heating and subsequently tempered by the H32 Strain (1/4 hardness) is chosen. The alloy with a further tempering H32 Strain hardened (1/4 hard) and stabilized by low-temperature heating alloy is selected. The Young's modulus, Poisson's ratio and the instantaneous thermal expansion coefficient for AA5083 is shown in Figure 3.2 [26], [51], [92].

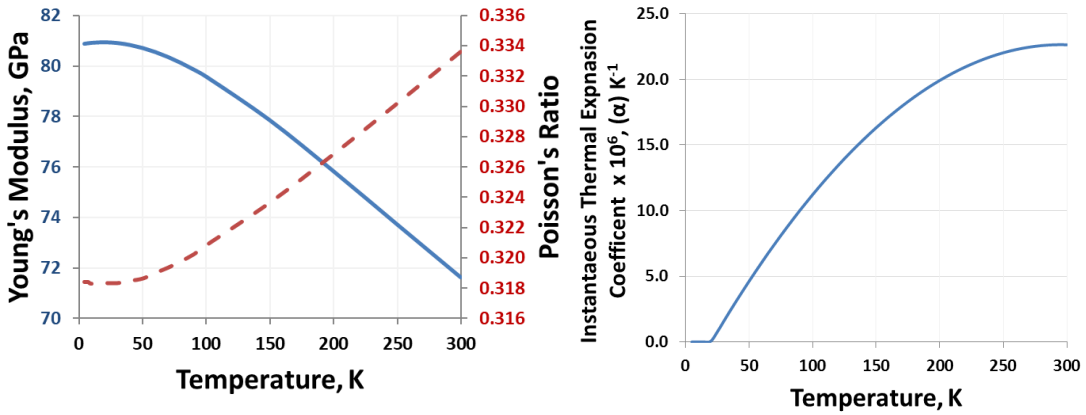

(a) (b)

Figure 3.2 (a) Young's modulus, Poisson's ratio and (b) instantaneous thermal expansion coefficient of AA 5083 H32

3.3.3 OFHC Copper

Oxygen free, high conductivity copper (OHFC) is used as a matrix of the superconducting wires of the magnet. The Young's modulus, Poisson's ratio and the instantaneous thermal expansion coefficient for AA5083 is shown in Figure 3.3 [26], [93]–[95]. These mechanical properties are crucial for ensuring the structural integrity and performance of the superconducting wires under varying thermal and mechanical stresses. The the copper matrix provides strength to the wire and is particularly important to minimize stress and avoid potential damage during operation.

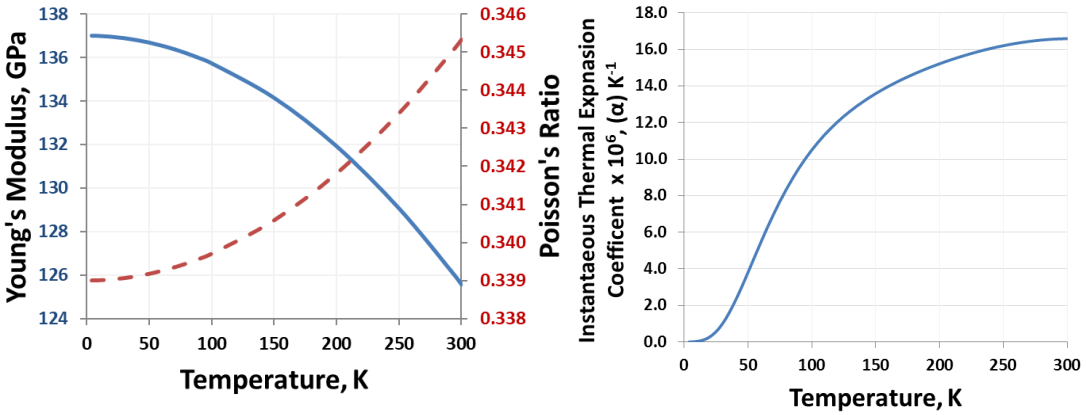

(a) (b)

Figure 3.3 (a) Young's modulus, Poisson's ratio and (b) instantaneous thermal expansion coefficient of OFHC Copper

3.3.4 Niobium Titanium (Nb-Ti)

Niobium Titanium is the superconductor most widely used in MRI magnets. The Young's modulus, Poisson's ratio and the instantaneous thermal expansion coefficient of Nb-Ti is shown in Figure 3.4 [92], [95].

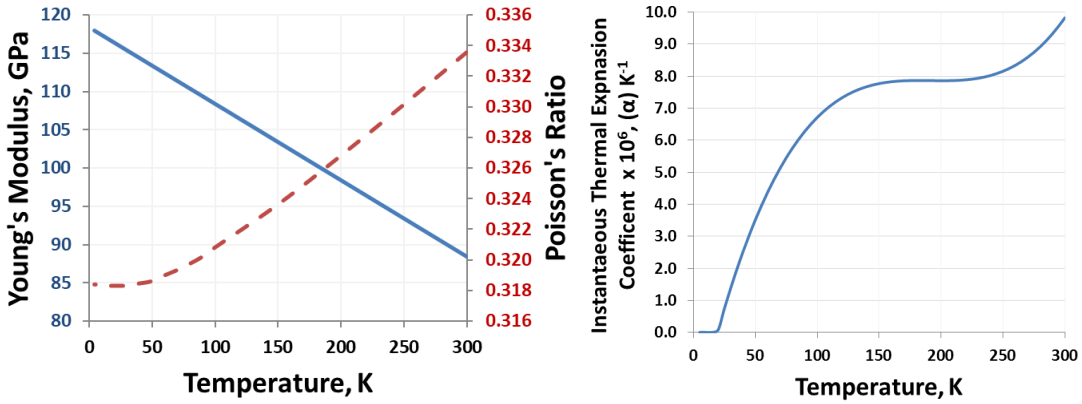

(a) (b)

Figure 3.4 Young's modulus, Poisson's ratio and (b) instantaneous thermal expansion coefficient of Nb-Ti

3.3.5 Epoxy

Different epoxies are under consideration for MRI magnets. MY750/HY5922 by Huntsman/Vantico Ltd and CTD 101K by Composite Technology Development, Inc. were the most widely used ones. Out of these, MY750/HY5922 was chosen as the epoxy system to use. The mechanical properties of these materials are not widely available, and properties at cryogenic temperatures are even scarcer.

Bagrets N et al. measured Young's modulus and other properties of MY750/HY5922 for three temperatures: 300 K, 77 K and 4.2 K [96]–[98]. The MY750/HY5922 data sheet quotes Young's modulus in the 2.8-3.0 GPa range at room temperature, which agrees with the experimental data. The thermal expansion coefficient is also calculated from the linear expansion data obtained from the same literature. Young's modulus and average thermal expansion coefficient of MY750/HY5922 epoxy is shown in Figure 3.5 [99].

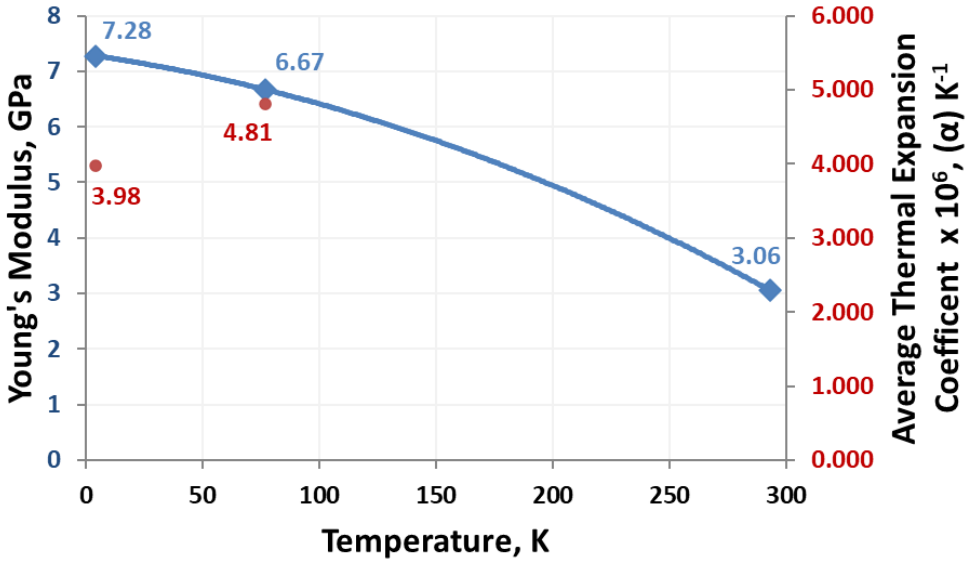

Figure 3.5 Young's modulus and average thermal expansion coefficient of MY750/HY5922 epoxy

3.4 Composite Property Calculation - Structure Estimation

In order to find the dimensions and, thus, the volume fraction of different components, the winding of the coils is inspected under a microscope and the dimensions are measured.

In order to make a prototype coil, a single bobbin was manufactured using aluminium 6061 such that the dimensions are similar to the smallest primary coil pair. The coil is wound on the bobbin using a piece of sample wire, at the facility in VECC, Kolkata. The photographs of the bobbin and the winding process are shown in Figure 3.6 (a) and (b).

The coil was wound using a similar sized wire to the magnet and impregnated using a room temperature cure resin. This ensured the coil will have similar dimensional characteristics although it might not have a similar strength or the same process. The coil was then cut and a sample was taken to inspect under microscope.

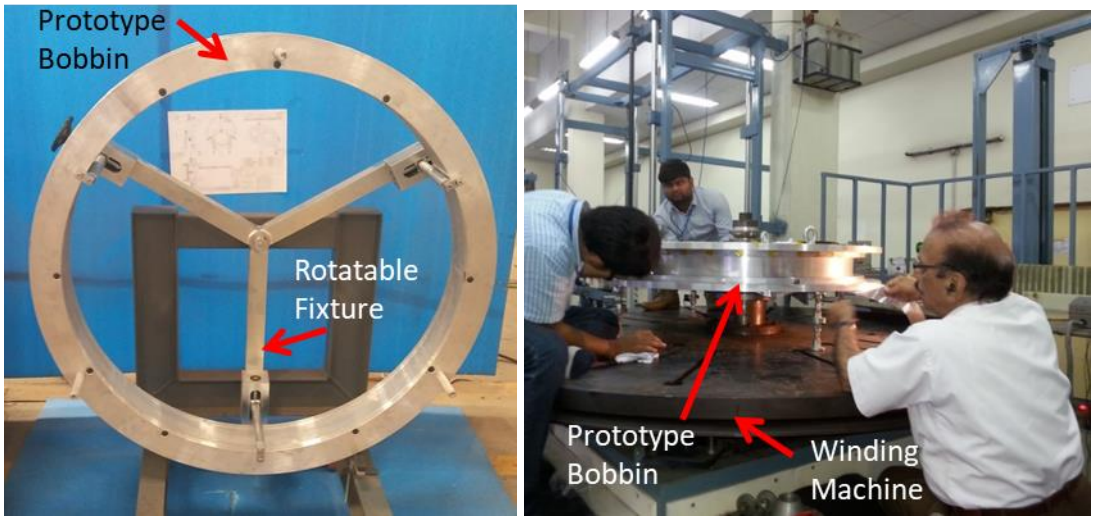

(a) (b)

Figure 3.6 The prototype bobbin made using aluminium (a) and the winding process of the coil in VECC, Kolkata (b)

After winding, and resin cure, the coil was then cut and a sample was taken to inspect under microscope. The grid structure (a) and the dimensions (b) are shown in Figure 3.7.

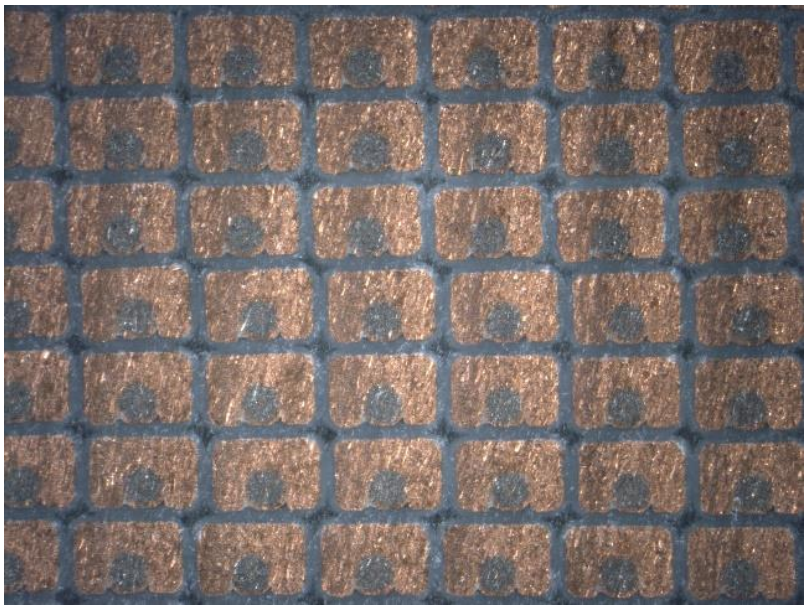

(a)

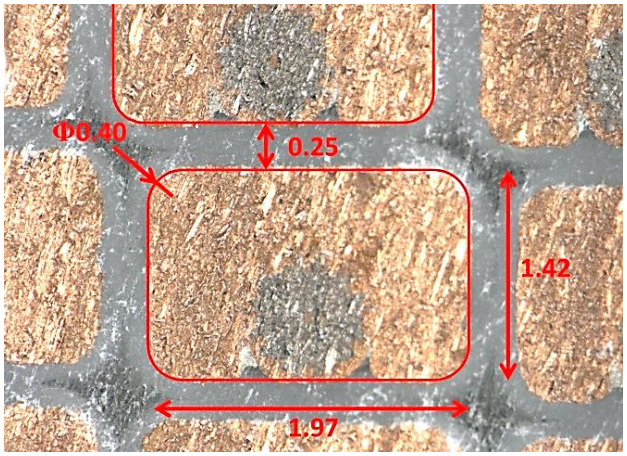

(b)

Figure 3.7 Microscopic view of a coil cross-section showing (a) the wire packing and grid and (b) showing the dimension (mm) of a single wire.

Based on the measurements, a Representative Volume Element (RVE) is created for both the main coil and the shield coil. The bare dimensions of the wire are measured, while the Cu:SC ratio is provided by the wire manufacturer. The PET insulation thickness was taken to be 0.125 mm. The porosity of the PET insulation was taken to be 50%, and the rest of the volume is assumed to be filled with epoxy. Based on this configuration, the RVE was made for both the coils. The RVE model was used to calculate the composite, and the volume fraction for each component was also calculated (Table 3.1). Figure 3.8 shows the RVE and the various components that make up the RVE.

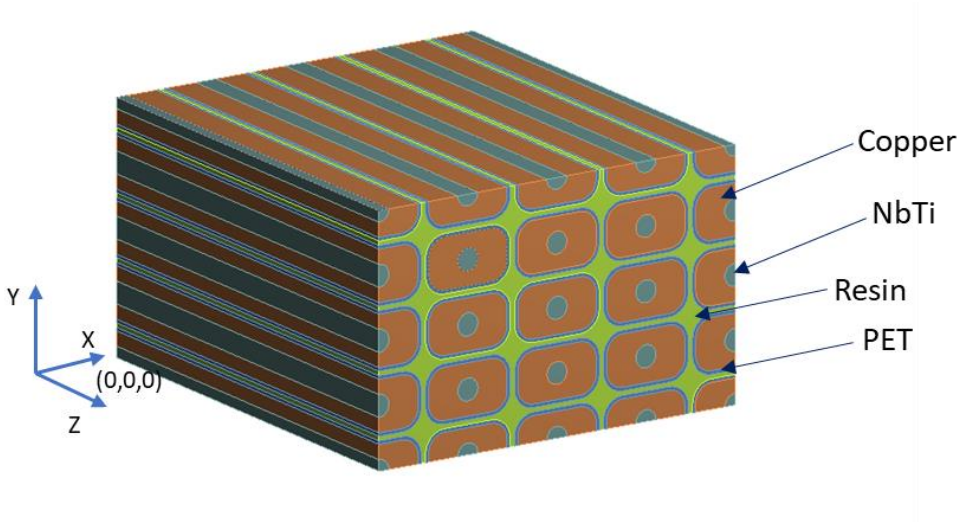

Figure 3.8 Composition of the Representative Volume Element (RVE) showing various components present in an MRI coil

Table 3.1 Volume fraction of various components present in the MRI main coils and shield coils.

	Copper	**Nb-Ti**	**Epoxy**	**Polyester**
Main coil	0.64	0.07	0.14	0.14
Shield Coil	0.70	0.06	0.12	0.12

3.5 Composite Properties for Coils

Computational modelling of a composite structure such as a superconducting coil is computationally intensive, and a very fine level of detail is required during modelling. In order to reduce the complexity of the problem, homogenization is considered to be a viable approach. This aids in connecting the individual micro components in the structure to a single homogenised structure on a larger macro scale. In general, the most common models used for homogenisation are the Reuss model (rule of mixtures) and the Voigt model (inverse rule of mixtures)

The Reuss model, also known as the rule of mixtures, is a theoretical framework used to estimate the overall properties of composite materials based on the properties of their individual components. Formulated in the early 20th century by Gustav Reuss, this model assumes that when two or more materials are combined to form a composite, the stress or strain experienced by each component is the same. This simplistic approach treats the composite material as a homogenized entity, disregarding any interactions or variations between its constituents. The Reuss model serves as a valuable tool in predicting the mechanical behaviour of composites, offering a straightforward calculation method for properties such as elastic modulus and strength. However, its simplicity can lead to inaccuracies, particularly when applied to heterogeneous materials or those with complex microstructures.

In contrast, the Voigt model, often referred to as the inverse rule of mixtures, presents a complementary perspective on composite material behaviour. Proposed independently by Woldemar Voigt, this model assumes that the strains experienced by each constituent of a composite material are identical when subjected to external loads. Unlike the Reuss model, the Voigt model considers the interactions

between individual components within the composite, acknowledging their influence on the overall mechanical response. By accounting for these interactions, the Voigt model provides a more refined estimation of composite properties, particularly in cases where the constituents exhibit significant disparities in stiffness or other mechanical characteristics. Despite its enhanced accuracy, the Voigt model can still oversimplify certain aspects of composite behaviour, necessitating careful consideration of material-specific factors and microstructural complexities.

The Reuss model and the Voigt model represent the lower and upper bounds of composite properties, respectively, through their assumptions and approaches to calculating the overall behaviour of composite materials. The Reuss model represents the lower bound of composite properties because it assumes minimal interaction or reinforcement between the individual components. Consequently, it predicts conservative estimates for properties such as elastic modulus and strength, neglecting any synergistic effects that may enhance the material's performance. Conversely, the Voigt model assumes that the strains experienced by each constituent are identical under external loads. By incorporating these interactions, the Voigt model provides a more refined estimation of composite properties compared to the Reuss model. However, it still represents an upper bound because it assumes perfect bonding and alignment between the components, which may not always be achievable in practice. Thus, the Voigt model tends to predict more optimistic values for composite properties. Considering the coil is the strongest in the azimuthal direction and weakest in the radial or axial direction, the Reuss & Voigt models can roughly predict the radial and azimuthal (circumferential) properties, respectively.

$$E_{circum} = \sum E_i \, V_i \tag{3.6}$$

$$E_{radial}/E_{axial} = \sum \frac{E_i}{V_i} \tag{3.7}$$

3.5.1 Poisson's Ratio

$$\nu_{circum-radial,}\nu_{circum-axial,} = \sum \nu_i \, V_i \tag{3.8}$$

$$\nu_{Radial-Axial} = \quad E_{circum} \sum \frac{\nu_i \, V_i}{E_i} \tag{3.9}$$

3.5.2 Shear modulus

$$G_{circum} = \frac{E_{circum}}{2\,(1 + \nu_{radial-axial})} \tag{3.10}$$

$$G_{radial}/G_{axial} = \frac{E_{radial}}{2\,(1 + \nu_{circum-radial})} \tag{3.11}$$

Here *E* is the Young's modulus, *V* is the Volume fraction, *v* is the Poisson's ratio and *G* is the shear modulus. The subscripts are circumferential (circum), radial, and axial and the subscript '*i*' denotes each component.

Figure 3.9 shows Young's modulus estimates from the Reuss model (radial) and Voigt model (circumferential). They represent the upper and lower limits of the mechanical properties of a composite.

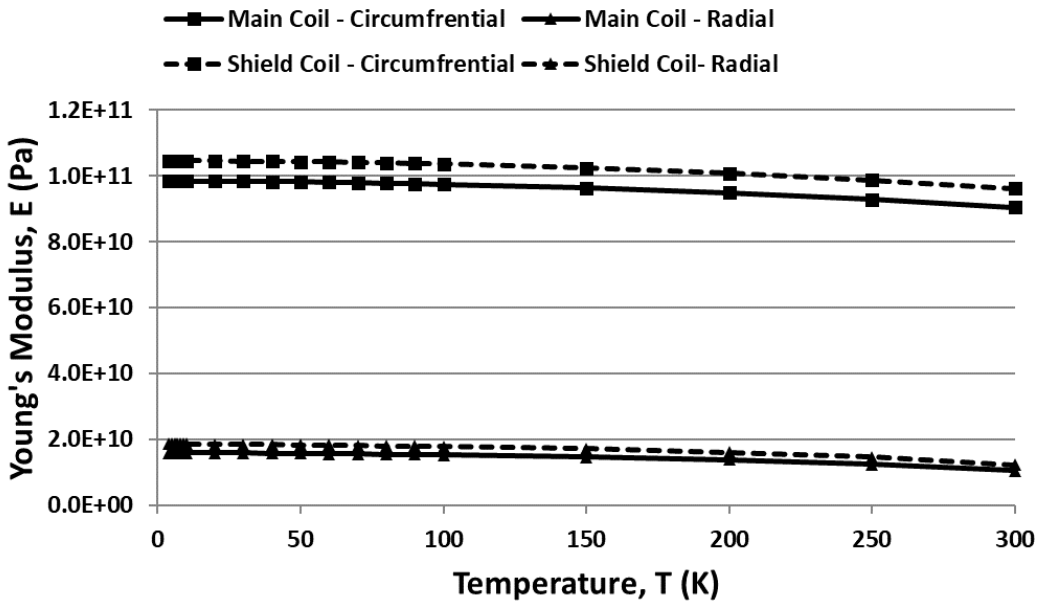

Figure 3.9 Young's Modulus estimates of the main coil and shield coil from the Reuss Model and Voigt Model. They represent the upper and lower limits of the mechanical properties of a composite.

A more accurate prediction of the composite properties of the coil can be made using the Representative Volume Element (RVE) method. In this method, a small volume of the composite material is chosen such that it represents the microstructure of the entire material. This volume should be large enough to contain a representative sample of all the phases and their interactions within the composite. The properties of this volume are then analysed using techniques like finite element analysis (FEA) or analytical methods to predict the overall mechanical behaviour of the material. [29], [100]–[102].

By accurately capturing the microstructural features and interactions within the material, the RVE method can provide more precise predictions of mechanical properties compared to the simplified Reuss and Voigt models. This makes it a valuable tool for designing and optimizing composite materials for various applications. From Hook's law, the stress compliance matrix for a RVE can be written as

$$\begin{Bmatrix} \varepsilon_1 \\ \varepsilon_2 \\ \varepsilon_3 \\ \gamma_4 \\ \gamma_4 \\ \gamma_6 \end{Bmatrix} = \begin{bmatrix} S_{11} & S_{12} & S_{13} & . & . & S_{19} \\ S_{21} & . & . & . & . & . \\ S_{31} & . & . & . & . & . \\ . & . & . & . & . & . \\ . & . & . & . & . & . \\ S_{91} & . & . & . & . & S_{99} \end{bmatrix} \begin{Bmatrix} \sigma_1 \\ \sigma_2 \\ \sigma_3 \\ \sigma_4 \\ \sigma_5 \\ \sigma_6 \end{Bmatrix} \tag{3.12}$$

Considering symmetry across the three orthogonal planes, and assuming $\varepsilon_{12} = \varepsilon_{21}$ etc, the compliance matrix can be reduced as

$$\begin{Bmatrix} \varepsilon_1 \\ \varepsilon_2 \\ \varepsilon_3 \\ \gamma_4 \\ \gamma_4 \\ \gamma_6 \end{Bmatrix} = \begin{bmatrix} S_{11} & S_{12} & S_{13} & 0 & 0 & 0 \\ S_{21} & S_{22} & S_{23} & 0 & 0 & 0 \\ S_{31} & S_{32} & S_{33} & 0 & 0 & 0 \\ 0 & 0 & 0 & S_{44} & 0 & 0 \\ 0 & 0 & 0 & 0 & S_{55} & 0 \\ 0 & 0 & 0 & 0 & 0 & S_{66} \end{bmatrix} \begin{Bmatrix} \sigma_1 \\ \sigma_2 \\ \sigma_3 \\ \sigma_4 \\ \sigma_5 \\ \sigma_6 \end{Bmatrix} \tag{3.13}$$

Replacing the compliance elements with elastic constants, equation (3.13) can be rewritten as

$$\begin{Bmatrix} \varepsilon_1 \\ \varepsilon_2 \\ \varepsilon_3 \\ \gamma_4 \\ \gamma_4 \\ \gamma_6 \end{Bmatrix} = \begin{bmatrix} \frac{1}{E_1} & -\frac{\nu_{21}}{E_2} & -\frac{\nu_{31}}{E_3} & 0 & 0 & 0 \\ -\frac{\nu_{12}}{E_1} & \frac{1}{E_2} & -\frac{\nu_{32}}{E_3} & 0 & 0 & 0 \\ -\frac{\nu_{13}}{E_1} & -\frac{\nu_{23}}{E_2} & \frac{1}{E_3} & 0 & 0 & 0 \\ 0 & 0 & 0 & \frac{1}{G_{23}} & 0 & 0 \\ 0 & 0 & 0 & 0 & \frac{1}{G_{13}} & 0 \\ 0 & 0 & 0 & 0 & 0 & \frac{1}{G_{12}} \end{bmatrix} \begin{Bmatrix} \sigma_1 \\ \sigma_2 \\ \sigma_3 \\ \sigma_4 \\ \sigma_5 \\ \sigma_6 \end{Bmatrix} \tag{3.14}$$

Considering the symmetry of the compliance matrix and expanding the matrix, each engineering constant can be solved by varying the boundary conditions. For example, considering the first line,

$$\varepsilon_1 = \frac{\sigma_1}{E_1} - \frac{\sigma_2\,\nu_{21}}{E_2} - \frac{\sigma_3\,\nu_{31}}{E_3} \tag{3.15}$$

This can be further expanded in a RVE as

$$\frac{\Delta L_1}{L_1} = \frac{F_1}{A_1.E_1} - \frac{F_2 \Delta L_2}{A_2.\Delta L_1.E_2} - \frac{F_3.\Delta L_3}{A_3.\Delta L_1 E_3} \tag{3.16}$$

By solving the compliance matrix, six equations can be derived. The compliance matrix can be solved by applying various boundary conditions and measuring the reaction.

Table 3.2 Critical dimensions of the Representative Volume Element (RVE) for the Main coil and the shield coil

Property	Main Coil (mm)	Shield Coil (mm)
Wire Size	2.23x1.42	2.55x1.77
ΔX	8.92	10.20
ΔY	5.68	7.08
ΔZ	10.00	10.00
Displacement (U)	1.00	1.00

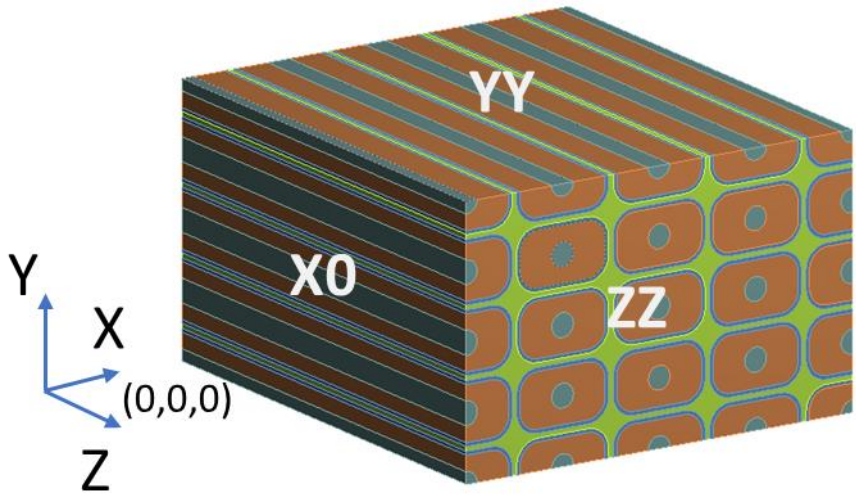

Figure 3.10 Composition of the RVE showing various components and definition of various faces on the RVE

The RVE is taken to have six perpendicular faces with one corner taken as (0,0,0). The faces connected to this point are named X0, Y0, and Z0. Figure 3.10 shows the composition of the RVE showing various components. Table 3.2 lists the critical dimensions of the RVE for the main coil and the shield coil. The faces parallel to these are XX, YY, and ZZ. The distance between the faces is then denoted by ΔX, ΔY, and ΔZ. The following cases, as shown in Table 3.3, based on unit displacement (U) of various faces, can be considered for the RVE.

Table 3.3 Different cases with different boundary conditions applied on the RVE

Case	X0	Y0	Z0	XX	YY	ZZ
1	Ux=0	Uy=0	Uz=0	Ux=1	Uy=cp	Uz=cp
2	Ux=0	Uy=0	Uz=0	Ux=cp	Uy=1	Uz=0
3	Ux=0	Uy=0	Uz=0	Ux=cp	Uy=cp	Uz=1
4	Uy=Uz=0	Ux=Uy=Uz=0	Uy=Uz=0	Uy=Uz=0	Ux=1	Uy=Uz=0
5	Uy=Uz=0	Uy=Uz=0	Ux=Uy=Uz=0	Uy=Uz=0	Uy=Uz=0	Uy=1
6	Ux=Uz=0	Ux=Uz=0	Ux=Uy=Uz=0	Ux=Uz=0	Ux=Uz=0	Uy=1

Here, ‘cp’ denotes a coupled condition where all the nodes on that face have the same displacement.

Using the results from these boundary conditions and solving the compliance matrix (eqn 3.9), the engineering constants can be calculated as shown in Table 3.4.

Table 3.4 Engineering constants based on various boundary conditions

Case	Engineering constant
1	$E_{xx} = \frac{\Delta X \,.\, F_{x\,(X0)}}{U_{x\,(XX)}}$
2	$E_{yy} = \frac{\Delta Y \,.\, F_{y\,(Y0)}}{U_{y\,(YY)}}$
3	$E_{zz} = \frac{\Delta Z \,.\, F_{z\,(Z0)}}{U_{z\,(ZZ)}}$
4	$G_{xy} = \frac{\Delta Y \,.\, F_{x\,(Y0)}}{\Delta X \,.\, \Delta Z \,.\, U_{x\,(ZZ)}}$
5	$G_{xz} = \frac{\Delta Z \,.\, F_{x\,(Z0)}}{\Delta X \,.\, \Delta Y \,.\, U_{x\,(ZZ)}}$

6	$G_{yz} = \frac{\Delta Z \,.\, F_{y\,(Z0)}}{\Delta X \,.\, \Delta Y \,.\, U_{y\,(ZZ)}}$
1	$\nu_{xy} = \frac{\Delta Y \,.\, U_{y\,(YY)}}{\Delta X \,.\, U_{x\,(XX)}}$
1	$\nu_{xz} = \frac{\Delta Z \,.\, U_{z\,(ZZ)}}{\Delta X \,.\, U_{x\,(XX)}}$
3	$\nu_{yz} = \frac{\Delta Z \,.\, U_{z\,(ZZ)}}{\Delta Y \,.\, U_{y\,(YY)}}$

The engineering constants across the whole temperature range for the coil structure is calculated based on the methodology above. The Young's modulus (*E*) and the shear modulus (*G*) in the three orthogonal directions for the main coil are calculated and are shown in Figure 3.11. Figure 3.12 shows the Poisson's ratio for the main coil in the three directions. Young's modulus (*E*) and shear modulus (*G*) for the shield coil RVE in three orthogonal directions is shown in Figure 3.13. Figure 3.14 shows Poisson's ratio for the shield coil RVE in three orthogonal directions.

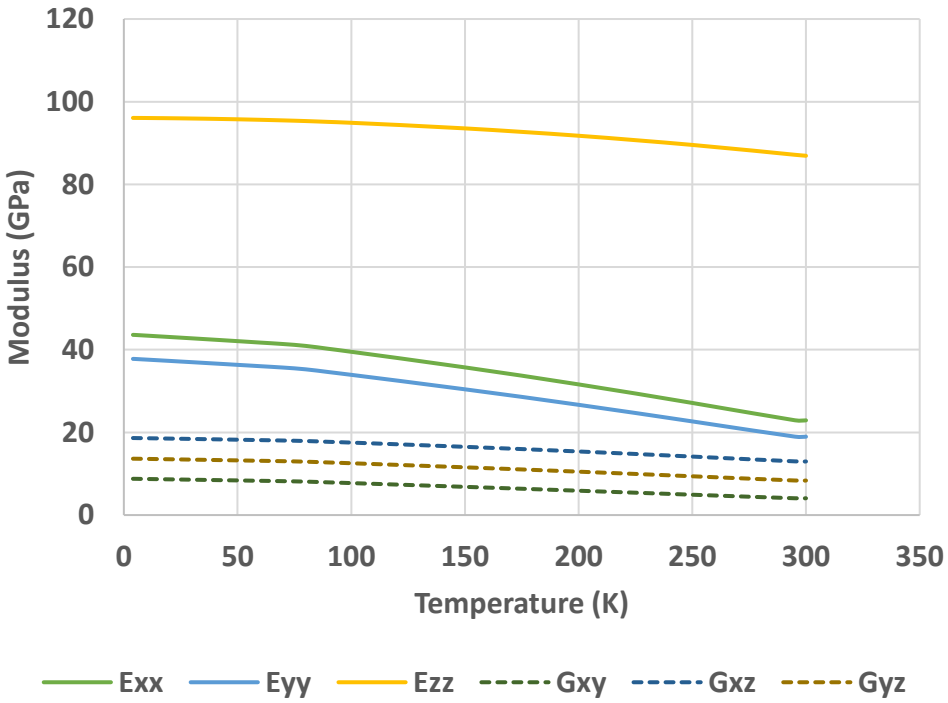

Figure 3.11 Young's Modulus (*E*) and Shear modulus (*G*) for the main coil RVE in three orthogonal directions

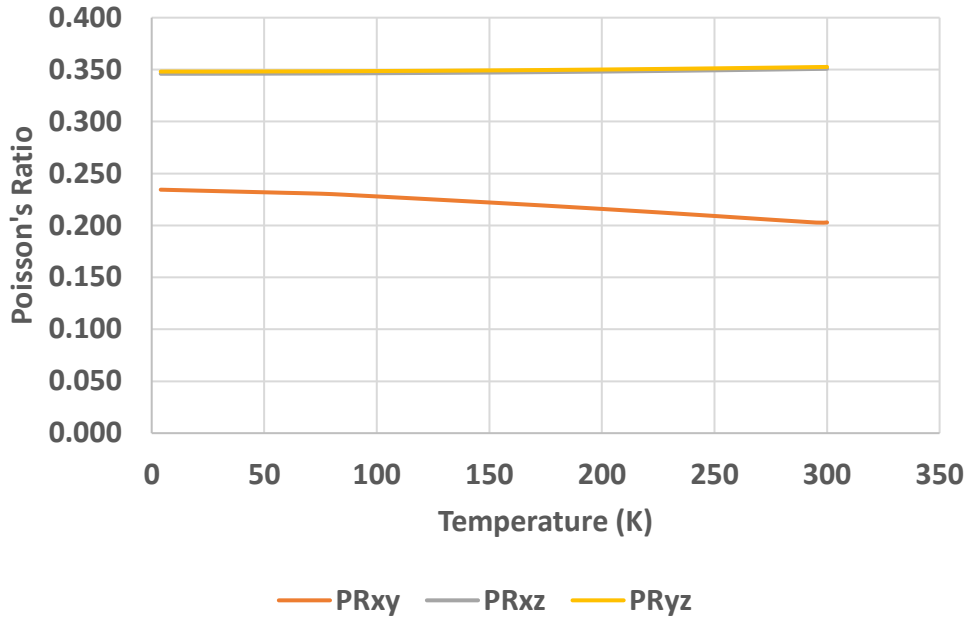

Figure 3.12 Poisson's ratio for the main coil RVE in three orthogonal directions. The values for *PRxz* and *PRyz* are very similar and the respective curves overlap in the graph.

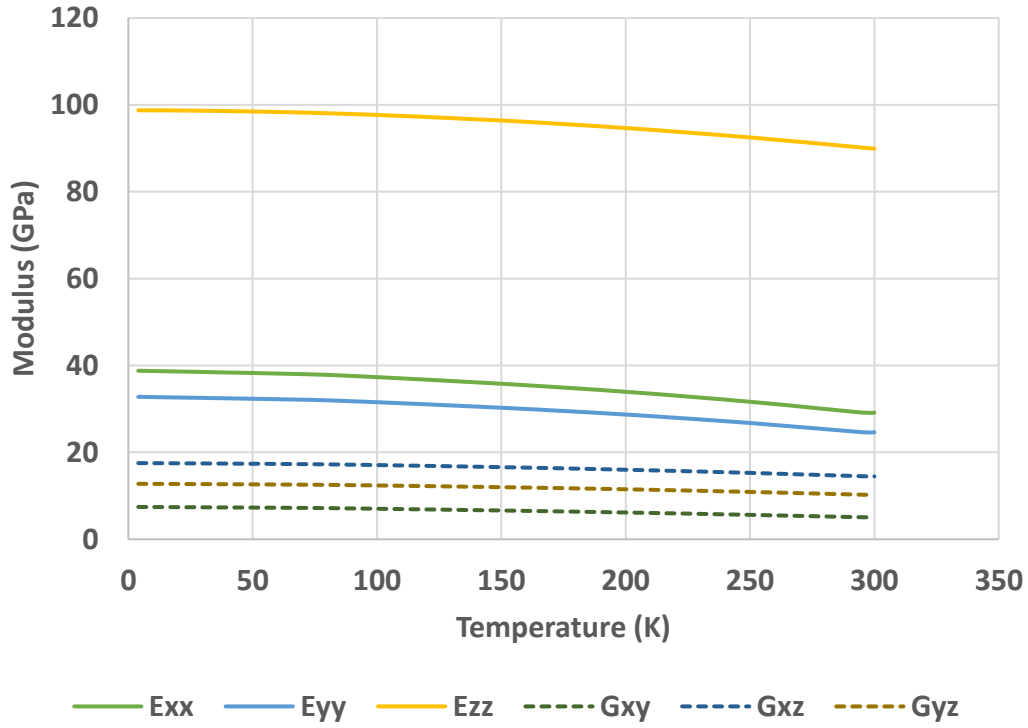

Figure 3.13 Young's modulus (*E*) and Shear modulus (*G*) for the shield coil RVE in three orthogonal directions

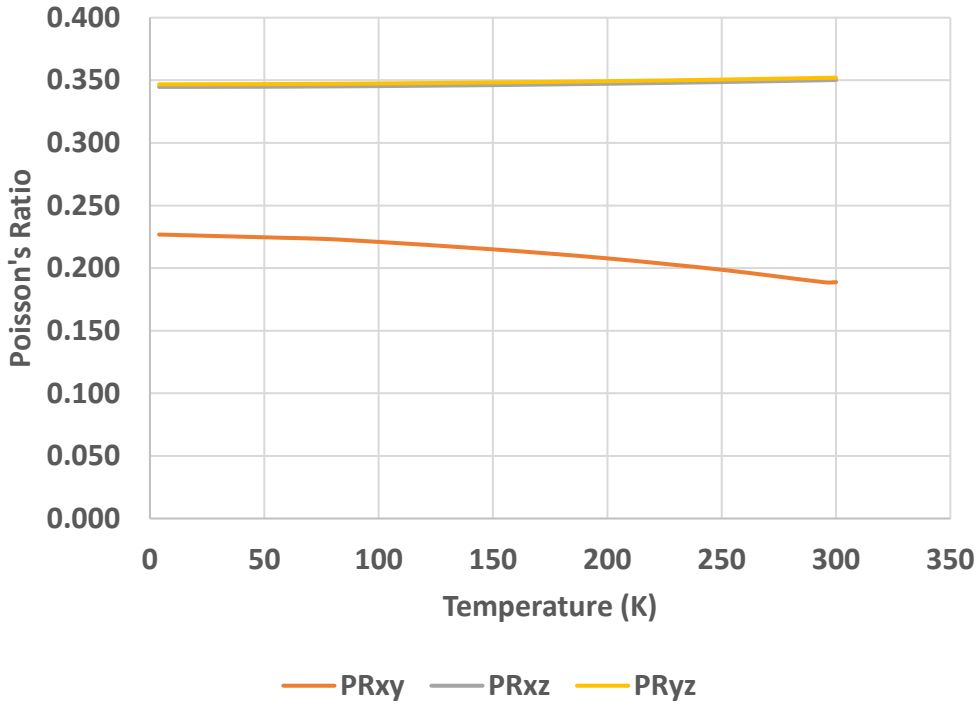

Figure 3.14 Poisson's ratio for the shield coil RVE in three orthogonal directions. The values for PRxz and *PRyz* are very similar and the respective curves overlap in the graph

3.5.3 Thermal Expansion Coefficient

To find the average/secant thermal expansion, the RVE was cooled down to the desired temperature (4.2K) and the deformation was recorded for each face. The X0, Y0, Z0 faces, as explained before were held fixed while the faces XX, YY, ZZ were left free. The directional deformation in each direction is simulated and measured and is used to find the thermal expansion coefficient in that direction using the equation

$$\alpha_{j=x,y,z} = \frac{\Delta l_i}{l_i * \Delta T} \tag{3.17}$$

Here, α is the thermal expansion coefficient, Δl the change in length due to temperature change ΔT and l the original length. The total deformation of the RVE for the main coil when cooled down to 4.2K from 300K is shown in Figure 3.15. The same RVE structure used to estimating the engineering constants was considered for estimating thermal properties. Table 3.5 lists the thermal expansion coefficient when cooling from 300K to 4.2K.

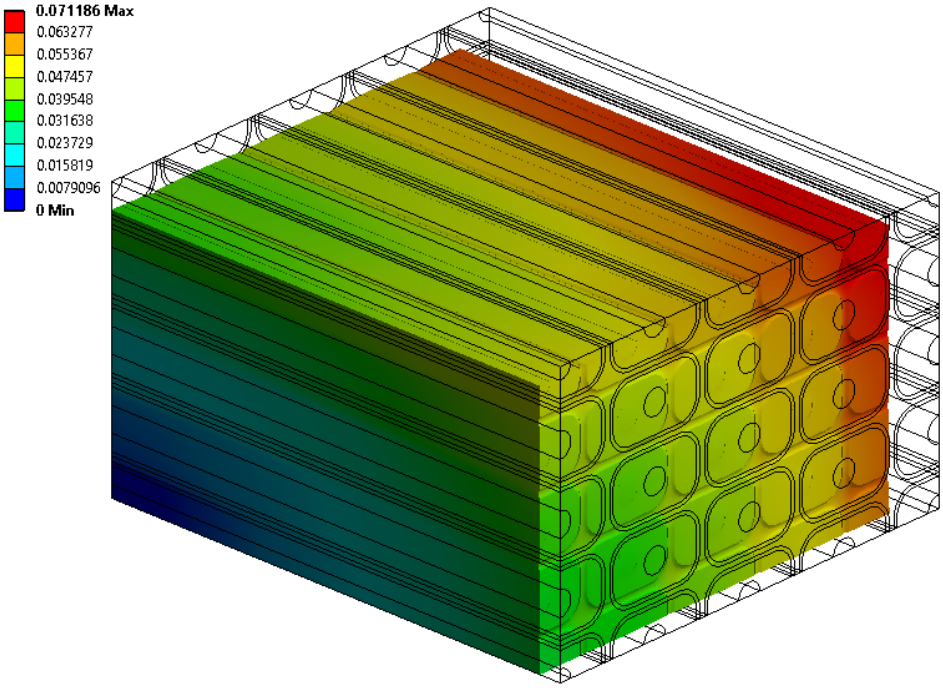

Figure 3.15 Thermal contraction (mm) of the RVE when cooled down from 300 K to 4.2 K. The wireframe shows the RVE at 300 K and the shaded diagram denotes the shrinkage.

Table 3.5 Orthotropic average thermal expansion coefficients of the assumed homogeneus material of the coils from 300 K to 4.2 K

	Main coil	**Shield coil**
α_{radial}	1.99E-05	2.18E-05
α_{circum}	1.24E-05	1.13E-05
α_{axial}	1.94E-05	1.94E-05

3.6 Conclusions

The composite material properties for the main coil and the shield coil are estimated using the Representative Volume Element method. The constituents of both coils are the same, i.e. copper, Nb-Ti superconductor, PET insulation and epoxy (MY750/HY5922). However, the ratio of different components does vary. The orthotropic engineering constants, Young's modulus, Poisson's ratio, shear modulus, along with thermal expansion coefficient are found out. The estimated values are within the upper and lower limits defined by Voigt and Reuss models. The estimated properties would be used as input in further simulations.

CHAPTER 4

ELECTROMAGNETIC DESIGN AND ANALYTICAL MODEL FOR FORCE CALCULATION

4.1 Superconducting Solenoid Magnet

André-Marie Ampère, a French physicist, coined the term solenoid to designate a helical wound coil. The magnetic field generated by a current carrying conductor relating the magnetic field with the current flowing in a loop is derived from the Ampere's circuit law. Ampere's law states that for any closed loop path, the integral of the length elements (dl) times the magnetic field (B) in the direction of the length element is equal to the permeability (μ_0) times the electric current (i) enclosed in the loop and given by the equation

$$\oint B\, dl = \mu_0 I \tag{4.1}$$

The direction of the field can be found using Ampere's right-hand rule as shown in Figure 4.1. In case of a wound solenoid, with current flows flowing along the fingers, the direction of the magnetic field will be along the thumb.

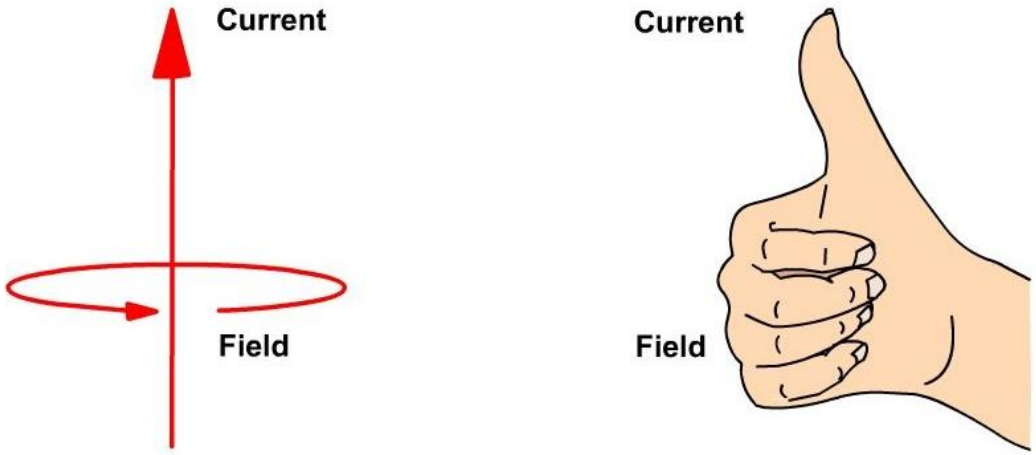

Figure 4.1 A depiction of Ampere's right-hand rule showing the relation of the direction of current flow and magnetic field generated in a conductor.

A solenoid, as a magnet design, is a type of electromagnetic coil which produces an axial magnetic field in a volume of space when an electric current flows through the coil. The magnetic field at the centre of a solenoid is given by the relation,

$$B_0 = \mu_0 \lambda \, N \, I \tag{4.2}$$

where N is the turn density (turns/m) and λ is the packing factor of the winding of the solenoid.

The packing factor signifies the actual conductor area in the whole winding area. Though equation 4.2 is valid for an infinite long solenoid, it is a good approximation even for a finite solenoid. The packing factor of a solenoidal coil can be estimated using the ratio of the area, which is given by

$$\lambda \; = \; \mathrm{n} \times \mathrm{A_{Nb-Ti}} \, \mathrm{h} \, \mathrm{L} \tag{4.3}$$

where A_{NbTi} is cross-sectional area of the conductor, n is the number of turns of the multi-filamentary Nb-Ti conductors used in the winding, and h is the thickness of the solenoid coil and L is the winding length of the coil.

The value of packing factor would always be less than one as the whole winding area includes the superconductor, epoxy, voids and any inter-layer insulation.

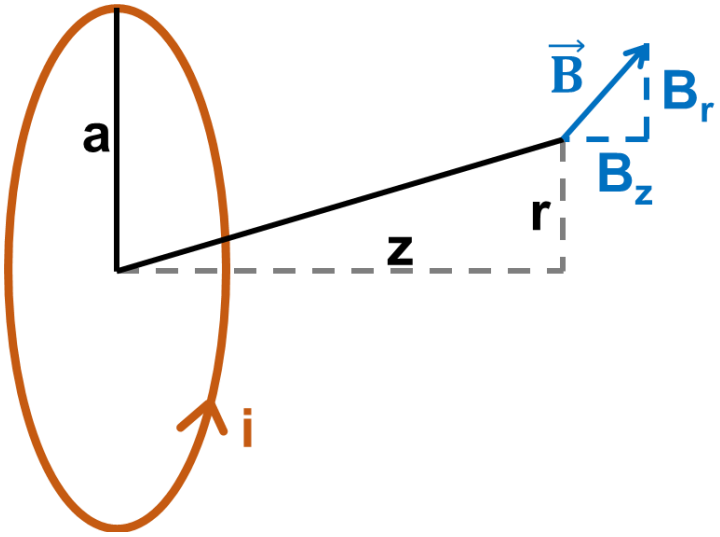

Figure 4.2 A current carrying conductor and a point in space in relation to the centre of the loop experiencing the magnetic field generated by the loop.

Now, considering a single loop of wire carrying current *i* (Figure 4.2), the magnetic field created by a current loop at a point outside the current flowing region can be calculated as

$$B_z = \frac{\mu_0 i}{2\,\pi\,a\,\sqrt{(1+\alpha)^2+\beta^2}}\left[E(k)\frac{1-\alpha^2-\beta^2}{(1+\alpha)^2+\beta^2-4\alpha}+K(k)\right] \tag{4.4}$$

$$B_r = \frac{\mu_0 i\,\gamma}{2\,\pi\,a\,\sqrt{(1+\alpha)^2+\beta^2}}\left[E(k)\frac{1+\alpha^2+\beta^2}{(1+\alpha)^2+\beta^2-4\alpha}-K(k)\right] \tag{4.5}$$

$$k = \sqrt{\frac{4\,\alpha}{(1+\alpha)^2+\beta^2}} \tag{4.6}$$

Where, $\alpha = \frac{r}{a}$ and $\beta = \frac{z}{a}$ and $\gamma = \frac{z}{r}$

i is the current in the loop wire

a is the radius of the loop

μ_0 is the permeability constant (4π x 10^{-7})

x is the distance in the axial direction from the centre of the current loop to the field measurement point.

r is the distance in the radial direction from the axis of the current loop to the field measurement point.

K(*k*) is the complete elliptic integral function of the first kind, and E(*k*) is the complete elliptic integral function of the second kind. These elliptic integral functions are defined in the range of 0 to1 as

$$K(k) = \frac{\pi}{2}\sum_{n=0}^{\infty}\left(\frac{(2n-1)!!}{(2n)!!}\right)^2 k^{2n} \tag{4.7}$$

$$E(k) = \frac{\pi}{2}\left[1 - \sum_{n=0}^{\infty}\left(\frac{(2n-1)!!}{(2n)!!}\right)^2 \frac{k^{2n}}{2n-1}\right] \tag{4.8}$$

The K(*k*) and E(*k*) plots are shown in Figure 4.3 and Figure 4.4 respectively. It may be noted that both functions are reduced to $\frac{\pi}{2}$ when *k* = 0.

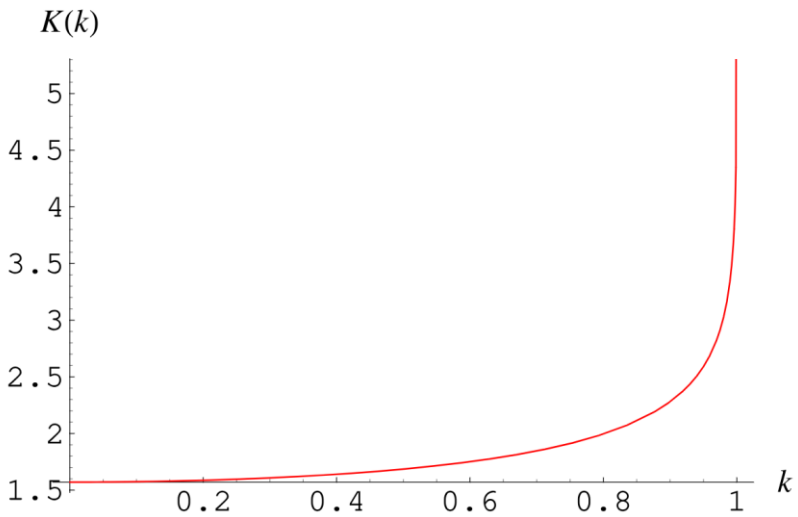

Figure 4.3 The plot of the complete elliptic integral function of the first kind, K(*k*) in the range of 0 to 1.

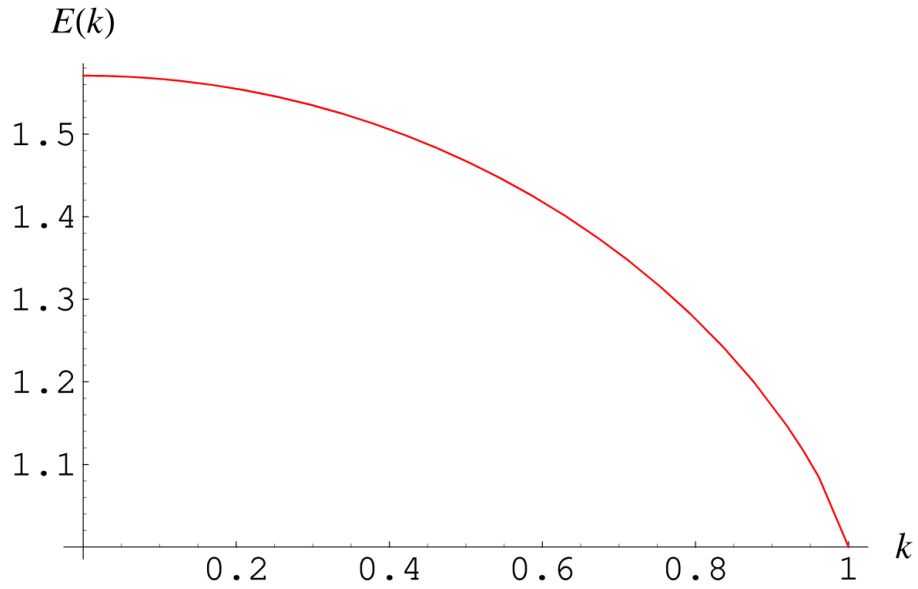

Figure 4.4 The plot of the complete elliptic integral function of the first kind, E(*k*) in the range of 0 to 1.

The axial magnetic field at the centre of a solenoid, B_0 (Tesla), with a rectangular cross-section and uniform current density, can be estimated by the simplified relation[9], [103], [104],

$$B_0 = J\,\lambda\,a\,\mathrm{F}(\alpha,\beta)\,\times\,10^{-6} \tag{4.9}$$

$$F(\alpha,\beta) = \frac{4\pi}{10}\beta\,\log_e\frac{\alpha+\sqrt{\alpha^2+\beta^2}}{1+\sqrt{1+\beta^2}} \tag{4.10}$$

The function F(α,β) is called the Fabry factor or the field factor and gives a parametric view of a magnet's magnetic field and it's geometry. The magnetic field generated by individual coils can be calculated based on equation (4.4 and (4.5. The magnetic field at a point will be the vector summation of the magnetic fields generated by different coils at that point.

The magnet considered for the 1.5 T MRI magnet is of a multi-coil configuration having six primary coils and two active-shield coils which have current running in opposite directions as the primary coils. The coils would be connected in series thus operating at the same current. Depending on the wire chosen, coils will have different current densities. The geometric parameters of the coil are given in the Table 4.1. Figure 4.5 shows the relative positions of each coil.

Table 4.1 The geometric position, size and current density of the MRI coils

Coil No.	Coil Nomenclature	Centre Position		Coil Size		Current Density A/m^2
		Radial mm	Axial mm	Radial mm	Axial mm	
1	Primary Coil	553	-96	42	64	$1.411x10^8$
2	Primary Coil	553	96	42	64	$1.411x10^8$
3	Primary Coil	524	-298	38	82	$1.411x10^8$
4	Primary Coil	524	298	38	82	$1.411x10^8$
5	Primary Coil	536	-622	57	154	$1.411x10^8$
6	Primary Coil	536	622	57	154	$1.411x10^8$
7	Shield Coil	810	-505	74	122	$-1.002x10^8$
8	Shield Coil	810	505	74	122	$-1.002x10^8$

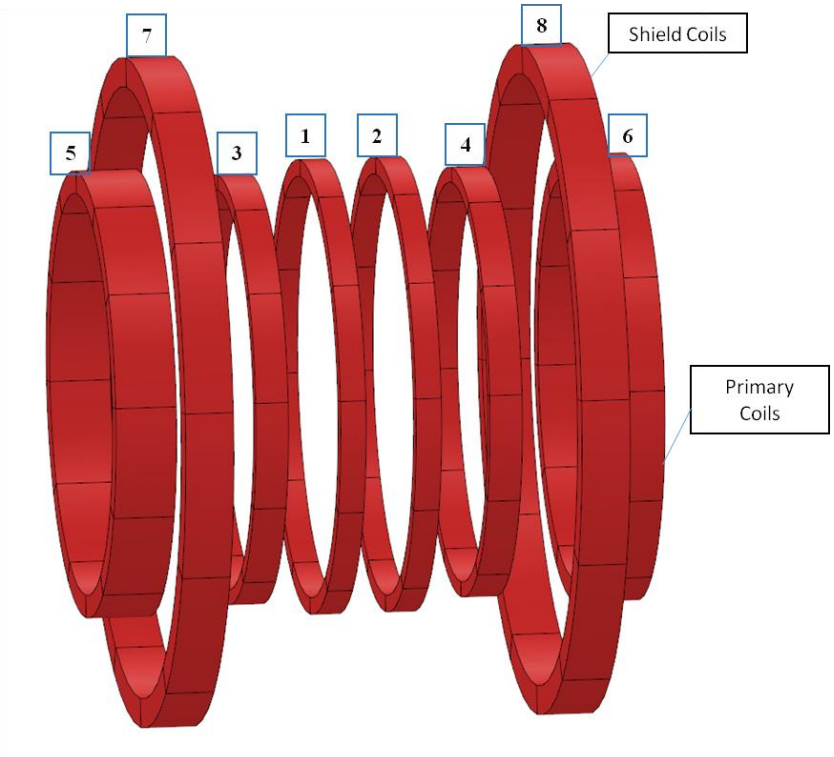

Figure 4.5 The special arrangement of eight superconducting coils in order to achieve the required magnetic field strength and field homogeneity.

If we measure the magnetic field along the z-axis, equation (4.4 can be reduced as

$$B_z = B = \frac{\mu_0 i\, r^2}{2\sqrt{(r^2 + z^2)^3}} \tag{4.11}$$

The combined magnetic field of the eight coils, along the axis, is shown in the Figure 4.6.

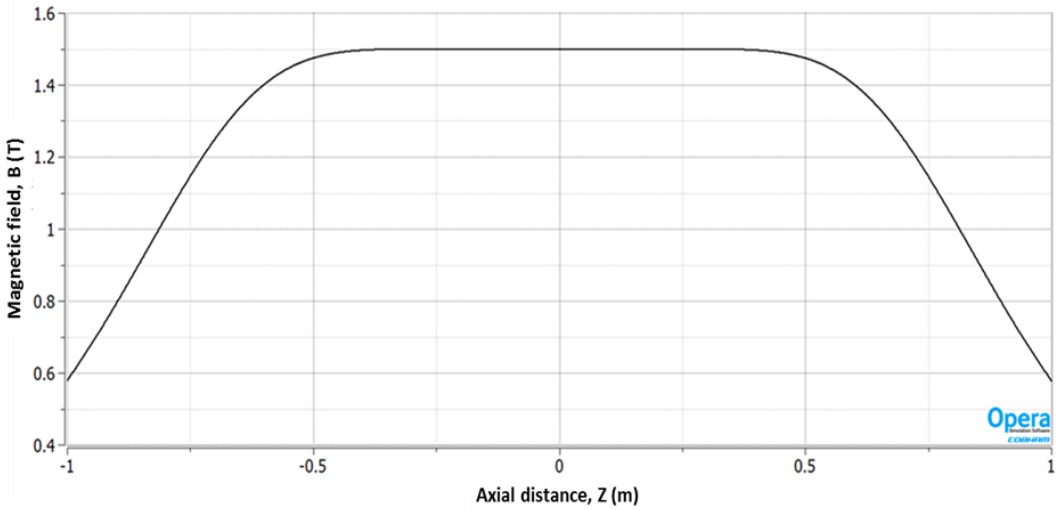

Figure 4.6 The total magnetic field (T) along the central axis of the MRI magnet. The central plateau region is the high homogeneity region.

4.2 Peak Field

Active shield configuration generates a higher peak field in the multi-coil magnet system. Figure 4.7 shows the field profile of the 1.5 T MRI magnet and the concentration of the field on the conductor of the coils. This concentration of field generates a peak magnetic field on every coil. Figure 4.7 shows that the peak field is located close to the coils shown in the red zone in the simulation. For a typical 1.5 T MRI scanner, this peak field can be a factor of three higher than the central magnetic field. This is evident in Figure 4.7, which shows the flux concentration map on different coils. The distribution of flux is not uniform among different coils. The concentration of magnetic flux eventually generates higher peak fields on every coil. The maximum peak field is generated on the outermost primary coils (coils 5&6) and

the shield coils (coils 7&8). Figure 4.7 shows the distribution of the peak field along the axial direction on the inner radii of different coils. For most of the coils, except coils 5&6, the maximum peak field formation is at the axial centre of each coil. For coils 5& 6, the maximum peak field formation is shifted towards the outer edge of the coils and located between the axial centre and the outer edge of each coil. The highest peak field for this design is 4.3 T on the outermost pair (end coils) of the primary coil (coils 5&6).

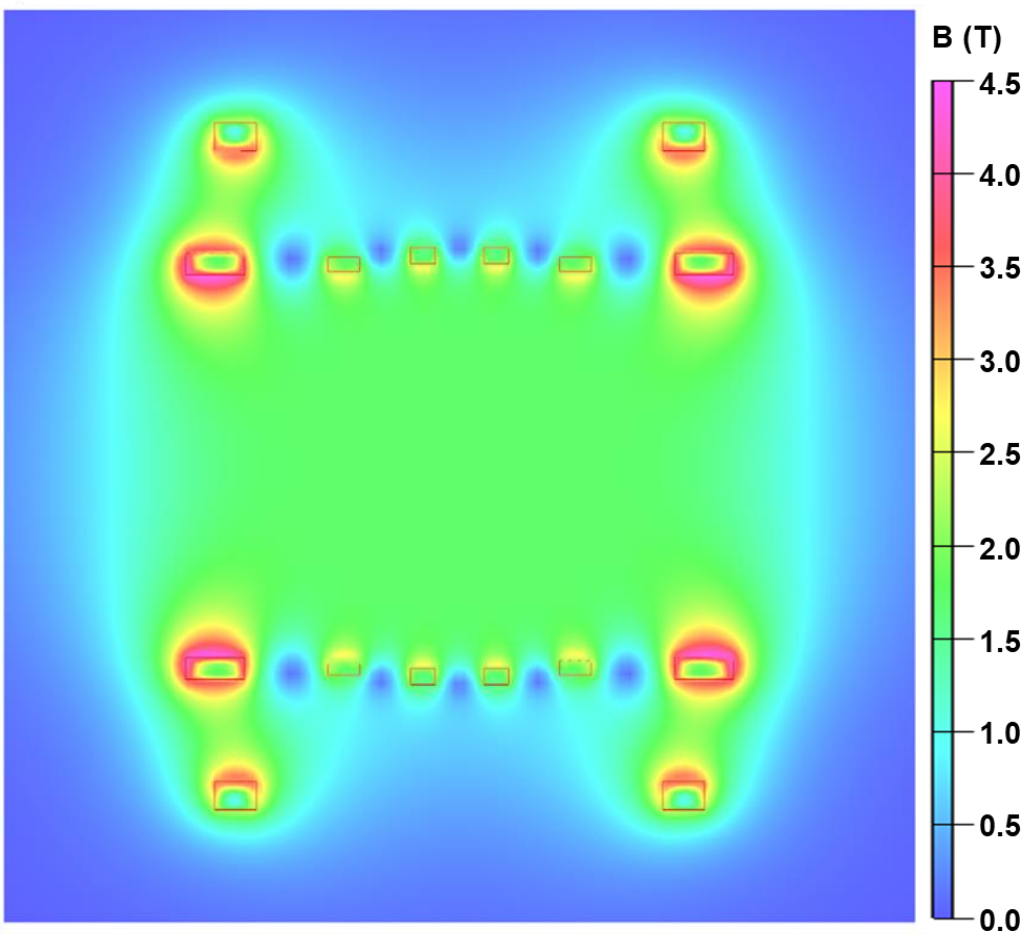

Figure 4.7 Magnetic field distributions (in Gauss) on the Y-Z plane of the 1.5 T MRI magnet.

The maximum peak fields on each pair of coils have been summarized in Table 4.2. The value of the highest peak field for this design is quite reasonable and well within the manageable limit. It can be also seen that due to the close proximity of C5/C6 to C7/C8 the magnetic field around those coils are very high. This presence of high fields around the coil reduces the net forces, while increasing the stress.

Table 4.2 Peak field on different pairs of the coil of the 1.5 T MRI magnet.

Coil No.	Coil	Peak Field (B_p) T
1 & 2	Primary	2.93
3 & 4	Primary	2.92
5 & 6	Primary	4.26
7 & 8	Shield	4.08

4.3 Field Distribution within a Solenoid

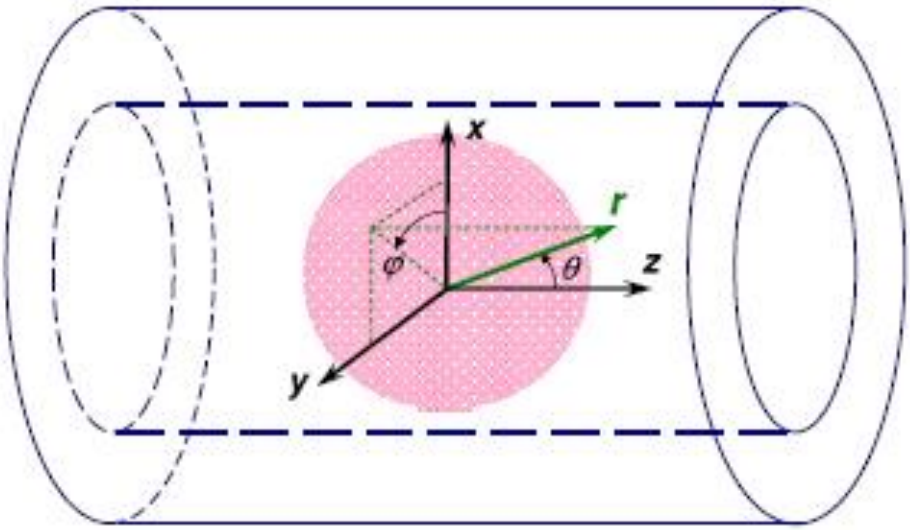

Figure 4.8 Cartesian and spherical coordinate system of a solenoid magnet and a Diametrical Spherical Volume (DSV) at the magnetic centre.

If we consider a spherical region of interest inside the solenoid (Figure 4.8), such that there are no current carrying elements inside the volume, then the distribution of the magnetic field in the current free region (i.e. at the centre of the magnet) can be described by the Laplace equation. The magnetic field is distributed according to the Laplace equation [3]:

$$\nabla^2\left(B_x, B_y, B_z\right) = 0 \tag{4.12}$$

In MRI, the homogeneous magnetic field is along the axial (z) direction. Hence, in the DSV, the total field can be assumed to be equal to the axial component of the magnet field, B_z, thus

$$\nabla^2 B_Z = 0 \tag{4.13}$$

Using the spherical coordinate system (r, θ, φ) as shown in Figure 4.8, the solution of (4.13) can be expressed in terms of spherical harmonics as;

$$B_Z(r, \theta, \varphi) = \sum_{n=0}^{\infty} \sum_{m=0}^{n} r^n \, P_n^m(cos\theta)[A_n^m \cos(m\varphi) + B_n^m \sin(m\varphi)] \tag{4.14}$$

where P_n^m are the associated Legendre polynomials, n represents the zonal harmonics and describes the axial variation of the B_Z field, m signifies the radial harmonics and describes the variation of the B_z field in $x - y$ plane in the cartesian coordinate. A_n^m and B_n^m are the harmonic coefficients in the series expansion, which can be determined by the boundary conditions [105]–[107].

Equation (4.14) can be expanded in the form of the Taylor series, which is given by;

$$\begin{aligned} B_Z = {} & A_1^0 + 2A_2^0\,(z) + \ 3A_2^1\,(x) + 3B_2^1\,(y) \\ & + \frac{3}{2}A_3^0[2Z^2 - (x^2 + y^2)] + 12A_3^1\,(zx) + 12B_3^1\,(zy) \\ & + 15A_3^2(x^2 - y^2) + 30B_3^2(xy) + \cdots \end{aligned} \tag{4.15}$$

$$B_Z = B_0 + 3\ First\ order\ (Linear)\ terms + 5\ second\ order\ terms + 7\ third\ order\ terms + 9\ fourth\ order\ terms + \cdots \quad (4.16)$$

where B_0, the central magnet field of the MRI system, B_0 needs to be as homogenous as possible. All other terms represent field inhomogeneities, which need to be eliminated. First-order terms are the linear distortion terms of the magnetic field in the x, y and z directions. Second-order terms are the field distortion in the xy, zx, zy, z^2 and x^2-y^2 directions. In practice, while the higher order terms can cause a larger variation in the magnetic field, they tend to have lower amplitudes. This usually depreciates the effect the higher order terms have in the overall homogeneity. Thus, in practical magnet design, only orders up to 16 are considered for an eight-coil magnet.

The field created by an ideally aligned axisymmetric coil system has m=0, which makes the 2nd term of the (4.14) equal to zero. If a magnet is symmetric with respect to the $z = 0$ plane, then $A_{2i+1} = 0$ for i= 1, 2... i.e all odd order spherical harmonics are also zero. Six field shaping primary coils, i.e. three pairs of primary coils, represent the most common configuration of MRI scanners, having up to 10th-order harmonics compensated over an DSV region which is usually half of the bore diameter. Considering a 45 cm DSV, the Legendre polynomials of the magnet are given in Table 4.3.

Table 4.3 Values of coefficients of Legendre polynomials calculated for 45 cm DSV.

Order (n)	**45 cm** $\mathbf{A^0_n}$
0	1.499
2	7.89E-07
4	2.33E-06
6	1.56E-06
8	1.73E-06

10	-1.72E-06
12	-2.89E-06
14	1.12E-06
16	-2.14E-07

4.4 Field Homogeneity in a Solenoid

Magnetic field homogeneity is one of the critical performance parameters of any MRI scanner. The commercial standard for reporting homogeneity has been shifting from specifying peak-to-peak homogeneity on the surface of the DSV to specifying the root mean square (RMS) homogeneity. The peak-to-peak magnetic field homogeneity is defined by:

$$\left|\frac{B_{max} - B_{min}}{B_0}\right| \times 10^6 = \left|\frac{\Delta B_0}{B_0}\right| \times 10^6 \ (ppm) \qquad (4.17)$$

where, B_{max},B_{min} and B_0 are the maximum, the minimum and the central magnetic field in the homogeneous field region, respectively. ΔB_0 is the difference between the maximum and minimum of the magnetic field in the desired diametrical spherical volume (DSV). The DSV is also referred to as a good field region or Field of View (FOV).

Figure 4.9 shows the iso-homogeneous lines at the centre of the magnet. It can be seen that the 6 ppm line touches the 45 cm DSV line in few places, thus giving a design of 6 ppm. Figure 4.10 shows the variation in homogeneity in three different FOVs, i.e. 30, 40, 45 cm. This can predict the homogeneity in a given DSV to a better accuracy, say 5.5 ppm in 45 cm DSV.

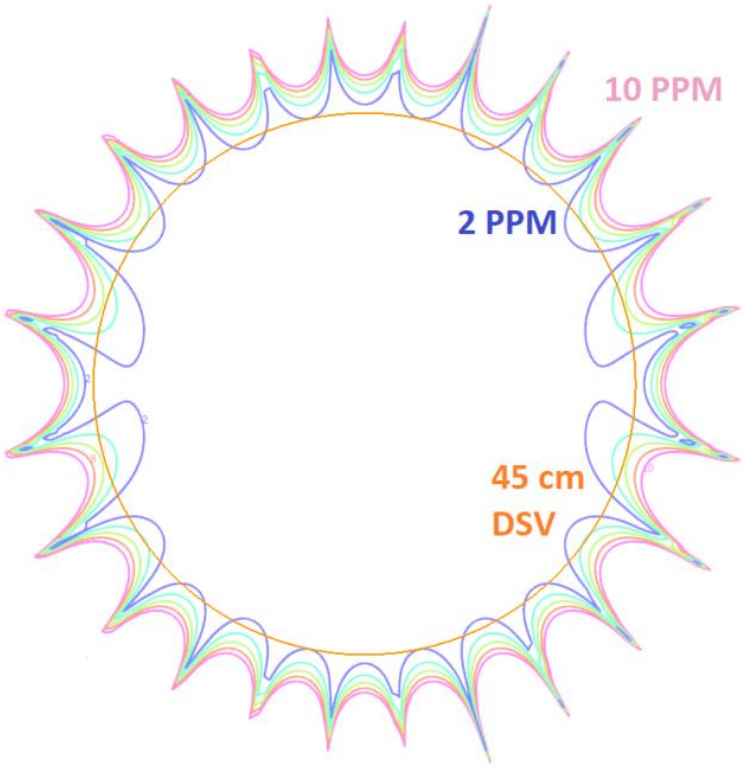

Figure 4.9 Iso-homogeneous lines of 2, 4, 6, 8 and 10 ppm (Purple, Blue, Green, Red, and Pink, respectively). The orange circle represents 45 cm DSV.

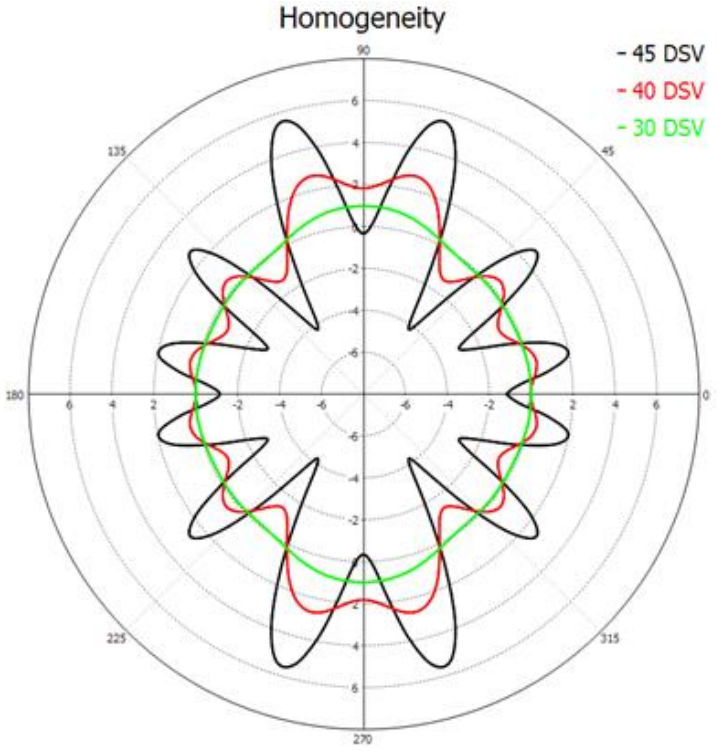

Figure 4.10 Polar chart of the homogeneity on 30 cm (green), 40 cm (red) and 45 cm (black) DSV; each circle represents the iso-homogeneous line .

4.5 Forces in a Solenoid Coil

Any current-carrying conductor placed in a magnetic field would experience electromagnetic or Lorentz forces in the presence of the magnetic field. The magnetic stresses on the conductor are directly dependent on the field they experience inside the winding pack. Hence, a higher peak field on the coil implies high mechanical stresses. The mechanical stress needs to be calculated so that a suitable mechanical structure (bobbin, support, etc.) can be designed for the coil. In order to simulate the effect of Lorentz forces, it is important to calculate the Lorentz forces as body forces distributed in the coil volume. Since the coils are solenoid, the forces can be calculated for a cross-section of the coil, and the problem can be solved as an axisymmetric case. In such a case, the forces would be reduced to a force per unit area (N/m^2) from force per unit volume (N/m^3). The Lorentz force [108], [109] experienced by a current-carrying conductor placed in a magnetic field is given as

$$F_L = J_c \times B \tag{4.18}$$

Here, J_c is the current density, and B is the field experienced by the conductor. Expanding these formulae based on the cartesian coordinates, we get

$$F_x = J_y B_z - J_z B_y \tag{4.19}$$

$$F_y = J_z B_x - J_x B_z \tag{4.20}$$

$$F_z = J_x B_y - J_y B_x \tag{4.21}$$

The coils in the MRI magnet are axisymmetric along the z-axis. Thus, in the components of Lorentz, forces can be calculated in an arbitrary plane passing through the z-axis instead of the whole volume, and the total force can be determined at any point. This also enables representation of the forces as a 2D cases instead of a 3D case as forces are absent in azimuthal direction. If we consider an orthogonal plane, say a y-z plane, we can consider the following boundary conditions:

The current flows perpendicular to the plane, so

$$J_x = J_c \, , J_y = J_z = 0 \tag{4.22}$$

There is no magnetic field perpendicular to the plane, i.e. parallel to the current flow direction.

$$B_x = 0 \tag{4.23}$$

Applying these conditions, the forces can be calculated as

$$F_x = 0 \tag{4.24}$$

$$F_y = - J_c \, . B_z \tag{4.25}$$

$$F_z = J_c \, . B_y \tag{4.26}$$

These equations can be generalized into a cylindrical coordinate system where the x and y axis are radial (r) directions,

$$F_r = - J_c \, . B_z \tag{4.27}$$

$$F_z = J_c \, . B_r \tag{4.28}$$

The axial and radial components of the Lorentz force at any point can be found out as

$$F_r = J_\theta \times B_z \tag{4.29}$$

$$F_z = J_\theta \times B_r \tag{4.30}$$

The force distribution inside the coil can vary in both magnitude and direction depending on the magnetic field at that point. The opposing forces may squeeze the turns together or try to separate them, causing overall compressive or

tensile stresses in the coils. The net force acting on a coil is also crucial as this force will be acting on the bobbin structure and will be responsible for the stresses in the bobbin. The net force on each coil can be calculated as a volume integral of the body force density, *F*, over each coil.

$$f_L = \int_V F = \int_V J \times B \tag{4.31}$$

If we consider the body forces at discrete points inside the coil cross-section, eqn (4.31) can be written as,

$$f_L = 2\pi \frac{A}{n} \times \sum_n (F.r) \tag{4.32}$$

Where *r* is the radius of a point, *A* is the cross-section area of the coil, and *n* is the number of discrete points considered in the cross-section. The forces in coil six are shown in Figure 4.11. The arrowheads show the direction of force, and the colour represents the magnitude. It may be noted that there is no force present in the azimuthal direction.

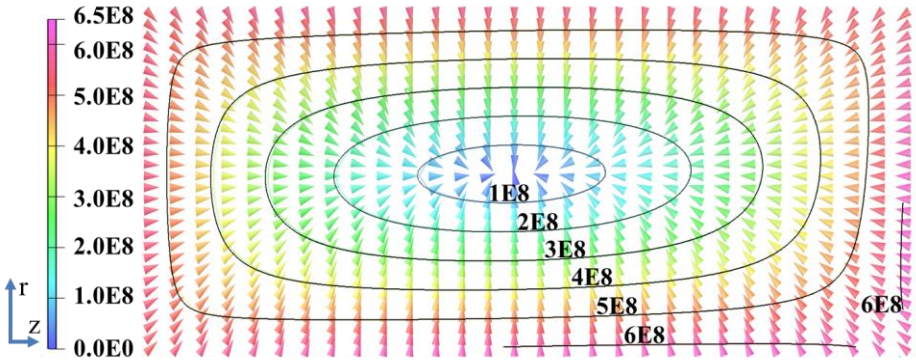

Figure 4.11 The magnetic force density (N/m^3) plotted in coil 6. The arrow heads denote the direction of the magnetic vector, and the colour represents the magnitude.

The forces on different coils were calculated using an integral method in the OPERA-TOSCA simulation. The calculated values of electromagnetic forces on different coils have been summarized in Table 4.4. The (+) ve sign indicates the force towards (+) ve Z –axis, and the (-) ve sign indicates the force towards (-) ve Z −axis.

Figure 4.12 shows the pictorial representation of the electromagnetic force on each 1.5T magnet system coil. It shows that all the primary coils experience a net force towards the mid-plane or iso-centre of the magnet. The outermost primary coils (Coil-5 & 6) experience the maximum axial force of 543.7 kN. Overall, the primary magnet structure experiences a compressive force. The axial forces are comparatively less and directed axially outward for the shield coils, as shown in Figure 4.12.

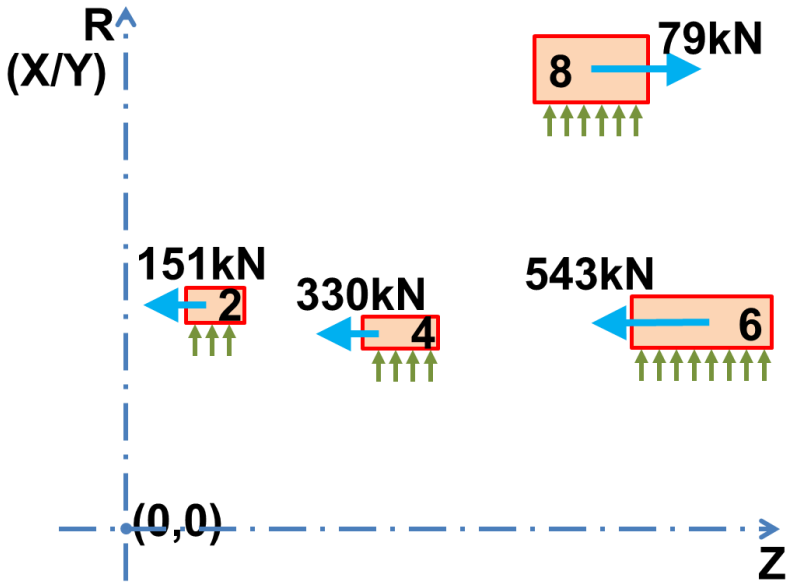

Figure 4.12 Net Lorentz forces generated in each coil at the full operating current of the magnet. Only one half of the coil pair is shown and the forces on the conjugate pair would be equal and opposite.

In order to validate the analytical model, the calculated net forces can be compared to the values obtained via a commercial solver, OPERA FEA [110]. While OPERA can calculate the net forces, it cannot produce them in a form that can further be used for analysis i.e. body forces. Table 4.4 compares the net axial force values between the model presented and OPERA FEA simulated results. It can be seen that the analytical model is in good agreement with the values obtained through the commercial solver.

Table 4.4 Comparison of net axial forces in each coil between the analytical model and OPERA FEA. The +ve and -ve values denote the direction of force concerning the z-axis

Coil	**Net Axial Force (kN) Analytical Model**	**Net Axial Force (kN) Biot Savart method (TOSCA)**
Coil 1	151.522	151.603
Coil 2	-151.522	-151.603
Coil 3	330.629	330.788
Coil 4	-330.629	-330.786
Coil 5	543.659	543.463
Coil 6	-543.659	-543.456
Coil 7	-79.609	-79.783
Coil 8	79.609	79.783

4.6 Hoop Stress

Hoop stress is another important parameter for any MRI magnet. The hoop stress (σ_θ) for a circular coil from the Lorentz forces can be calculated by eqn (4.33), which is given by;

$$\sigma_\theta = B \cdot J \cdot R_{coil} \tag{4.33}$$

where *B* is the field experienced by the conductor, *J* is the current density, and R_{coil} is the radius of the coil.

The field is not uniform throughout the winding cross-section when considering a thick coil. In order to calculate the average stress in a coil, the value of

B_{avg} in (4.33 has been calculated by averaging the maximum and minimum values of the magnetic field. Similarly, the R_{coil} has been calculated by averaging the radius of the winding pack. Thus, eqn 4.33 can be written as

$$\sigma_\theta = B_{avg} \cdot J \cdot R_{coil} \tag{4.34}$$

where B is the average field experienced by the conductor, J is the current density, and R_{coil} is the radius of the centroid of the coil. Table 4.5 summarizes the values of hoop stress on different coils of the 1.5T magnet. The shield coils experience a maximum hoop stress of about 52.86 MPa. Although the peak field on the shield coil is less in comparison to the outermost primary coils (Coil 5 & 6), the diameter of the shield coil is larger (R_{shield} ~1.5$R_{coil\text{-}5,6}$). Hence, the shield coil experiences higher hoop stress than the end-most primary coils.

Table 4.5 The values of maximum hoop stress as calculated by the proposed model on different coils of the 1.5T magnet.

Coil	**Hoop Stress (MPa)**
Coil 1	31.53
Coil 2	31.53
Coil 3	31.67
Coil 4	31.67
Coil 5	22.50
Coil 6	22.50
Coil 7	52.86
Coil 8	52.86

For higher hoop stresses on the shield coils, it is recommended to use an Nb-Ti conductor with a higher ratio of copper. These electromagnetic forces are one of the limiting factors for any MRI magnets, and these forces need to be taken care of by designing a proper mechanical structure and choosing a suitable wire-in-channel (WIC) conductor that can withstand higher stress.

The stresses in the coils are also simulated using commercial FEA packages (ANSYS, OPERA FEA). The thermal stresses due to cooldown from 300 K to 4.2 K and the effect of Lorentz forces are simulated separately, and the combined effect is also calculated. The data is plotted for each coil along a median line starting from the inner radius of the bobbin to the outer radius of each coil.

It can be seen from Figure 4.13 (b) that the calculated hoop stress matches the simulated results in Table 4.5. Figure 4.13 also shows the radial stress (a), axial stress (c) and radial deformation (d) due to thermal cooldown from 300 K to 4.2 K. From Figure 4.13 and Figure 5.3, it can be seen that due to the thermal cooldown and the Lorentz forces, there is a gap between the bobbin and the coil. The winding tension and, if required, additional banding is necessary to reduce this gap. The details of winding tension and banding will be discussed later.

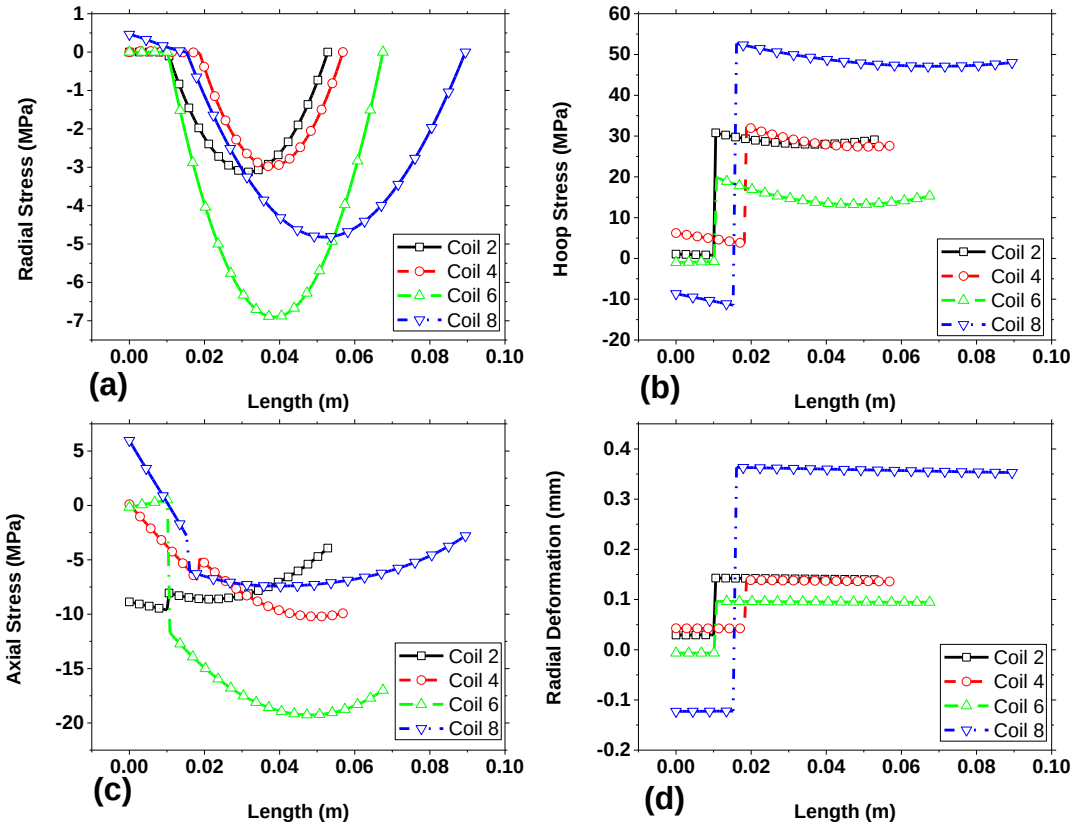

Figure 4.13 Radial stress (a), hoop stress (b), axial stress (c) and radial deformation (d) due to Lorentz forces on each of the four coils along a line from the inner radius of the bobbin towards the outer radius of the coil.

The winding tension is defined in terms of pre-stress applied to the wire during winding. This winding tension corresponds to values in terms of weight, which is the value denoted by most winding machines. The wire is under tension along its

axis during winding. This translates into a tension along the azimuthal direction of the winding. In simulation, since the coil is a closed structure (solenoid), there are no faces to which a force can be applied directly to simulate the winding. This was overcome by using the *inistate* command, which defines the initial state of a body in terms of stress or strain. The winding is a layer-by-layer process, and when each layer is wound, it compresses and displaces the layers beneath it. Thus, at the end of the winding, the whole coil settles into place, distributing the applied pretension along the entire cross-section. This process was modelled using the Element Death and Birth [28], [64], [111]–[113] method in ANSYS. Accordingly, the combined stresses in the magnet are simulated.

The winding machine can operate within a range of 5 to 30 kg. So, the winding tension is to be chosen in that range. Also, it is not preferred to apply high tension on the superconducting wire as it deteriorates the current carrying capacity. If the forces cannot be contained within the defined levels of tension, additional banding is provided. Here, high-strength aluminium alloy (e.g. AA5083, AA6061, etc.) wire is used for banding. Since banding doesn't have restrictions on applied stress, relatively higher winding tensions can be applied to the banding.

4.7 Conclusion

Calculation of Lorentz forces is critical to the analysis of stress in the magnet. Here an analytical model is proposed to calculate the Lorentz forces. The magnetic field is calculated based on elliptic integrals and is used to calculate the magnetic fields in regions where there is no current carrying element. The magnetic field vector is then used to find out the Lorentz forces in the magnet coils. The Lorentz force is calculated as a point forces, which is then fed into the stress simulation as body forces.

Comparing the results of the analytical model to the results produced by commercial FEA software, it can be seen that the analytical code is in good agreement. The net force generated in each coil is compared to results produced in Opera FEA and the hoop stress generated due to Lorentz forces is compared to structural analysis results from Ansys.

CHAPTER 5

OPERATIONAL STRESS AND ITS EFFECTS

5.1 Thermal Stresses

The MRI magnet is operated at cryogenic temperatures of 4.2K. This is achieved by dipping the magnet in liquid helium. The cooldown of the magnet from room temperature (300K) to 4.2K causes deformations in the bobbin and the coils, coil movement and thermal stresses. This can be simulated by FEA modelling in ANSYS thermal. Figure 5.1 and Figure 5.2 show the displacement due to the von Mises stress in the bobbin and helium vessel bore tube coils. Figure 5.3 shows the radial stress, hoop stress, axial stress and radial displacement at the centre of the four coils. From Figure 5.1 and Figure 5.3(d), it can be seen that as the magnet cools down, a gap is generated between the coils and the bobbin. This can also be derived from Figure 5.3(a) where a near-zero radial stress at the point where the coil touches the bobbin, signifying the coil is not excreting any force on the bobbin.

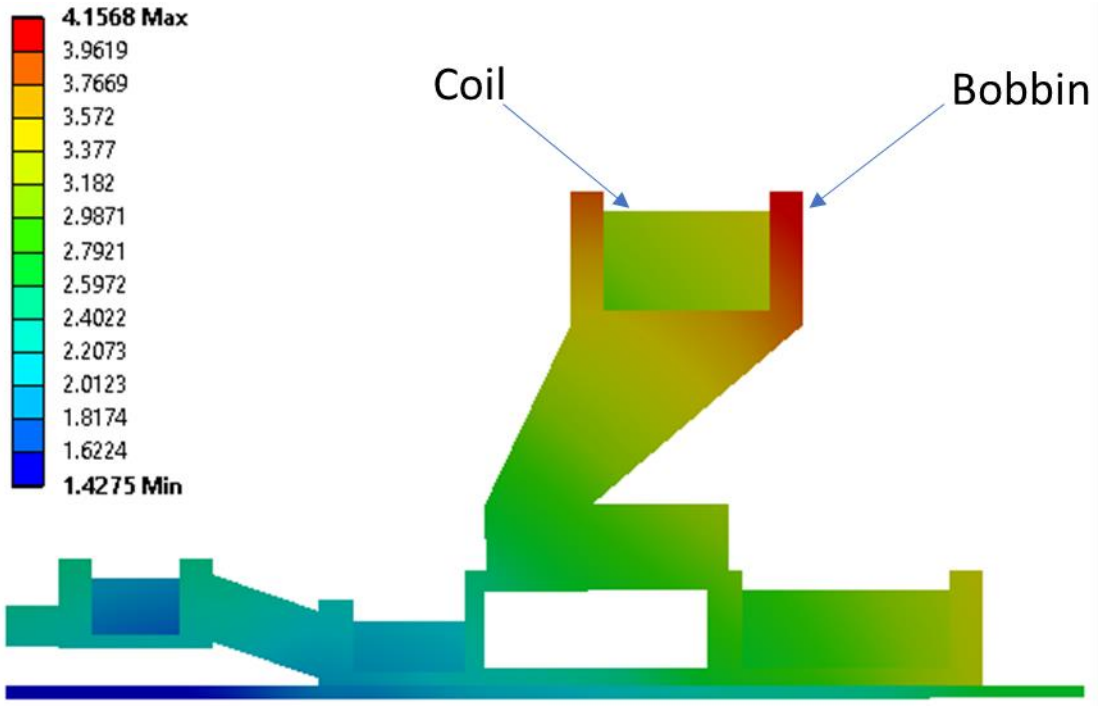

Figure 5.1 Displacement (mm) of the magnet coils and the bobbin due to cooldown from 300K to 4.2K.

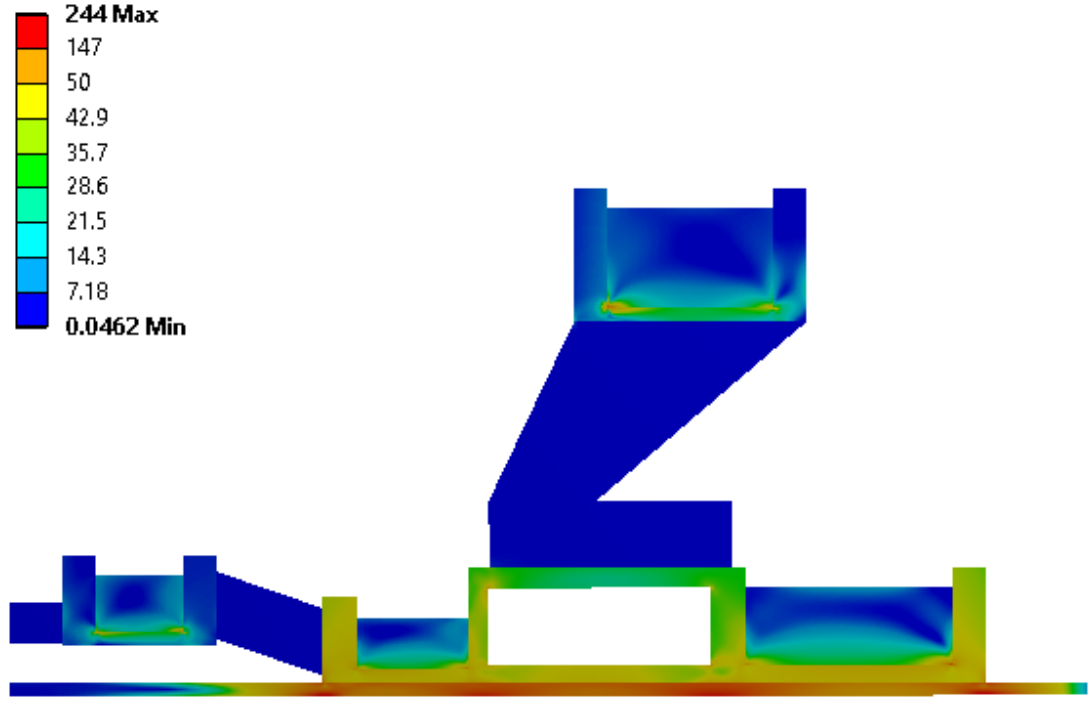

Figure 5.2 von Mises stress (MPa) in the coil, the bobbin and the helium vessel due to thermal cooldown. The peak stresses are experienced in the helium vessel bore, which resists the shrinkage of the bobbin.

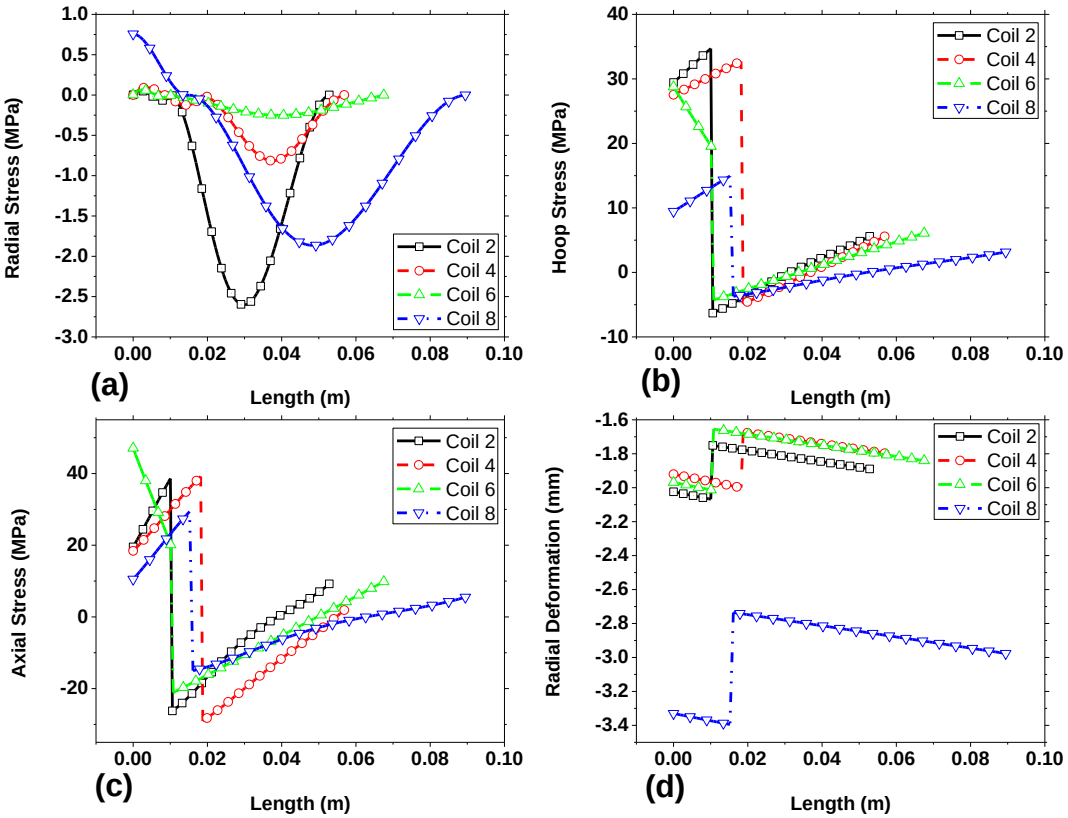

Figure 5.3 Radial stress (a), hoop stress (b), axial stress (c) and radial deformation (d) due to thermal cooldown on each of the four coils along a line from the inner radius of the bobbin towards the outer radius of the coil.

5.2 Winding Tension of Magnet

The thermal stresses and the Lorentz forces acting on the magnet cause relative movement of the bobbin and the coils. This can lead to a gap between the coil and the bobbin, which can then cause a relative movement of coils and a shift in magnetic coordinates. Winding tension is used to counteract the forces acting on the magnet and thus keep the coils pressed onto the bobbin. In case the winding tension in a coil is not enough to manage the forces, an additional banding or overbinding wound at high winding tension may also be provided.

Winding tesnion in a magnet is applied during winding as a tensile force while the wire is in a straight condution. Practically this is attanied using a tensioning element as part of the winding machine.

During operation, the magnet has to bear the complete effect of all three stresses. The direction and the magnitude of these stresses are different, and the combined effect has to fulfil the following conditions;

a. The von Mises stress at any point should be less than the yield stress of the material.
b. The stresses in the coil should be compressive in radial and axial directions. Tensile stresses in these directions will try to de-laminate the coils.
c. The hoop stress in the coil should be tensile and axisymmetric. Compressive stress can cause irregular deformations such as ovality on the coil.
d. The displacements should be minimized yet predictable and preferably linear. Any angular movements of the coil can cause huge inhomogeneity in the magnetic field.

5.3 Methodology

The winding tension is defined in terms of pre-stress applied to the wire or the conductor during the winding. This winding tension corresponds to values in terms of weight, which is the value denoted by most winding machines. The wire is under tension along its axis during winding. This translates into a tension along the azimuthal direction of the winding. In simulation, since the coil is a closed structure (solenoid), there are no faces to which a force can be applied directly to simulate the winding.

This was overcome by using the *inistate* command in Ansys APDL, which defines the initial state of a body in terms of stress or strain. The winding is a layer-by-layer process, and when each layer is wound, it compresses and displaces the layers beneath it. Thus, at the end of winding, the whole coil settles into place, distributing the applied pretension along the entire cross-section. This process was modelled using the *Element Death and Birth* [30], [56] method in ANSYS. The weight applied in the winding machine and its corresponding winding tension for different wires is given in Figure 5.4. Accordingly, the combined stresses in the magnet are simulated.

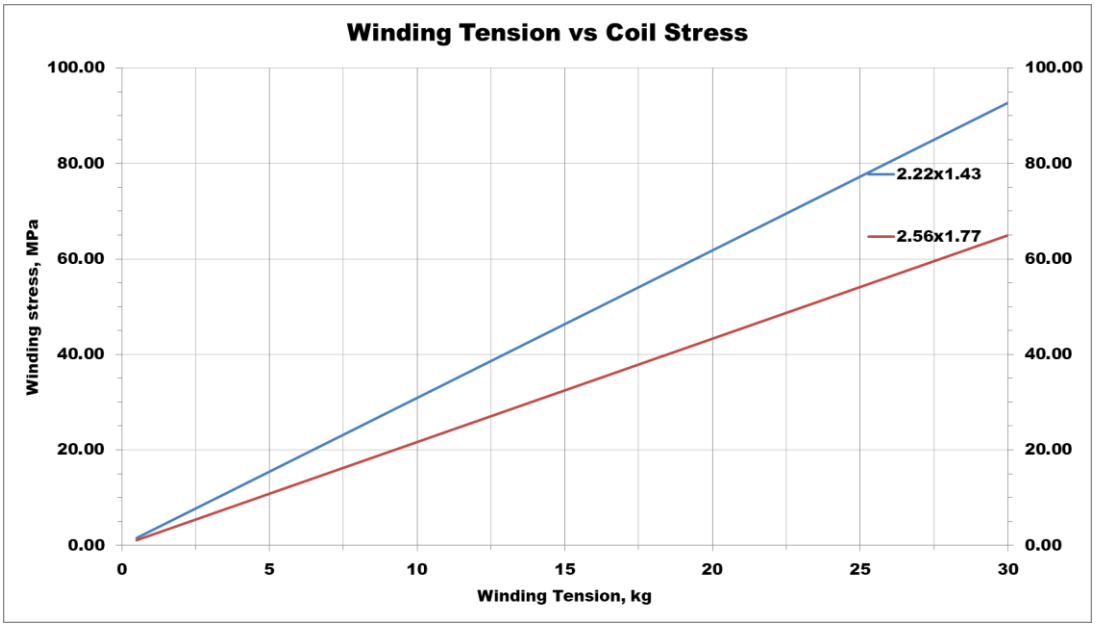

Figure 5.4 Winding tension vs. applied pre-stress in different wires used in MRI magnet.

The winding machine can operate within a range of 5 to 30 kg. So, the winding tension is to be chosen in that range. Also, high tension is not preferred on the superconducting wire as it deteriorates the current carrying capacity [114], [115]. If the forces cannot be contained within the defined levels of tension, additional banding is provided. Here, high strength aluminium alloy (e.g. AA5083, AA6061 etc.) wire is used for banding. Since banding doesn't have any restrictions on applied stress, a relatively higher winding tension can be applied to the banding.

5.4 Winding Tension Simulation

The superconducting wire or conductor is wound under tension to hold the wire in place during winding. After winding, this azimuthal tensile force on the conductor will translate as a radially inward force on the bobbin. An equal and opposite force will act on the winding from the bobbin, and the coil structure can be compared to that of a thick cylinder with inner pressure acting on it. This macroscopic view, however, is an assumption and is not an accurate representation of such a layered structure. In the actual case, each layer in the coil will be a thin cylinder compressing the layers underneath it while being compressed by layers above it.

The 1.5 T superconducting magnet's winding process is modelled using ANSYS, a commercial Finite Element Analysis (FEA) program. The basic equation for the finite element analysis is summarized with the general equation,

$$\sigma = [C]\ \varepsilon \tag{5.1}$$

where, [*C*] is the elastic stiffness matrix, ε represents the elastic strain vector, and σ indicates the stress developed in the geometry. The coil is modelled as layers, with each layer corresponding to a layer in the actual coil that is comprised of the superconducting wire, insulations, and epoxy. The initial state condition is used to apply the pre-strain corresponding to the pre-tension applied on the designated wire. After modelling the entire geometry, a uniform pre-strain is applied to the coil bundle, and all corresponding layer elements are deactivated by setting the stiffness to an ANSYS-defined low value of $1x10^{-6}$ Pa. This is achieved through the kill command in APDL. It may be noted that element *death* command 'anneals' the killed elements so that they contain no stresses when they are brought to life. However, the pre-stress applied initially will still be present. Next, each layer is activated by assigning the stiffness values back to their corresponding material property values, simulating the winding process. This is done using the *alive* command in APDL. This step is repeated for each layer, one by one, simulating the winding process. The ED&B process is not considered turn by turn as the axial winding tension is negligible and has a very minute effect on the state of stress. The ED&B method is superior to other winding simulation models since it is simulating the situation as close to reality, and similar analytical models like the CHCM model [51], [112] are incapable of precisely calculating the stress as the value of the elastic modulus changes due to the change from stainless steel mandrel to coil bundle. The structure of a coil as modelled in ANSYS including the individual layers representing coil and the bobbin is shown is Figure 5.5. Figure 5.6 below shows the complete model of the magnet coils along with the bobbin and helium vessel bore.

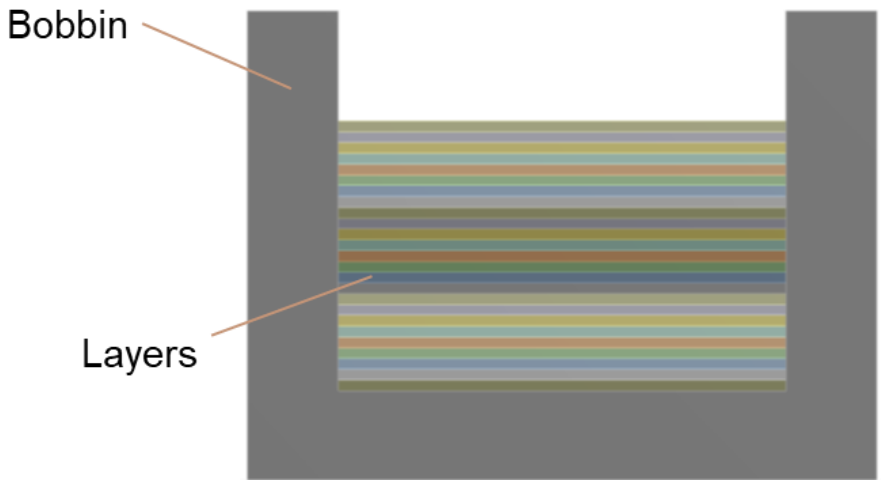

Figure 5.5 Structure of a coil, as modelled in ANSYS. The individual layers representing coil and the bobbin is shown here.

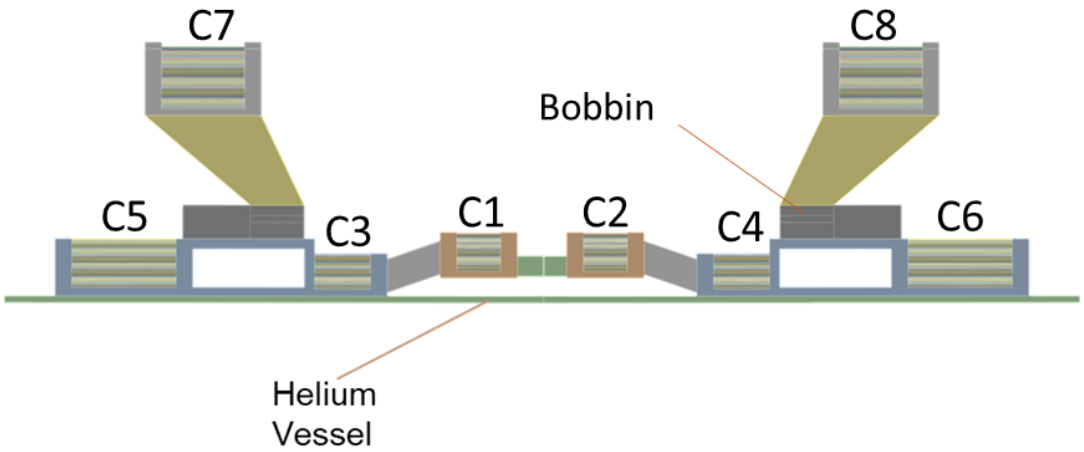

Figure 5.6 The complete model of the magnet coils along with the bobbin and helium vessel bore. The coils are modelled as individual layers.

5.5 Boundary Conditions

In ANSYS simulations, boundary conditions play a pivotal role in replicating real-world scenarios and accurately modelling structural interactions. During the simulation, multiple bodies, such as coils, bobbins, helium vessels etc., interact with each other. In the real world, these bodies are not bound to each other, and they can move with respect to one another. To simulate these conditions accurately, two boundary conditions are considered over the default bonded condition.

Bonded boundary conditions establish a permanent connection between selected surfaces, ensuring they remain in continuous contact throughout the analysis. This setup is ideal for simulating scenarios where components are permanently joined or bonded together, such as welded joints or glued interfaces. By enforcing this constraint, ANSYS accurately captures the behaviour of these bonded structures, enabling engineers to predict how they will respond to various loads and environmental conditions.

Frictional boundary conditions in ANSYS can be further classified into two categories: frictional without separation and frictional with separation. Frictional without separation conditions introduce the effects of friction between contacting surfaces while assuming no separation occurs during the analysis. This allows for simulating sliding and relative motion between components without considering detachment. On the other hand, frictional with separation boundary conditions extend the simulation to include separation between contacting surfaces, allowing for the study of systems where sliding leads to eventual detachment.

When defining a frictional boundary condition, one has to specify the coefficient of friction, a critical parameter that quantifies the resistance to sliding between surfaces. This coefficient represents the ratio of the frictional force between the surfaces to the normal force pressing them together. By adjusting the coefficient of friction, the varying levels of friction observed in different materials and surface conditions, ranging from smooth to rough interfaces, can be replicated. The coefficient of friction plays a significant role in determining the frictional forces' magnitude and the system's resulting behaviour under analysis. Higher coefficients of friction indicate stronger resistance to sliding, while lower coefficients allow for smoother motion between surfaces. The boundary conditions used in the model are marked in the Figure 5.7.

Here, the coefficient of friction is defined as the frictional condition between two sheets of mylar, which would be used as low-friction contact material and insulation between coil and bobbin. Here, a frictional coefficient of 0.35 is used to simulate mylar-to-mylar interaction. Figure 5.8 shows the coefficient of friction for contact between mylar and mylar. [116]

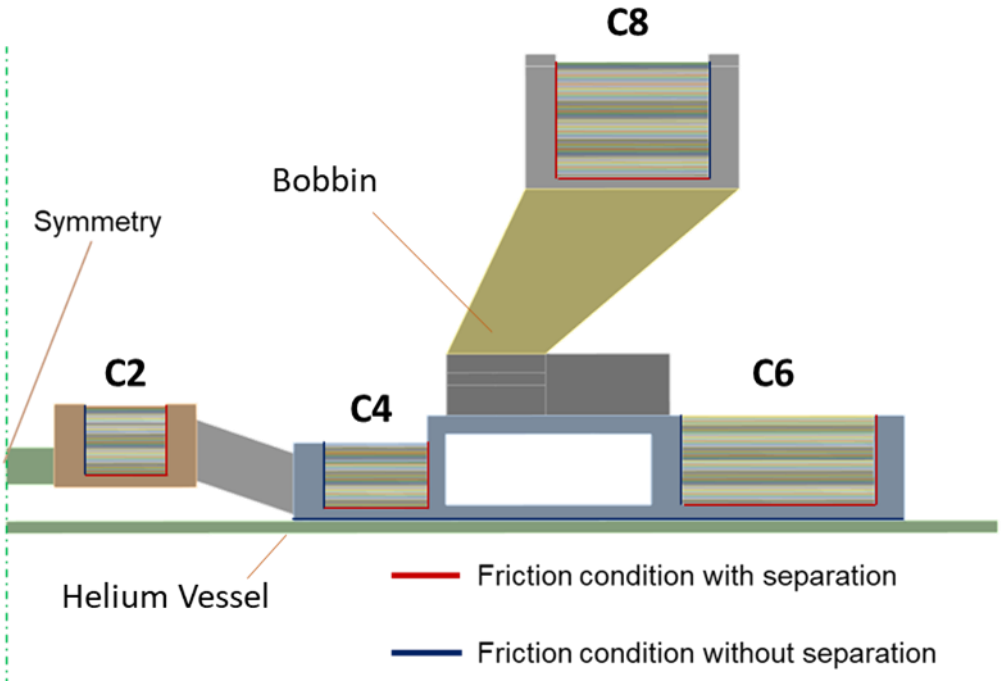

Figure 5.7 Boundary conditions used in the model to simulated various contact conditions between coil & bobbin and bobbin & helium vessel bore.

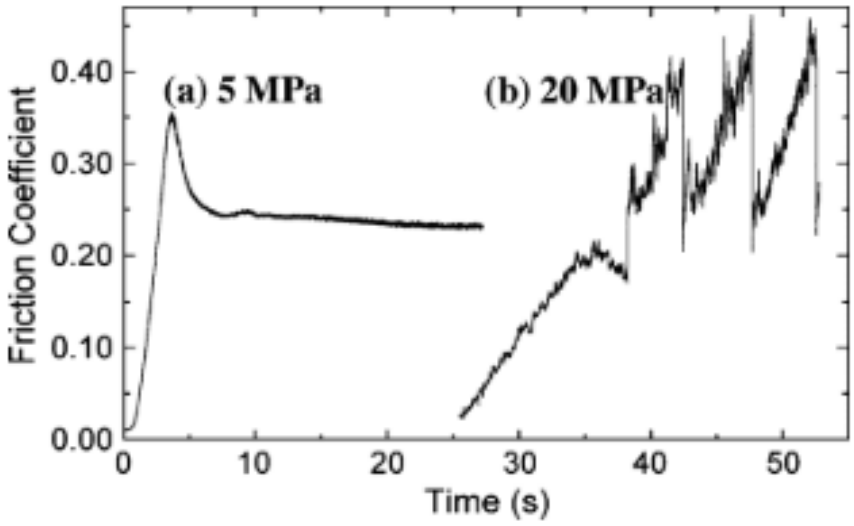

Figure 5.8 Coefficient of friction calculated experimentally for two sheets of mylar rubbing against each other.

5.6 Results

The individual coils of the magnet are analysed separately to estimate the winding tension, number of over binding layers and the winding tension of the over binding. Based on the simulations, the final design of winding tension was done by ensuring the final coil expansion does not leave a gap between the first layer and the former of more than 0.5mm to avoid dropped turns. This value is considered as the half thickness of the smallest dimension in the wire.

5.6.1 Coil 1 & 2

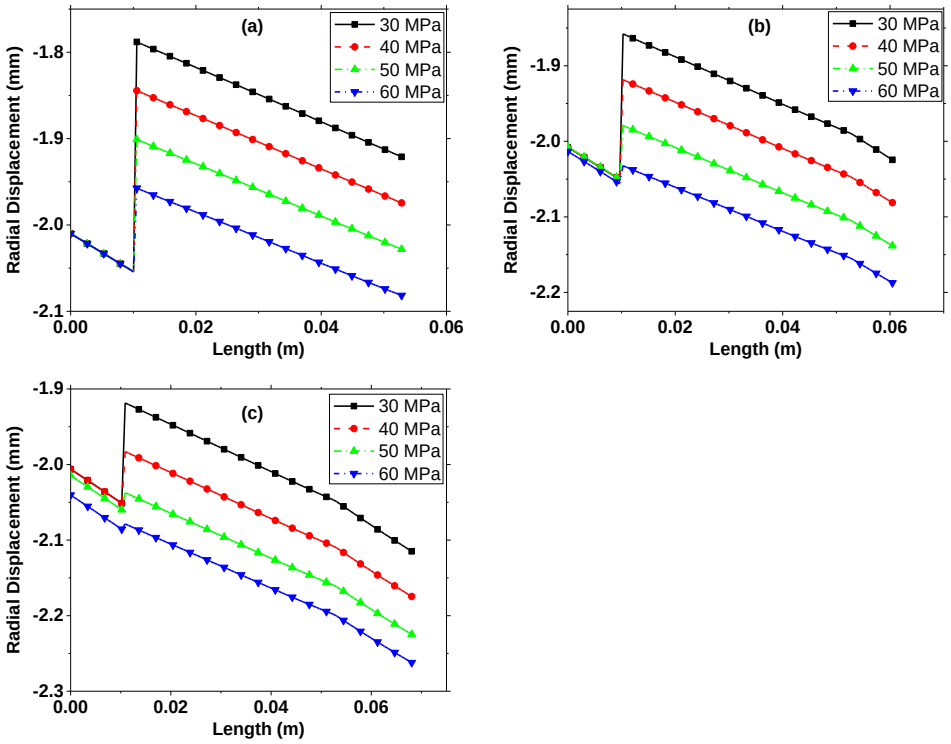

Figure 5.9 Radial displacement of bobbin and coil 1 (& 2) along the median line from inner to outer radius. Three different cases are plotted: (a) without any banding, (b) with five layers of banding and (c) with ten layers of banding using the AA5083 wire of the same size.

It can be seen from Figure 5.9 that the gap becomes zero at ten layers of banding, wound at 60 MPa. Additionally, a higher winding tension may be provided to the banding to provide a safety factor. Figure 5.10, Figure 5.11 and Figure 5.12 show the radial stress, hoop stress and axial stress, respectively, in coil 1 & 2.

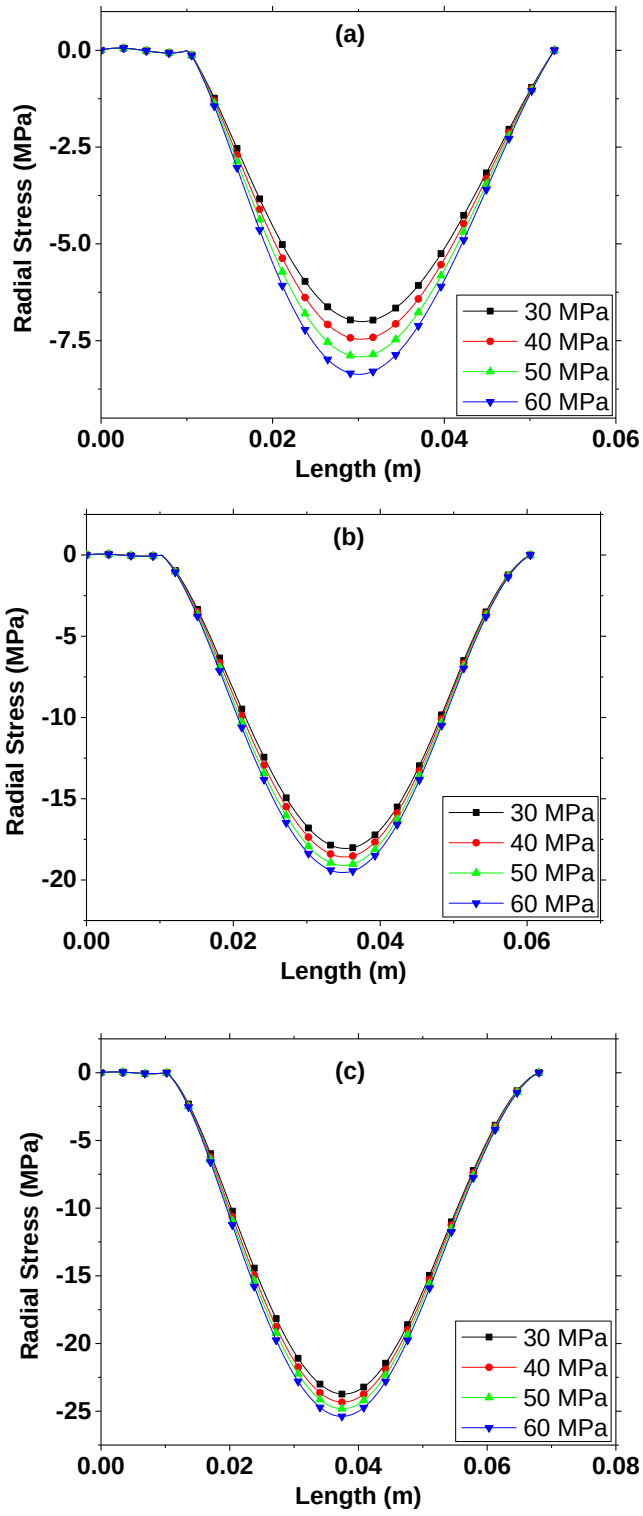

Figure 5.10 Radial stress of bobbin and coil 1 (& 2) along the inner to outer radius median line. Three different cases are plotted: (a) without any banding, (b) with five layers of banding and (c) with ten layers of banding using the AA5083 wire of the same size.

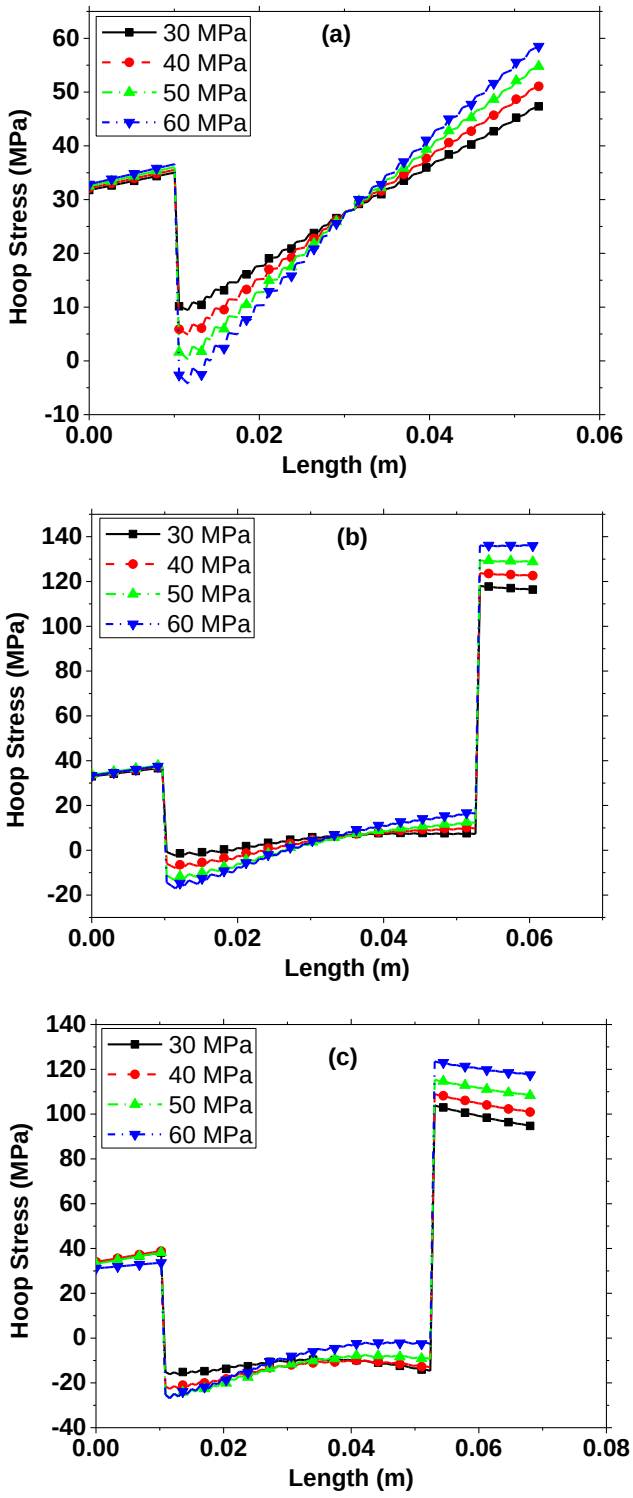

Figure 5.11 Hoop stress of bobbin and coil 1 (& 2) along the inner to outer radius median line. Three different cases are plotted: (a) without any banding, (b) with five layers of banding and (c) with ten layers of banding using the AA5083 wire of the same size.

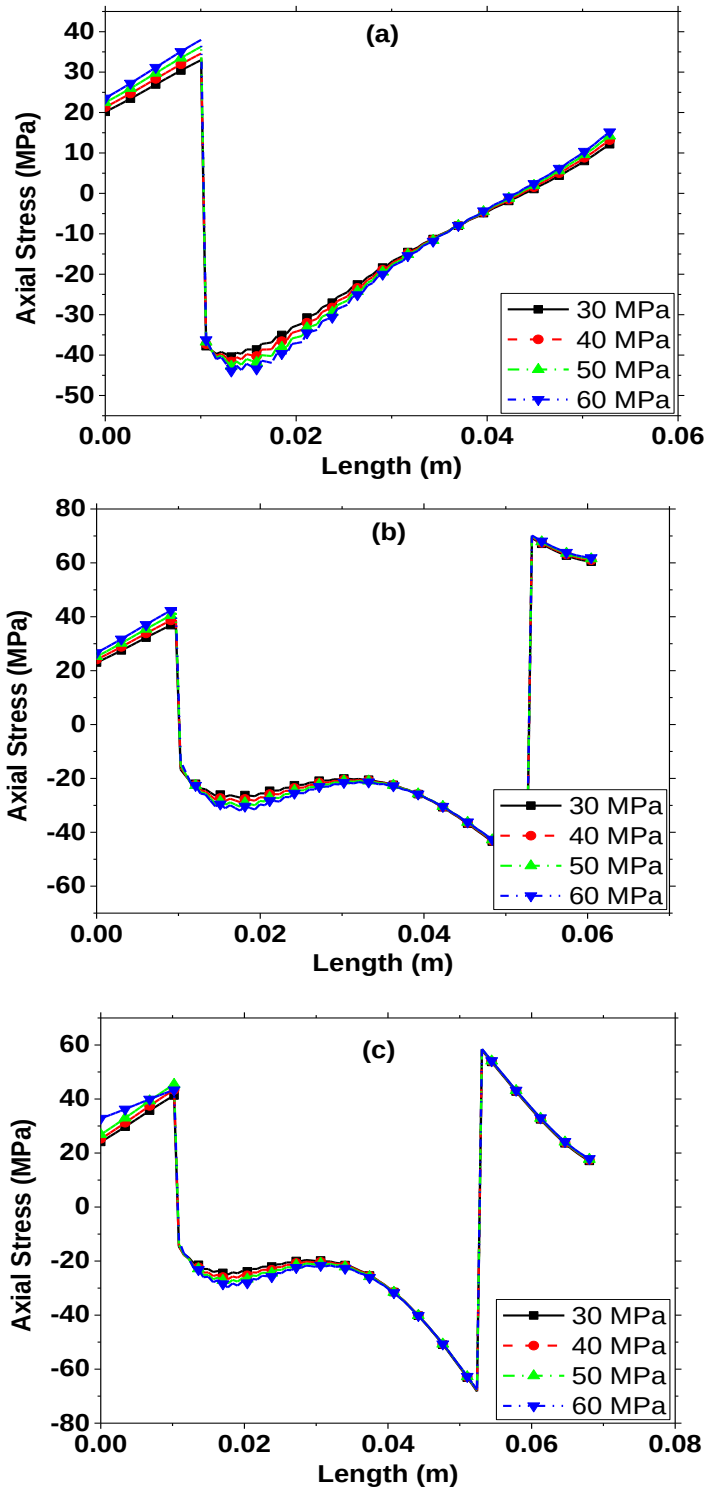

Figure 5.12 Axial stress of bobbin and coil 1 (& 2) along the inner to outer radius median line. Three different cases are plotted: (a) without any banding, (b) with five layers of banding and (c) with ten layers of banding using the AA5083 wire of the same size.

5.6.2 Coil 3 & 4

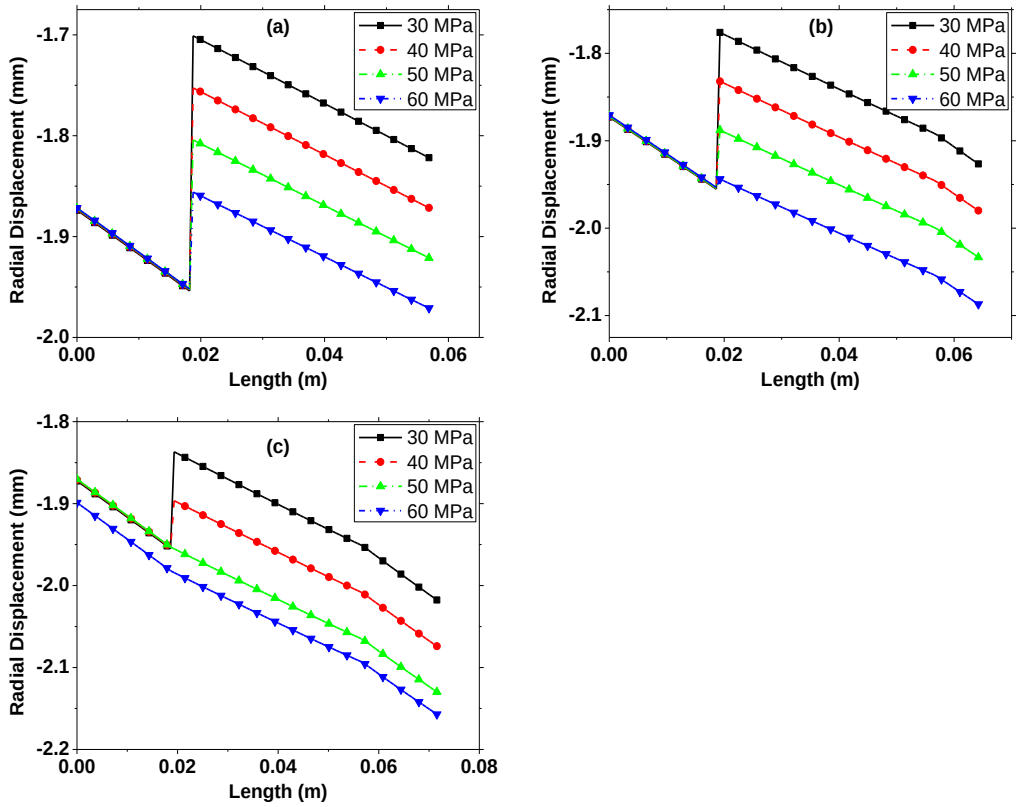

Figure 5.13 Radial displacement of bobbin and coil 3 (& 4) along the median line from the inner to the outer radius. Three different cases are plotted: (a) without any banding, (b) with five layers of banding and (c) with ten layers of banding using the AA5083 wire of the same size.

From Figure 5.13 it can be seen that the gap becomes zero at ten layers of banding, wound at 60 MPa. Additionally, a higher winding tension may be provided to the banding so as to provide a safety factor. Similar to Coil 1 & 2, Coil 3 & 4 has relatively low peak fields. However since the net radial forces are higher, Coil 3 & 4 also require high winding tension. Figure 5.14, Figure 5.15 and Figure 5.16 show the radial stress, hoop stress and axial stress, respectively, in coil 3 & 4.

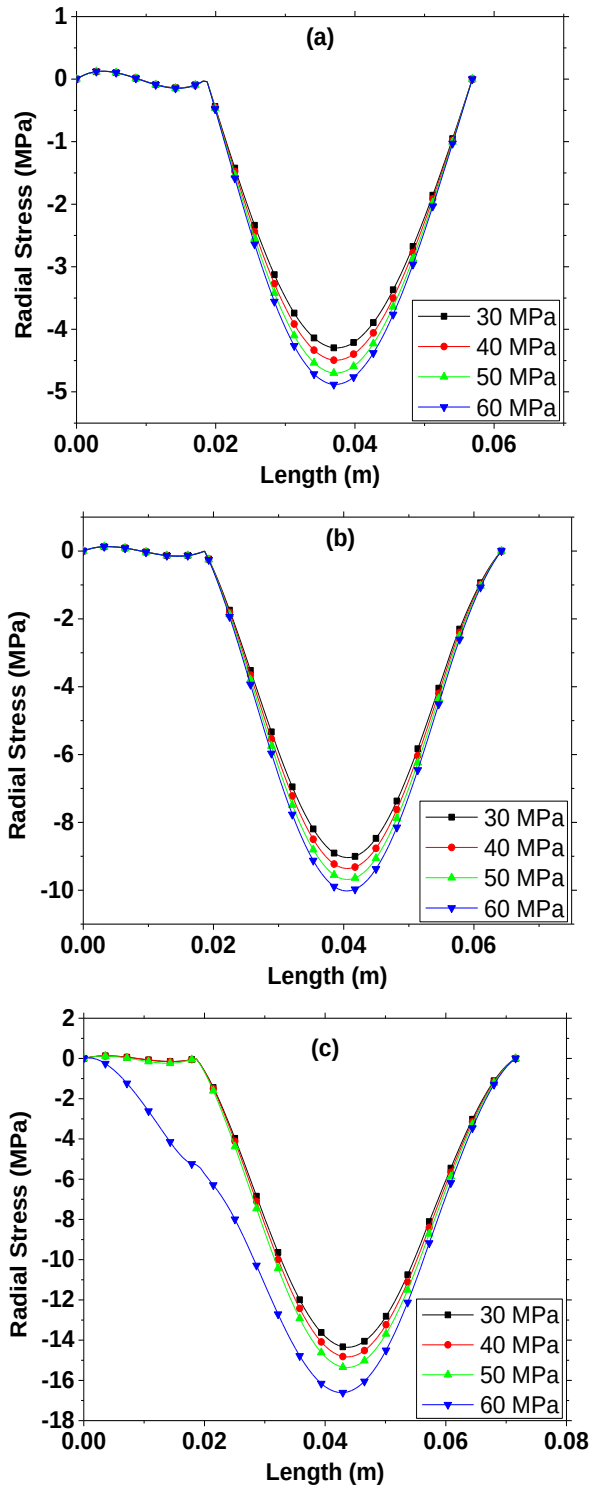

Figure 5.14 Radial stress of bobbin and coil 3 (& 4) along the median line from inner to outer radius. Three different cases are plotted: (a) without any banding, (b) with five layers of banding and (c) with ten layers of banding using the AA5083 wire of the same size.

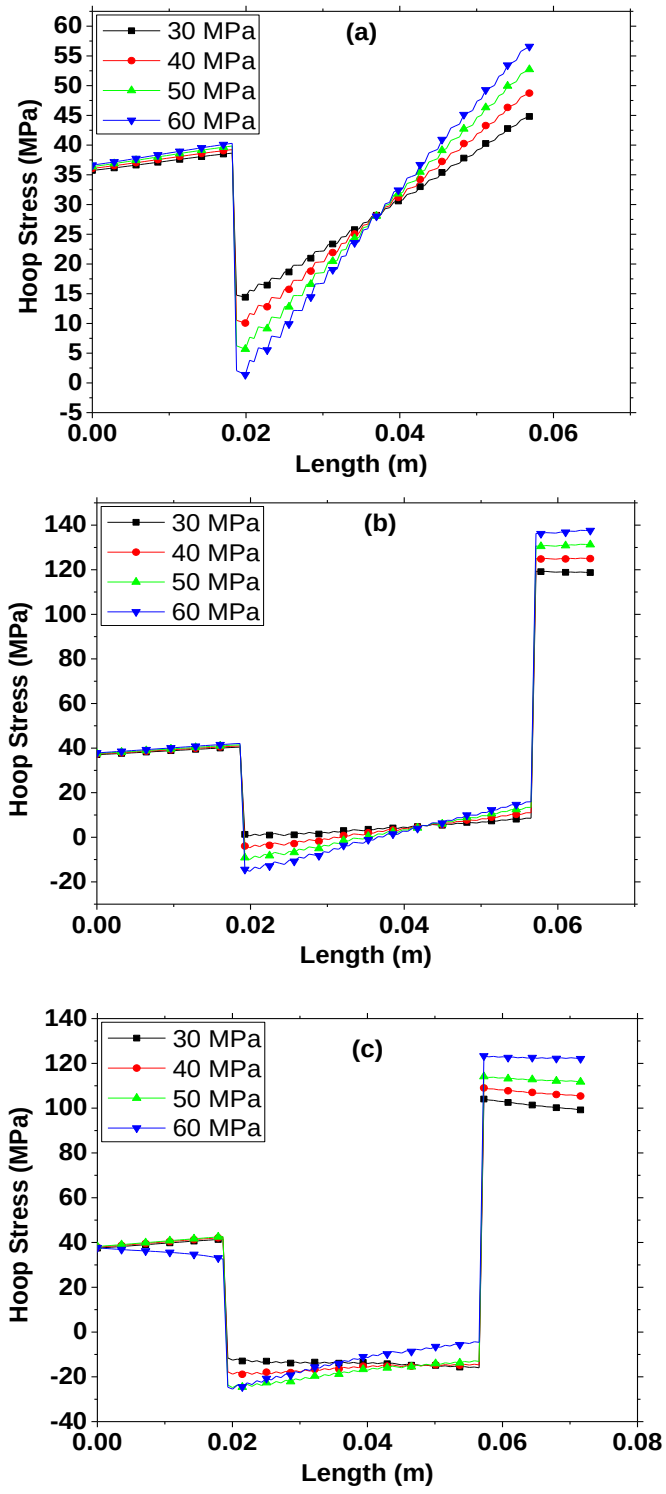

Figure 5.15 Hoop stress of bobbin and coil 3 (& 4) along the median line from inner to outer radius. Three different cases are plotted: (a) without any banding, (b) with five layers of banding and (c) with ten layers of banding using the AA5083 wire of the same size.

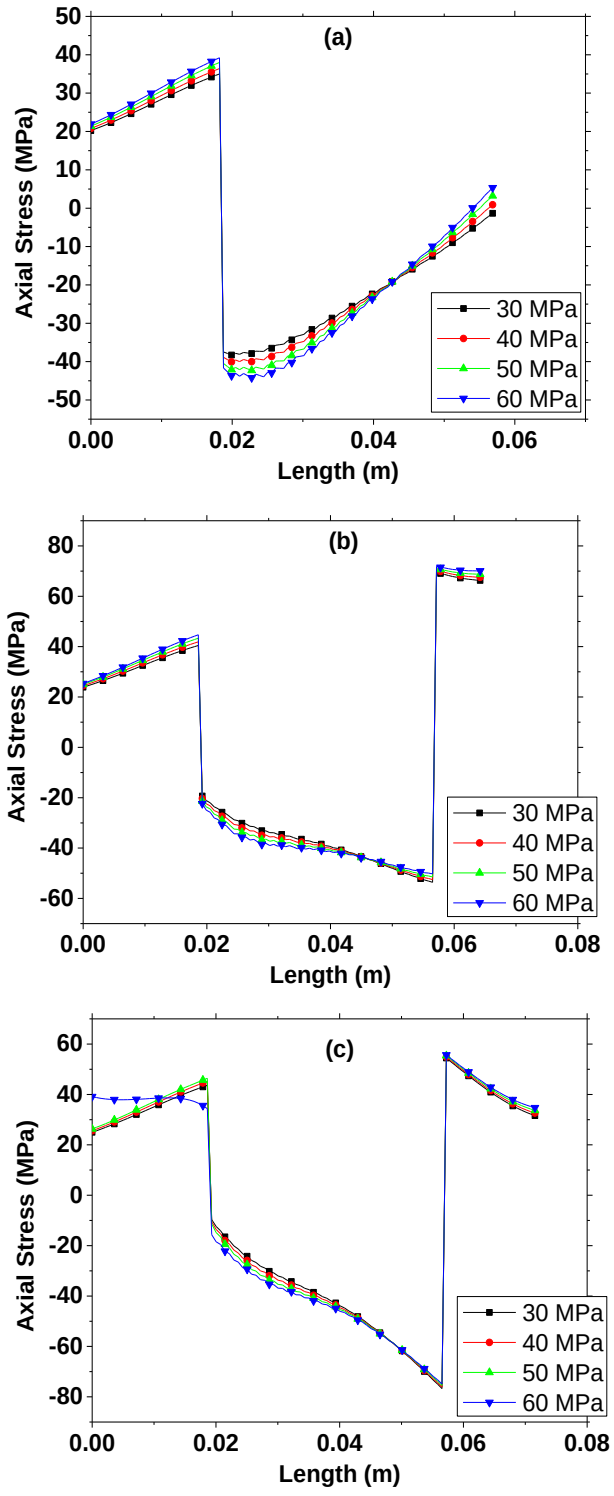

Figure 5.16 Axial stress of bobbin and coil 3 (& 4) along the median line from inner to outer radius. Three different cases are plotted: (a) without any banding, (b) with five layers of banding and (c) with ten layers of banding using the AA5083 wire of the same size.

5.6.3 Coil 5 & 6

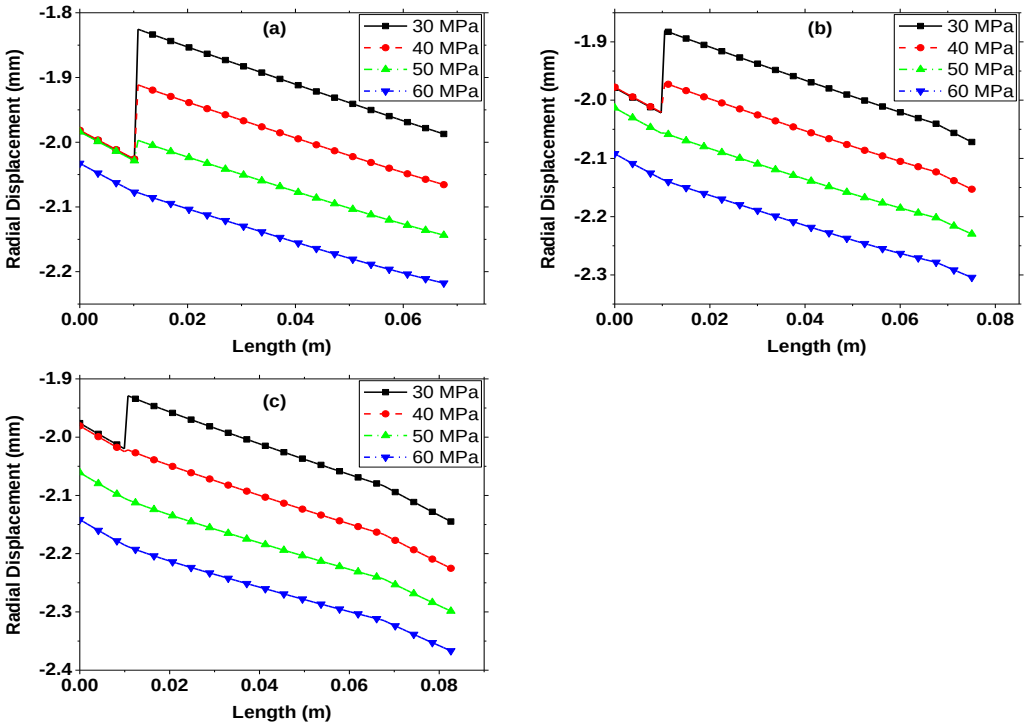

Figure 5.17 Radial displacement of bobbin and coil 5 (& 6) along the median line from the inner to the outer radius. Three different cases are plotted: (a) without any banding, (b) with five layers of banding and (c) with ten layers of banding using the AA5083 wire of the same size.

From Figure 5.17 can be seen that in coils 5 & 6, the gap becomes zero at 60 MPa winding tension without any banding or at 50 MPa with five layers of banding. In this case, winding at lower tension (50 MPa) with five layers of banding is chosen. Additionally, higher tension may be provided on the banding. Since the current carrying capacity of the superconducting wire can degrade at high stresses, it is always preferred to have a lower winding tension applied on the coil. It is especially true for coils with high fields, such as coil 5 & 6.

Figure 5.18, Figure 5.19 and Figure 5.20 show the radial stress, hoop stress and axial stress, respectively, in coil 3 & 4.

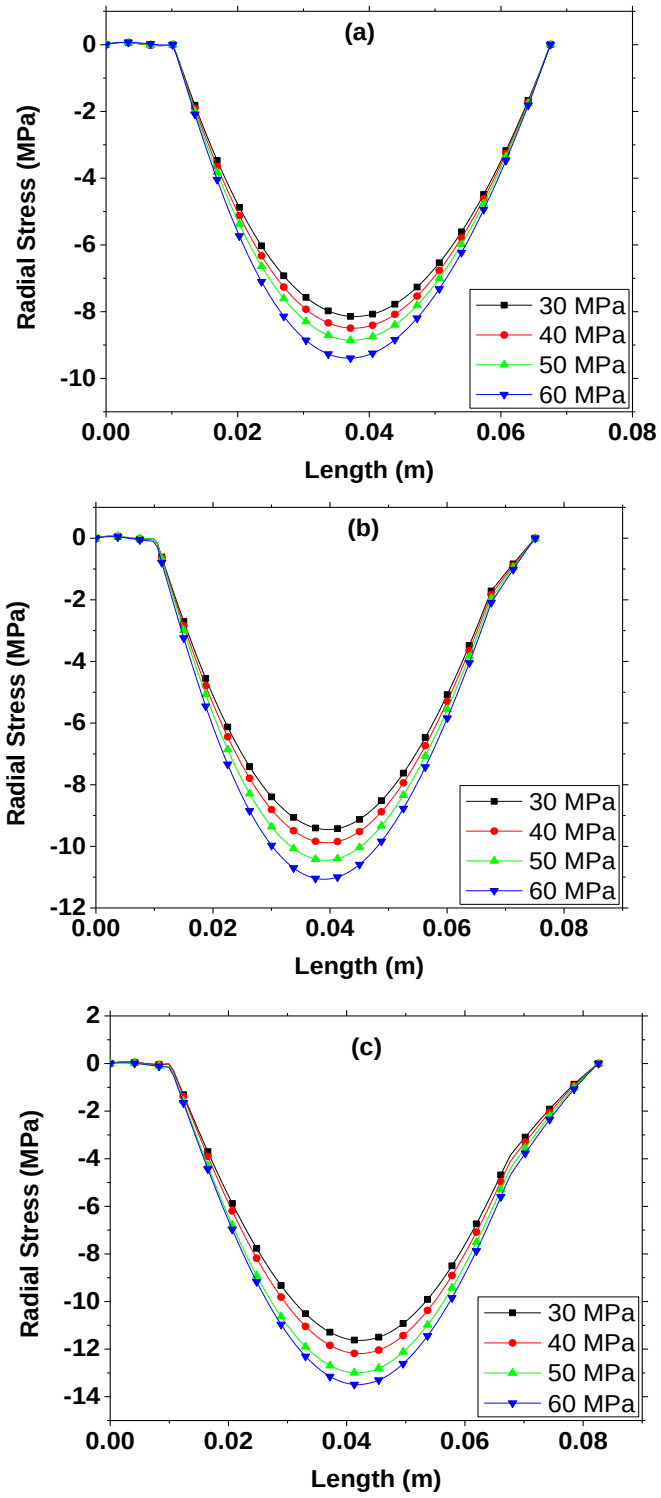

Figure 5.18 Radial stress of bobbin and coil 5 (& 6) along the median line from inner to outer radius. Three different cases are plotted: (a) without any banding, (b) with five layers of banding using the same superconducting wire and (c) with ten layers of banding using the AA5083 wire of the same size.

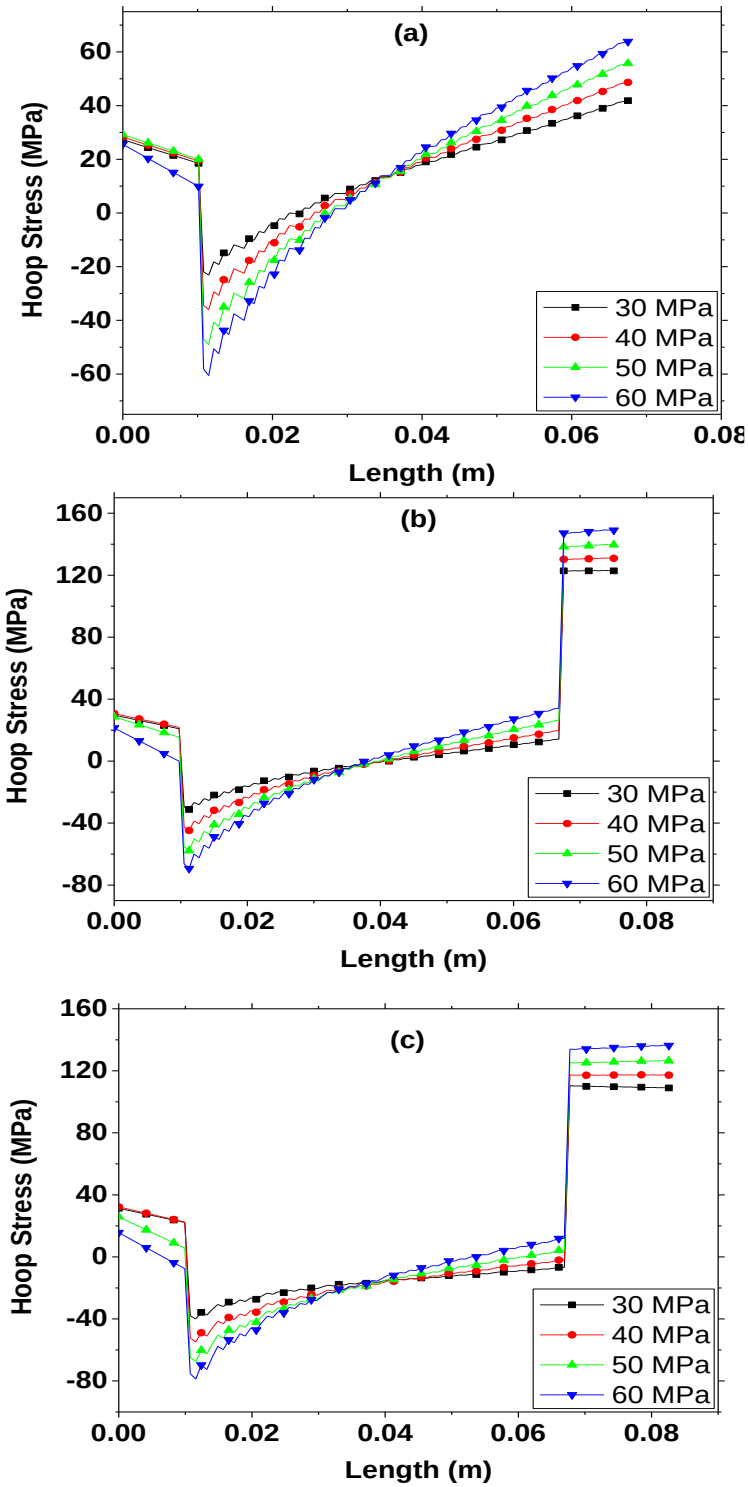

Figure 5.19 Hoop stress of bobbin and coil 5 (& 6) along the median line from inner to outer radius. Three different cases are plotted: (a) without any banding, (b) with five layers of banding using the same superconducting wire and (c) with ten layers of banding using the AA5083 wire of the same size.

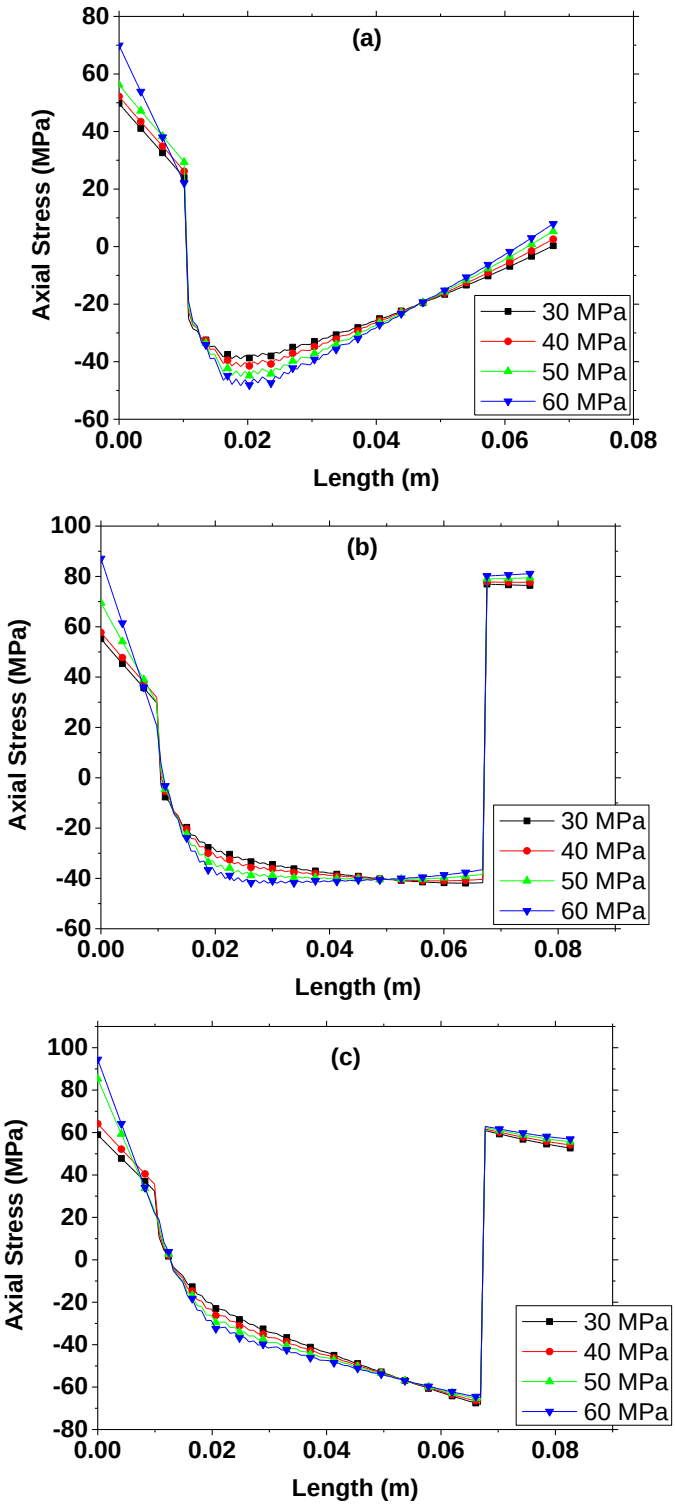

Figure 5.20 Axial stress of bobbin and coil 5 (& 6) along the median line from inner to outer radius. Three different cases are plotted: (a) without any banding, (b) with five layers of banding using the same superconducting wire and (c) with ten layers of banding using the AA5083 wire of the same size.

5.6.4 Coil 7 & 8

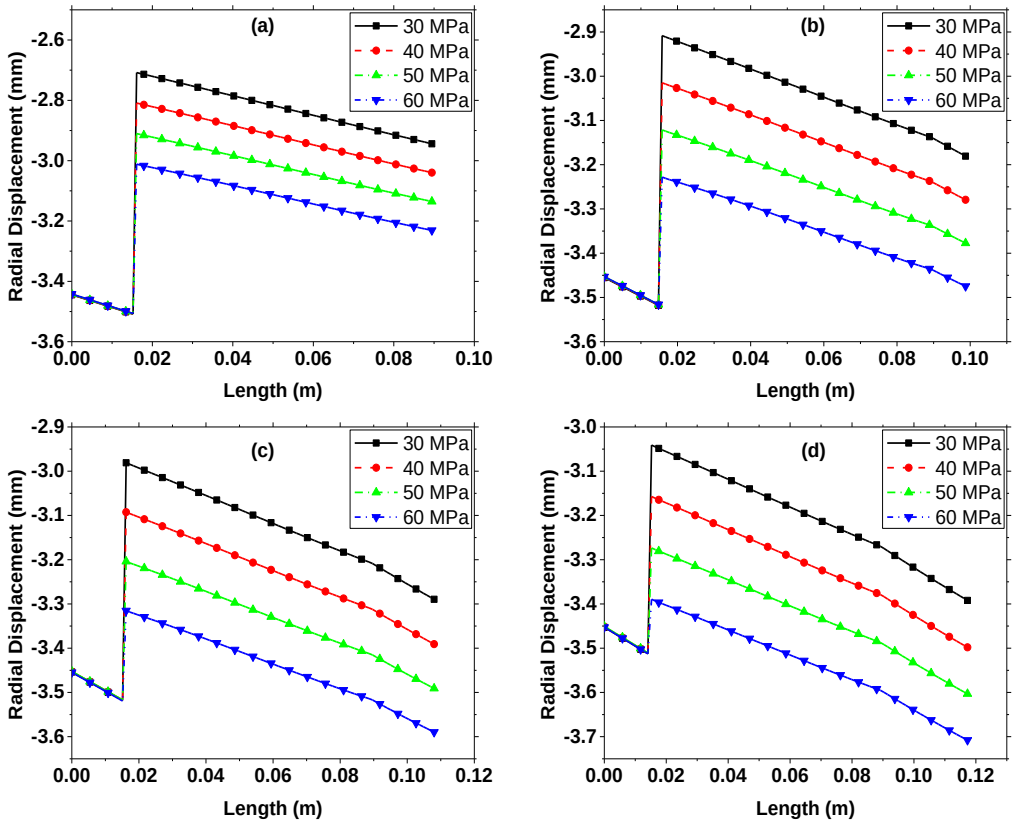

Figure 5.21 Radial displacement of bobbin and coil 7 (& 8) along the median line from inner to outer radius. Four different cases are plotted: (a) without any banding, (b) with five layers of banding, (c) with ten layers of banding and (d) with 15 layers of banding using the AA5083 wire of the same size.

In the case of coils 7 & 8, even at high tensions and 15 layers of banding, the gap doesn't become zero, which is evident from Figure 5.21. In such a case a high number of over binding (15) wound at very high tension can be considered. It may be noted that wire used in C7/C8 has a lower strength and thus, a lower tension is applied on it during winding. Figure 5.22, Figure 5.23 and Figure 5.24 show the radial stress, hoop stress and axial stress, respectively, in coil 7 & 8.

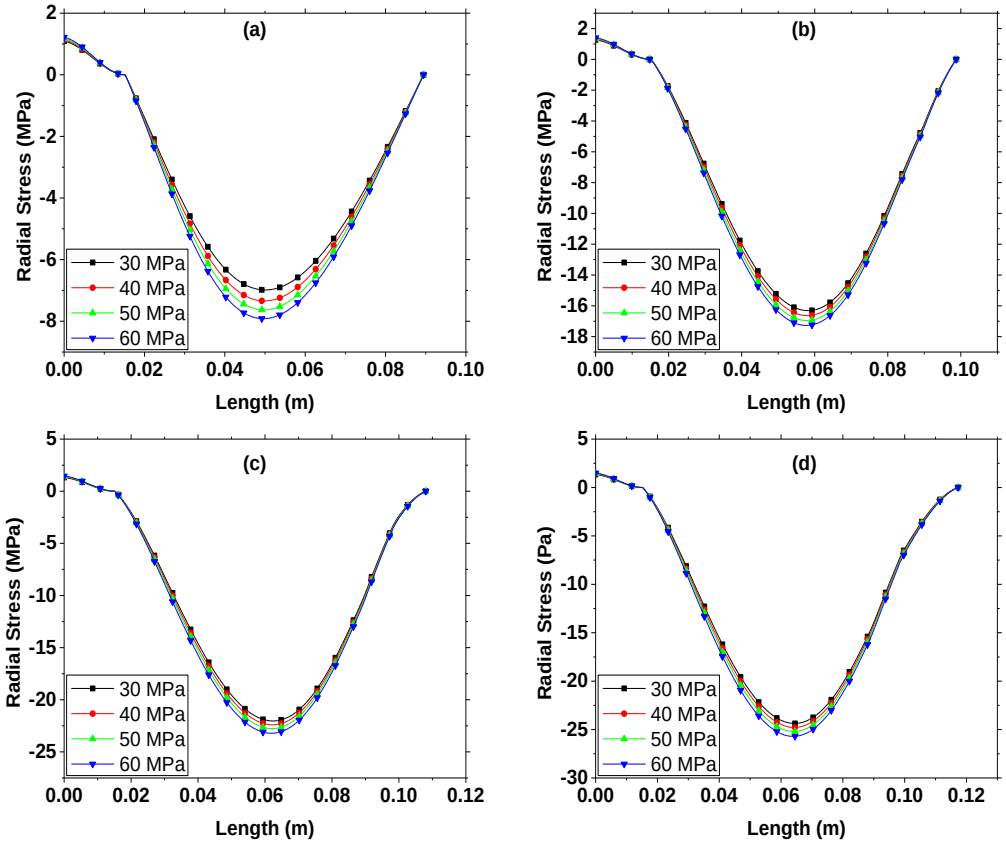

Figure 5.22 Radial stress of bobbin and coil 7 (& 8) along the median line from inner to outer radius. Four different cases are plotted: (a) without any banding, (b) with five layers of banding, (c) with ten layers of banding and (d) with 15 layers of banding using the AA5083 wire of the same size.

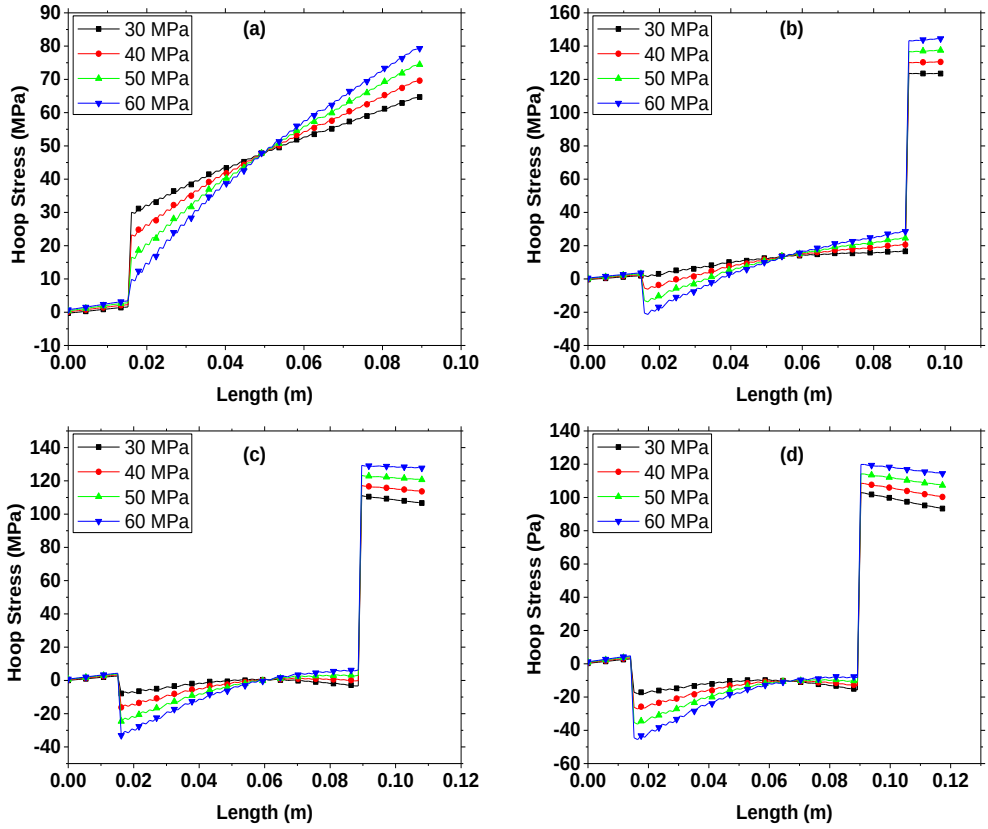

Figure 5.23 Hoop stress of bobbin and coil 7 (& 8) along the median line from inner to outer radius. Four different cases are plotted: (a) without any banding, (b) with five layers of banding, (c) with ten layers of banding and (d) with 15 layers of banding using the AA5083 wire of the same size.

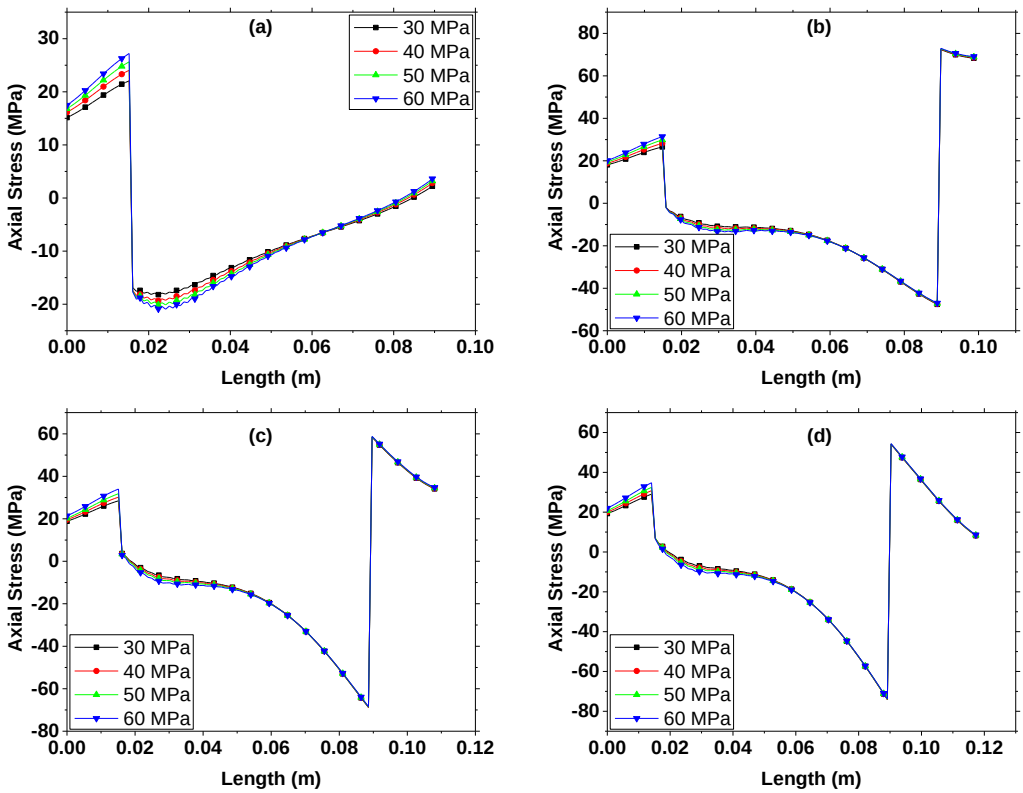

Figure 5.24 Axial stress of bobbin and coil 7 (& 8) along the median line from inner to outer radius. Four different cases are plotted: (a) without any banding, (b) with five layers of banding, (c) with ten layers of banding and (d) with 15 layers of banding using the AA5083 wire of the same size.

Based on the simulations, the final design of winding tension was done as per the following condition:

- Calculate the 'lift off' point for each turn. This is the point where the turn has zero radial stress.
- Check the final coil expansion does not leave a gap between the first layer and the former of more than 0.5mm to avoid dropped turns. The radial stress at this point should be low compared to a full contact between the coil and bobbin.

The final implemented design is given in Table 5.1. Due to symmetric nature, the coil pairs would have similar designed parameters.

Table 5.1 Final design of the magnet based on winding tension of the coil, over binding and the its winding tension.

Coil	Winding Tension (MPa)	Banding layers	Banding tension (MPa)
C1/C2	60	10	60
C3/C4	50	10	60
C5/C6	50	5	30
C7/C8	40	15	80

The details of radial displacement (Figure 5.25), radial stress (Figure 5.26), hoop stress (Figure 5.27) and axial stress (Figure 5.28) for the final design are given below. Figure 5.29 shows the final operational stress in the magnet structure.

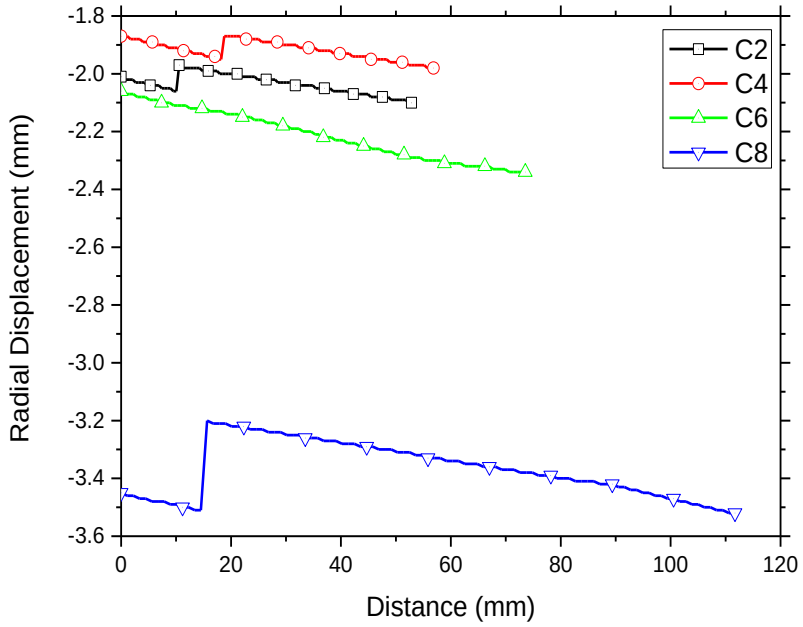

Figure 5.25 Radial displacement of bobbin and coils along the median line from inner to outer radius. The thickness of each coil is different, and it then further varies based on the layers of over binding put over it.

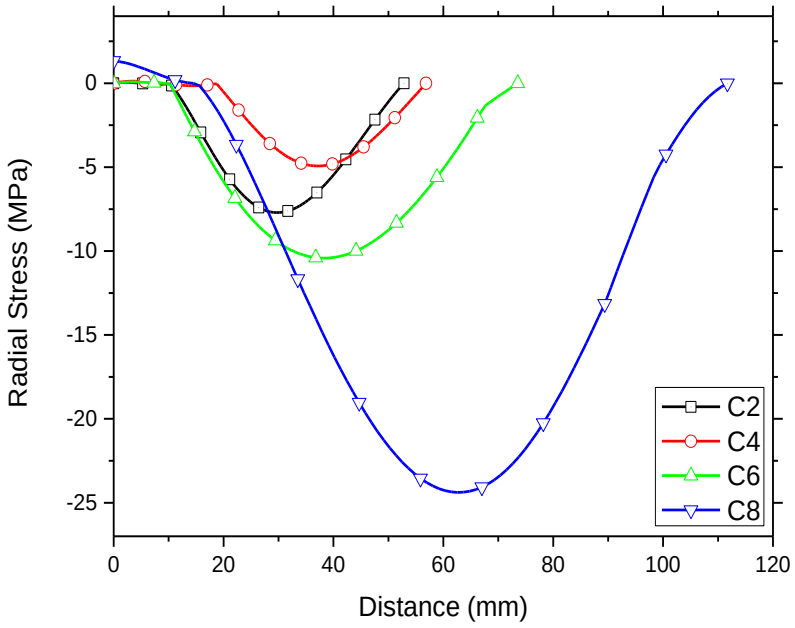

Figure 5.26 Radial stress of bobbin and coils along the median line from inner to outer radius. The thickness of each coil is different, and it then further varies based on the layers of over binding put over it.

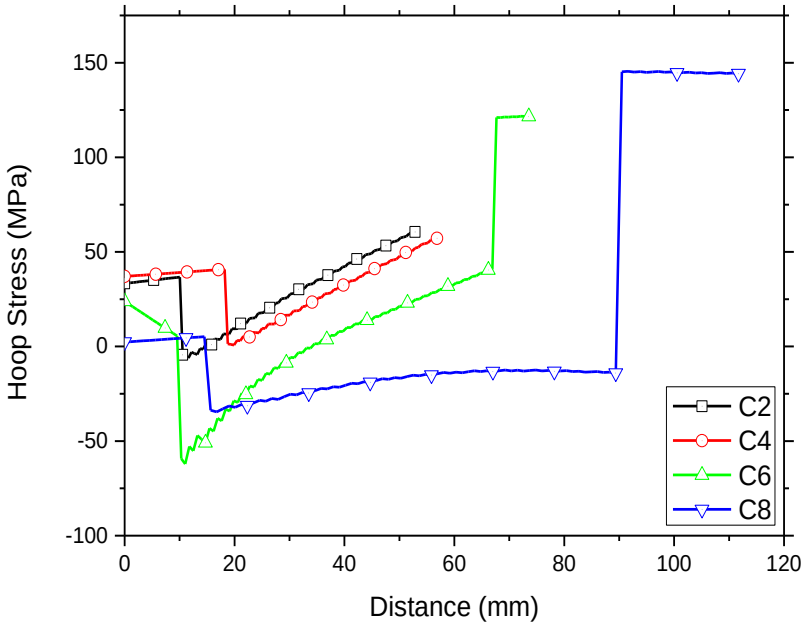

Figure 5.27 Hoop stress of bobbin and coils along the median line from inner to the outer radius. The thickness of each coil is different, and it then further varies based on the layers of over binding put over it.

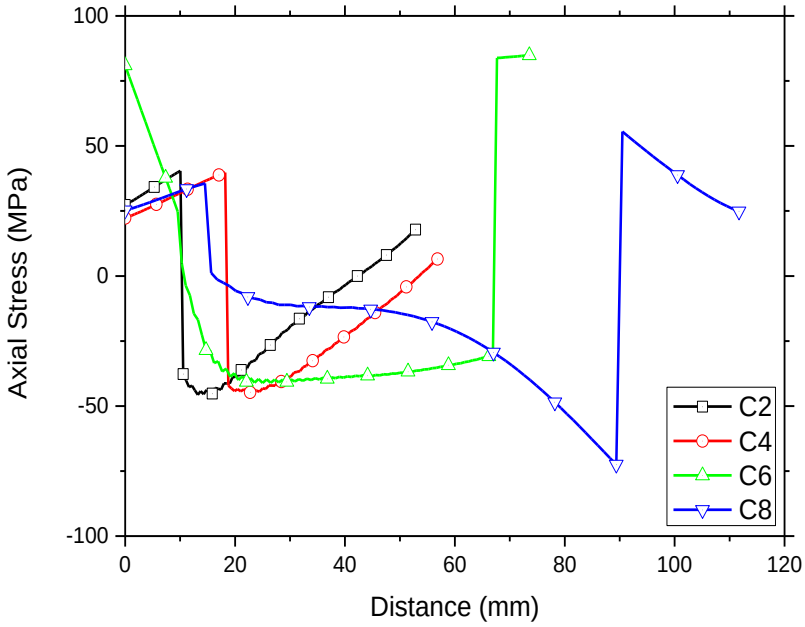

Figure 5.28 Axial stress of bobbin and coils along the median line from inner to outer radius. The thickness of each coil is different, and it then further varies based on the layers of over binding put over it.

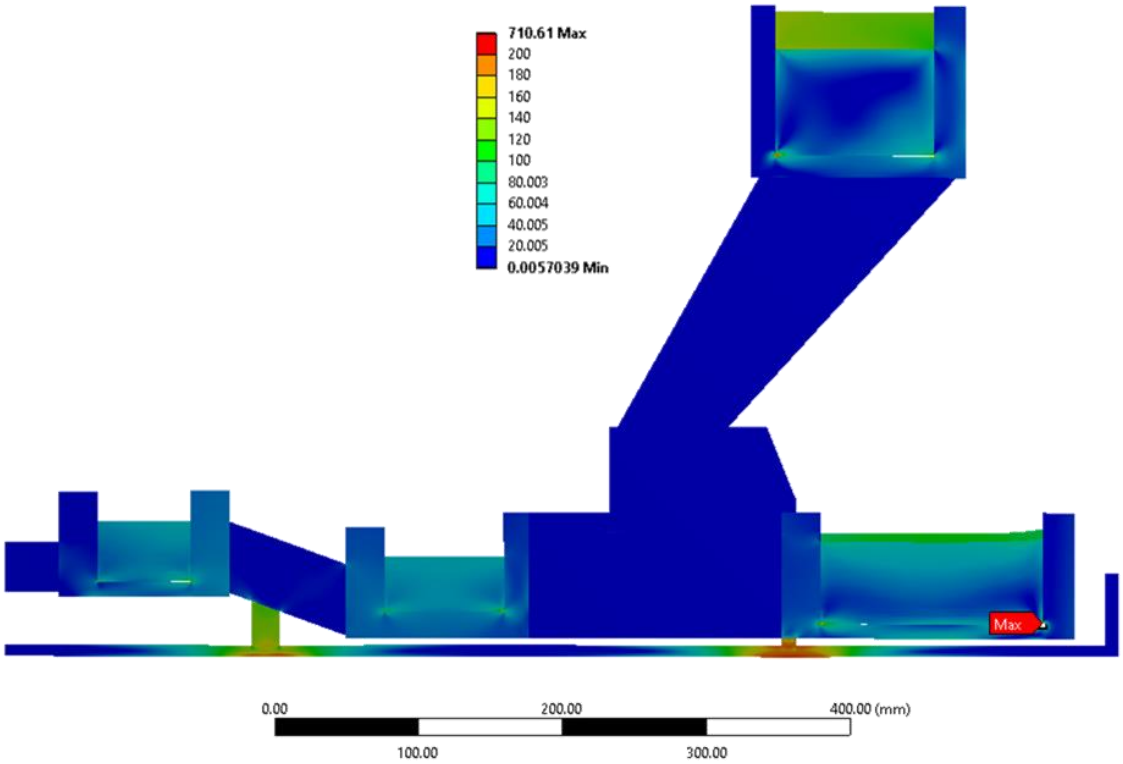

Figure 5.29 The final operational stress (MPa) in the magnet structure based on the selected winding tensions, thermal cooldown, and Lorentz forces.

5.7 Effect of Operational Stress

Based on the final operational model, the electromagnetic design of the magnet is reconsidered. The displacement of the bobbin and coils will cause relative movement in the magnetic coordinates of the system and this will affect the final magnet design. The thermal contraction of the bobbin and magnet structure also changes the coil cross-section. Since the magnet operates at a fixed current, the reduction in cross-sectional area increases the current density in each coil, which in turn increases the magnetic field.

One can assess adverse effects of thermal contraction by comparing the central magnetic field and the field homogeneity in the FOV before and after the thermal contraction. The simulation of the original magnetic coordinates and the disturbed coordinates show that the central magnetic field increases from 1.499964 T to 1.505933 T. The plot of magnetic field along the axis is shown in Figure 5.30. The increase in magnetic field shifts the resonance frequency of the MRI scanner to 64.11

MHz from 63.85 MHz. This variation is to be accounted for when designing the RF electronics associated with the imaging.

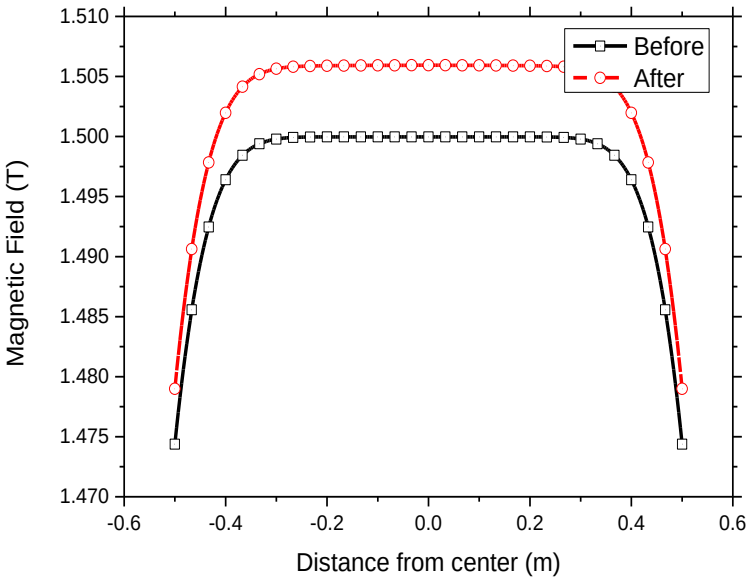

Figure 5.30 The variation in magnetic field along the central axis from the designed value to the final value achieved after the effects of operational stress is considered.

Considering the variation of magnetic field within the FOV, the field homogeneity can be plotted in a 45 cm DSV. Comparing the initial designed homogeneity to the final, it can be seen that the field homogeneity changed from ±5.5 ppm to ±278 ppm due to the variations in relative coil positions. The homogeneity plot is shown in Figure 5.31.

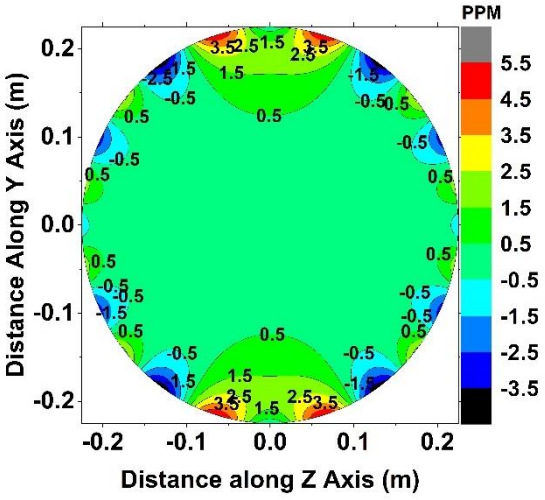

(a)

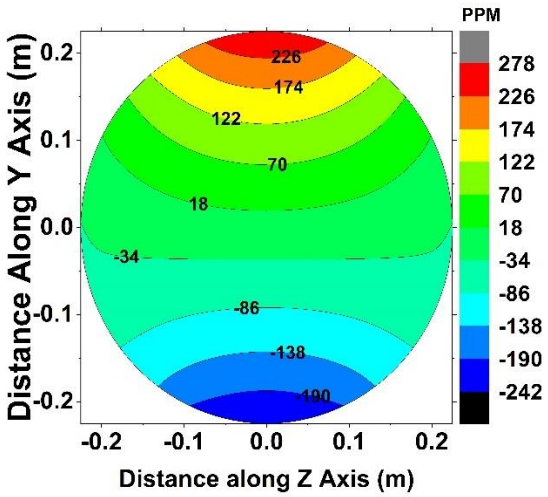

(b)

Figure 5.31 (a) The design field homogeneity (ppm) and (b) the achieved field homogeneity (ppm) in the 45 cm FOV at the iso-centre of the magnet. The homogeneity changed from ±5.5 ppm to ±277 ppm due to relative movement of coils.

The change is homogeneity can also be compared in terms of coefficients of Legendre polynomials. The coefficients A_n^m and B_n^m can define the magnetic field at any charge free location inside the magnet.

$$B_z = \sum_{n=0}^{\infty} \sum_{m=0}^{n} P_n^m \cos\theta \, (A_n^m \cos m\emptyset + B_n^m \sin m\emptyset) \tag{5.2}$$

where *A* and *B* are Legendre coefficients, P_n is Legendre polynomial of the n-th order [33], [117]. The zeroth order term is the central field and higher order terms are the harmonics which signify inhomogeneity of the magnetic field. It may be noted that for coil pairs symmetric about a plane, odd order terms are zero ($A_n^0 = 0$ and $B_n^0 = 0$, when n is odd) [118]. The cooldown of the magnet and the resultant relative displacements have introduced new harmonic terms, mostly in 2nd and 3rd order, which were not present before. Table 5.2 shows the coefficients of Legendre polynomials up to 16th order in the original design and the affected design due to operational stresses. During scanning or operation of the MRI magnet, the higher order harmonics can be of less effect in most of the cases. They only come into picture during precise modes, such as brain scans. However, the introduction of lower order terms is usually

problematic and can easily affect the filed quality and thus the image. The magnet thus needs to be shimmed to the design specifications before it can be used for scanning.

Table 5.2 The Legendre coefficients of the axial field in the FOV in the original design and the affected design due to operational stresses. New terms were introduced to the series due to distortions produced by the forces.

Order		**Original Design**		**Due to operational stresses**	
n	m	A_n^m	B_n^m	A_n^m	B_n^m
0	**0**	1.499964	0	1.505933	0
1	**1**	2.01×10^{-16}	1.11×10^{-16}	1.25×10^{-16}	3.15×10^{-04}
2	**0**	9.99×10^{-07}	0	-4.90×10^{-05}	0
2	**2**	-2.08×10^{-17}	-1.69×10^{-16}	-3.06×10^{-08}	-1.56×10^{-16}
3	**1**	-3.64×10^{-17}	8.81×10^{-18}	1.30×10^{-16}	-4.70×10^{-05}
4	**0**	3.73×10^{-06}	0	6.70×10^{-06}	0
5	**1**	-2.26×10^{-17}	-1.27×10^{-17}	7.89×10^{-17}	3.34×10^{-06}
6	**0**	3.16×10^{-06}	0	-3.03×10^{-06}	0
7	**1**	2.36x -17	-1.18×10^{-17}	4.68×10^{-17}	1.00×10^{-07}
8	**0**	4.43×10^{-06}	0	5.72×10^{-06}	0
9	**0**	-1.34×10^{-15}	0	-1.70×10^{-15}	0
9	**1**	1.41×10^{-17}	1.93×10^{-17}	3.88×10^{-17}	-1.20×10^{-07}
10	**0**	-5.59×10^{-06}	0	-6.24×10^{-06}	0
12	**0**	-1.19×10^{-05}	0	-1.22×10^{-05}	0
14	**0**	5.83×10^{-06}	0	6.09×10^{-06}	0
16	**0**	-1.41×10^{-06}	0	-1.49×10^{-06}	0

5.8 Coil Sensitivity Analysis

Further to operational stress and its effects, the manufacturing of the magnet also introduces variations to the intended magnetic field. These can be caused by a linear variation during machining of the winding surfaces of the bobbin or an angular variation to the coil during winding. While some corrections to the final magnetic field quality is possible by introducing small pieces of iron in the bore of the magnet, called passive shimming, the process has its limitations on how much iron can be placed at the central bore. This limitation comes both from a weight aspect and also because of the eddy current heating of the shim plates during the scanning. The standard practice for a 1.5T MRI magnet would be to shim up to 1000 ppm of inhomogeneity during the passive shimming phase.

In order to estimate the sensitivity of each coil towards the homogeneity, an analysis of the effect of various coil movements as defined in Table 5.3 were performed. The coils were moved individually or in pair by various distances and the effect in homogeneity was studied. The coil sensitivity based on these disturbances is shown in Figure 5.32. Considering a limit of 1000 ppm homogeneity, the manufacturing tolerances were fixed at 0.1 mm linear movement and 0.1° angular movement. The 1000 ppm limit is obtained as the limit up to witch a MRI can be shimmed using passive shimming techniques.

The results shows that any movement on coils 5, 6, 7, 8 have the largest impact on magnetic field homogeneity. Similarly angular movements have a much higher impact compared to linier movements. The movement of C5, C6, C7, C8 had large effects and the worst case was the angular movement of C5/C6 by 0.1° (815 ppm).

Table 5.3 Various linear and angular perturbations applied to various coils in order to simulate coil sensitivities.

Coil Case No	**1**	**2**	**3**	**4**	**5**	**6**	**7**	**8**
1	0	0	0	0	0	0	0	0
2	0.1	0.1	0	0	0	0	0	0
3	-0.1	-0.1	0	0	0	0	0	0
4	0.1	0	0	0	0	0	0	0
5	-0.1	0	0	0	0	0	0	0
6	0	0	0.1	0.1	0	0	0	0
7	0	0	-0.1	-0.1	0	0	0	0
8	0	0	0.1	0	0	0	0	0
9	0	0	-0.1	0	0	0	0	0
10	0	0	0	0	1	1	0	0
11	0	0	0	0	-1	-1	0	0
12	0	0	0	0	1	0	0	0
13	0	0	0	0	-1	0	0	0
14	0	0	0	0	0	0	1	1
15	0	0	0	0	0	0	-1	-1
16	0	0	0	0	0	0	1	0
17	0	0	0	0	0	0	-1	0
18	0	0	0	0	0.1°	0	0	0
19	0	0	0	0	0.1°	0.1°	0	0
20	0	0	0	0	-0.1°	0.1°	0	0
21	0	0	0	0	0	0	0.1°	0
22	0	0	0	0	0	0	0.1°	0.1°
23	0	0	0	0	0	0	-0.1°	0.1°

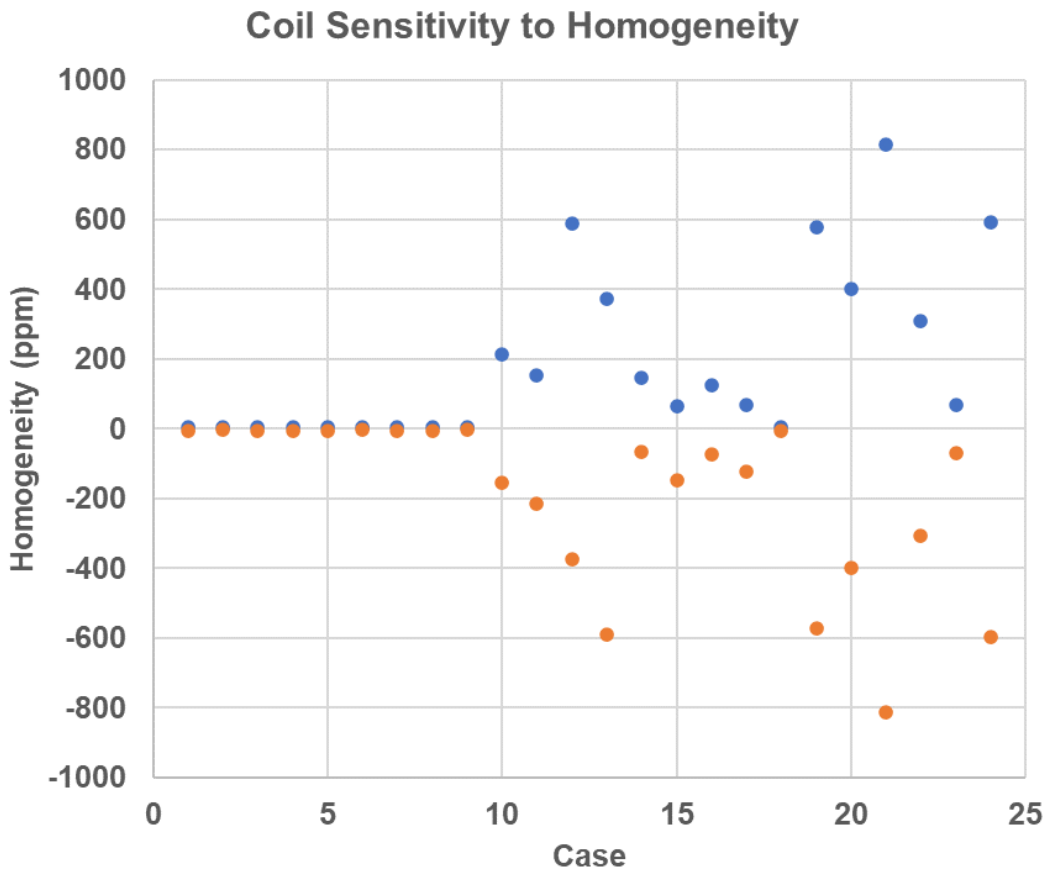

Figure 5.32 Coil sensitivity in terms of magnetic field homogeneity for various perturbations.

5.9 Magnet Test and Results

The final result of the design process would be to produce a magnet that operates to the defined specifications. This would include the cooldown of the magnet, ramping the magnet to required operating current, and critical component which is the field homogeneity that is achieved.

Based on the results of stress analysis the magnet was designed and fabricated at IUAC, New Delhi. The magnet was wound using around 80 km of Nb-Ti wire in channel superconducting wire, wound over an aluminium former (Figure 5.33). After fabrication, the magnet was housed in a 4.2K helium cryostat which had a patient bore of 90 cm. The magnet was cooled down to 4.2K using liquid helium and energized to 1.5 T (Figure 5.34).

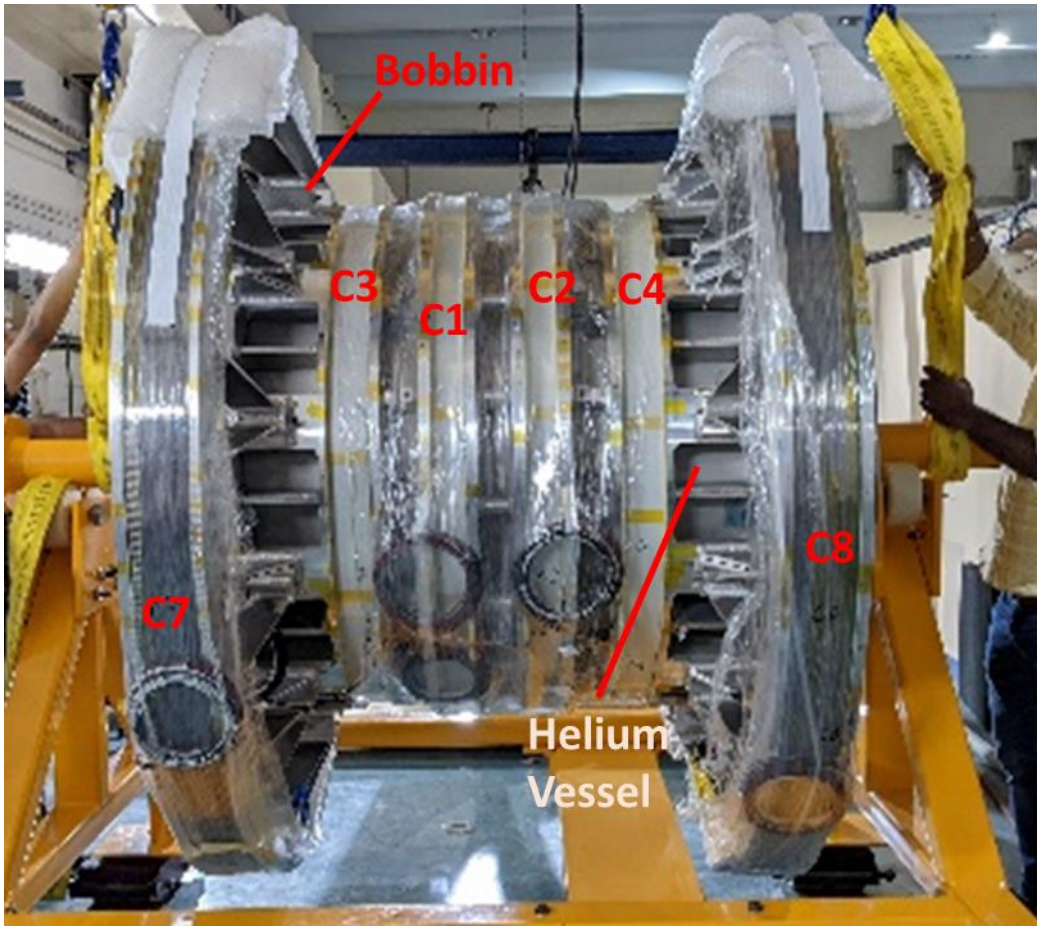

Figure 5.33 The finished magnet on a jig before assembly inside a helium vessel.

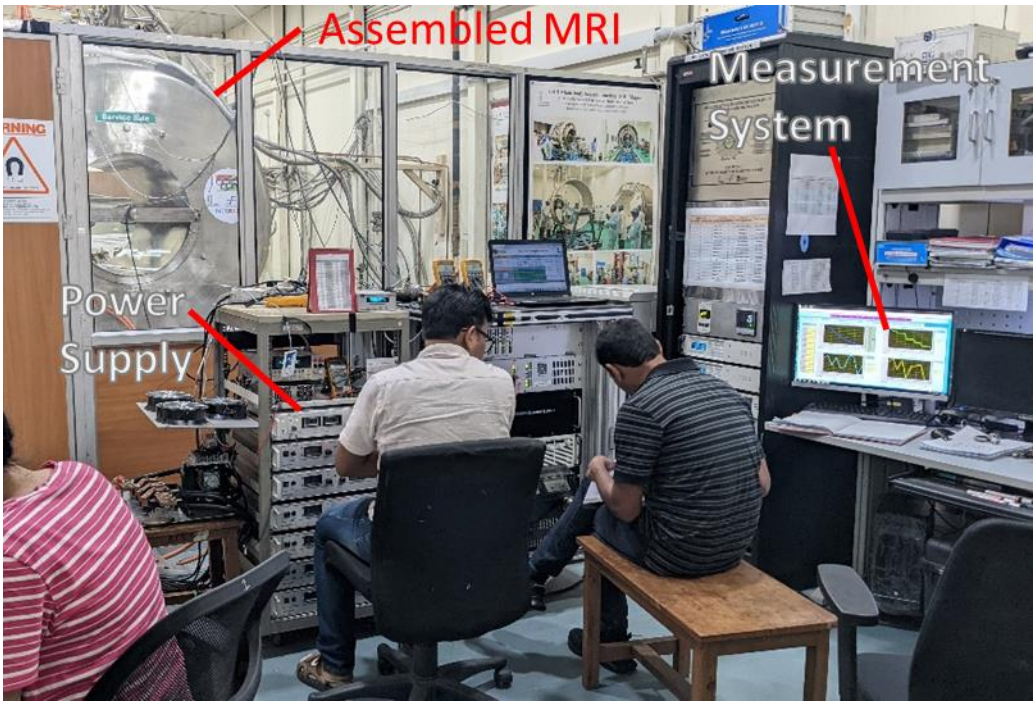

Figure 5.34 Finished and assembled MRI magnet in test bay during testing.

After cooldown and extensive testing, the homogeneity of the fabricated magnet was measured. The measurement was done using a 18-point halfmoon NMR camera by Metrolab (Figure 5.35). The field camera has a number of NMR probes placed in predefined positions in an halfmoon fixture. The core of an NMR probe is simply a coil wrapped around a sample. The sample is excited by scanning across a predefined range of wavelength and a Fourier transform of the output can provide the magnetic field value at the sample. The radiofrequency energy needed to cause spin flips in the sample is supplied by the coil wrapped around the sample. A separate receive coil close by captures the RF signal emitted by the sample.

Figure 5.35 The NMR half-moon camera with an overlap showing the PCB where 18 individual NMR probes are arranged to form a circle.

The 12-point halfmoon NMR camera offers a sophisticated means of spatially resolving the magnetic field distribution. By enabling the measurement of 18 distinct points in a plane, it facilitates detailed mapping of the field profile. This capability is particularly enhanced by the utilization of a specifically designed jig, as illustrated in Figure 5.36. Once centred the jig would allow the NMR probes to rotate covering a spherical surface at the centre of the magnet. Through controlled rotation within the magnet bore, the camera captures the field profile of a spherical volume, allowing for comprehensive characterization of the magnetic field's spatial distribution.

NMR probes utilize the resonance phenomenon to measure the overall strength of the magnetic field, represented by the resonant frequency of the sample. This resonant frequency is directly correlated with the magnetic field strength and is determined by the gyromagnetic ratio of the sample's nuclei, a fundamental physical constant. The stability of NMR magnetometers, characterized by minimal drift, obviates the need for frequent calibration, as the measurement relies on the inherent properties of the sample rather than external factors.

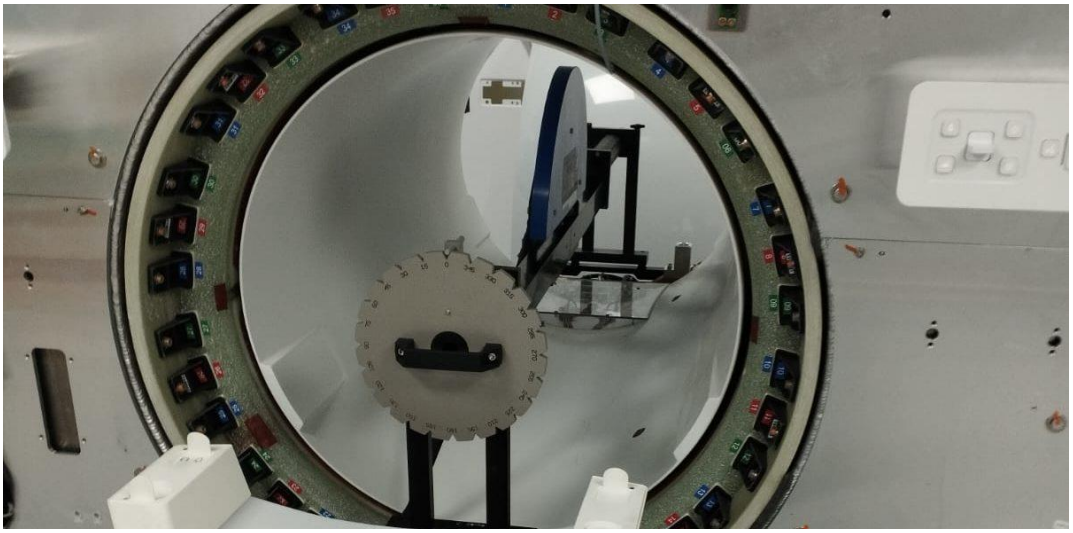

Figure 5.36 The NMR halfmoon camera inside the MRI magnet assembly.

In order to measure the homogeneity, the operating current is adjusted to attain a central field of 1.5 T. In this case this is achieved at 418A. This corresponds to a resonant frequency of 63.87 MHz at the centre. Then the NMR field camera is placed at the centre using a jig and measurements are taken for different angles by rotating the semi-circle, forming a sphere. Figure 5.37 shows the energized magnet produced a field homogeneity of ±307.5 ppm in the imaging volume against the predicted value of ±278 ppm.

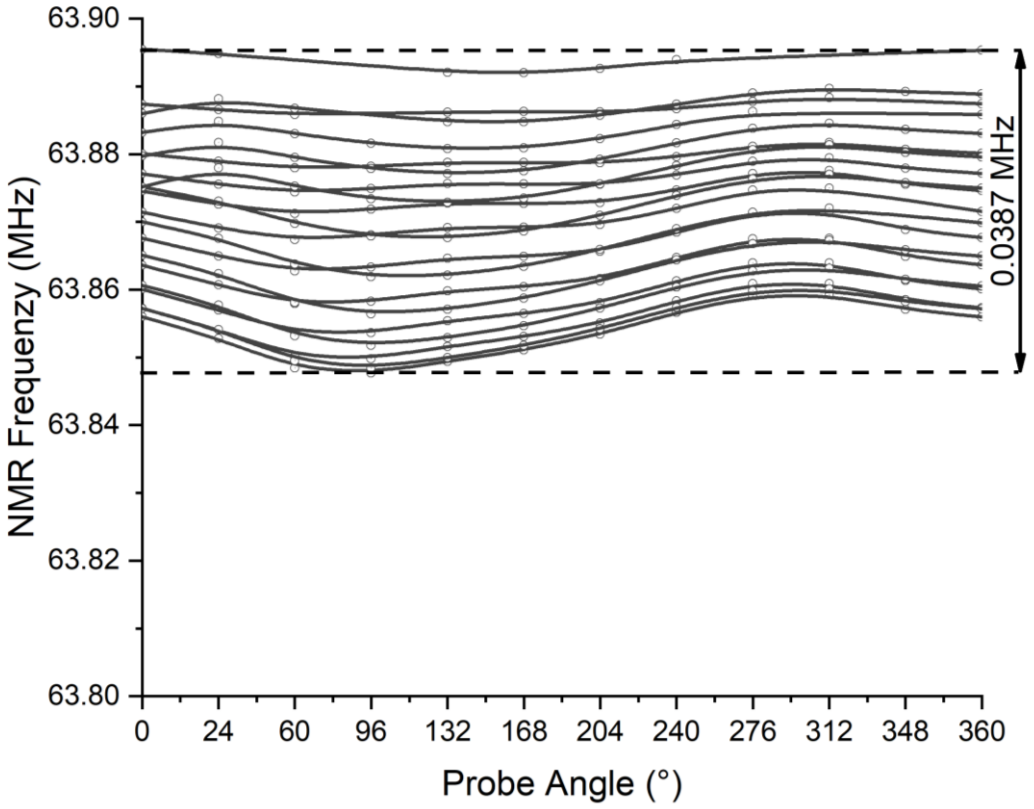

Figure 5.37 The plot of measured homogeneity in terms of change if frequency. Each line represents a single NMR probe and the x-axis are the different angles at which NMR probe measurement is made as it is rotated.

5.10 Conclusion

The operational stresses in the MRI magnet are studied and the winding stress is designed such that, the displacements and stresses are under acceptable limits. The final magnet is analysed and compared to the initial design. It was assessed that for the designed current, the central magnetic field varied from 1.499964 T to 1.505933 T. The magnetic field homogeneity changed from the designed value of ±5.5 ppm to ±278 ppm. These variations were also observed in the Legendre polynomial expansion of the magnetic field in the DSV. The sensitivity of coils to dimensional variation and manufacturing tolerance is also studied to estimate the applicable tolerances. Based on the results, the magnet design is finalized, manufactured and tested.

The tested magnet produced a field homogeneity of ±307.5 ppm in the imaging volume against the predicted value of ±278 ppm.

CHAPTER 6

BOND GRAPH MODEL FOR MODELLING EMERGENCY SHUTDOWN/QUENCH OF A SUPERCONDUCTING MAGNET

6.1 Introduction

Emergency shutdown of the magnet involves heating a portion of the magnet forcefully, such that the magnet starts to quench. Here a computational model to simulate the quench in a superconducting magnet using a bond graph is presented. While similar ideas have been proposed before, limited literature is available regarding this approach [65]–[67]. The use of bond graph can provide a simple model which is less resource-intensive. Here, two domains of magnet analysis, i.e. thermal and electrical, with two-way coupling, are considered.

6.2 Bond Graph Model of the Thermodynamic Domain

The thermodynamic domain of a superconducting magnet can be modelled using various approaches. While a true bond graph would be the most ideal solution, a pseudo bond graph will provide multiple advantages over the true bond graph model. In a pseudo bond graph, the flow variable (f) will be the heat flow (Q), and the effort variable (e) will be temperature (T).

In order to model the thermal domain, a lumped model is considered [119]. The solenoid coil is divided into small lumps in the axial and azimuthal directions, and each lump is modelled individually as a capsule using a pseudo bond graph [120], [121] with the capsule having external ports for modelling thermal conduction to neighbouring lumps. The geometry of the complete solenoid is shown in Figure 6.1. A single lump is highlighted in blue, where the quench is assumed to start.

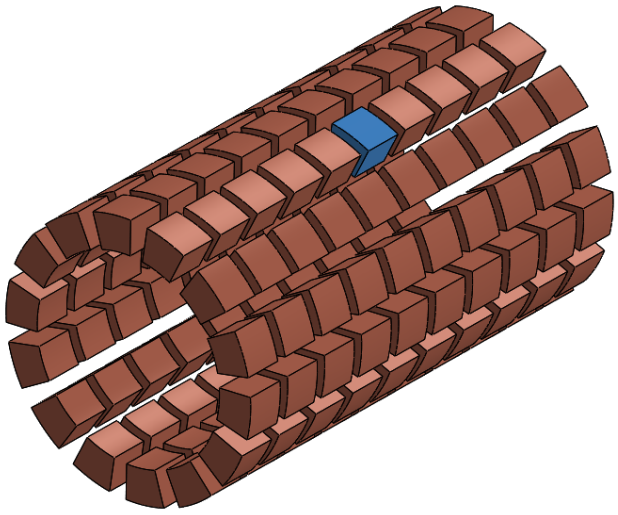

Figure 6.1 The complete solenoid geometry is divided into multiple lumps in axial and azimuthal directions. The quench initiates at the lump highlighted in blue.

Considering a small finite elemental volume within a superconducting magnet, the thermal domain of that volume can be modelled as follows. The energy stored in that volume will be $M.C_p.T$, where M is the mass of the body (kg), C_p is the specific heat capacity (J/kg.K), and T is the temperature of the body (K). This can be modelled in the bond graph as a C-element. The coefficient of the C element will be $K = 1/ (M. C_p)$, so the power variables can be related as Q= e/K. When generating the bond graph, the temperature of the lump can be measured using a detector (De)

element. The detector would be connected to the junction through an information bond rather than an energy bond.

Thus, the temperature of the lump (effort) can be calculated from the energy variable as T = Q*K. It may be noted that the Cp of a material is dependent on temperature, so that K = 1/($M.C_p(T)$). However, if that is considered in the bond graph, it will create a circular reference, since temperature T is calculated from C_p with a function of the same temperature. A similar problem of modulated C-element has been addressed by D Karnoop [12], [122], and it is concluded that ideally, a modulated C-element is not possible in the bond graph. So, here, the operating temperature range is considered and the average specific heat across that temperature range is considered.

The volume will generate heat in the form of Ohmic heating when the section is quenched. However, since the ohmic heating is dependent on the current and the resistance of the volume, this cannot be modelled as a static source of the flow. Here, the Ohmic heating is modelled using a modulated RS element that connects the thermal domain to the electrical domain. An RS element is an R element in the sense of bond graphs but with an additional source element showing entropy production. As with conventional R elements, power can leave through the thermal conduction bond or through the electrical bond. As long as more power enters the other bond, there is always some entropy produced (second law). Consequently, the RS element can either produce electrical power from an entropy flow over a finite temperature drop or pump entropy against a temperature difference by absorbing electrical power.

Each volume is connected to its neighbouring volumes, and heat will be transferred from each adjacent volume via conduction. In a thermal bond graph, the conduction can be modelled as an R-element connected to the path of heat flow through a 0-junction. Here, the material's thermal conductivity depends on the temperature of the material, so instead of a regular R-element, a modulated R-element is used, with the resistivity represented as a function of temperature. In order to provide better accuracy, contrary to some published literature [119], [123], [124], two R-elements are considered so that each R-element will provide half thermal resistance, with the resistivity defined by the temperature of two adjacent lumps. This can provide better accuracy where a large variation of resistivity due to a variation of temperature is present. The coefficient can be defined as $R= \rho\ L\ /\ A$ where ρ is the resistivity of copper, L is half the width of a lump, and A is the cross-sectional area of the lump with respect to the direction of heat flow. The pseudo causal bond graph for the thermal

model of a single lump of a solenoid magnet is shown in Figure 6.2. ①, ②, ③, ④, ⑤ are interface connections when this model is used as a sub model.

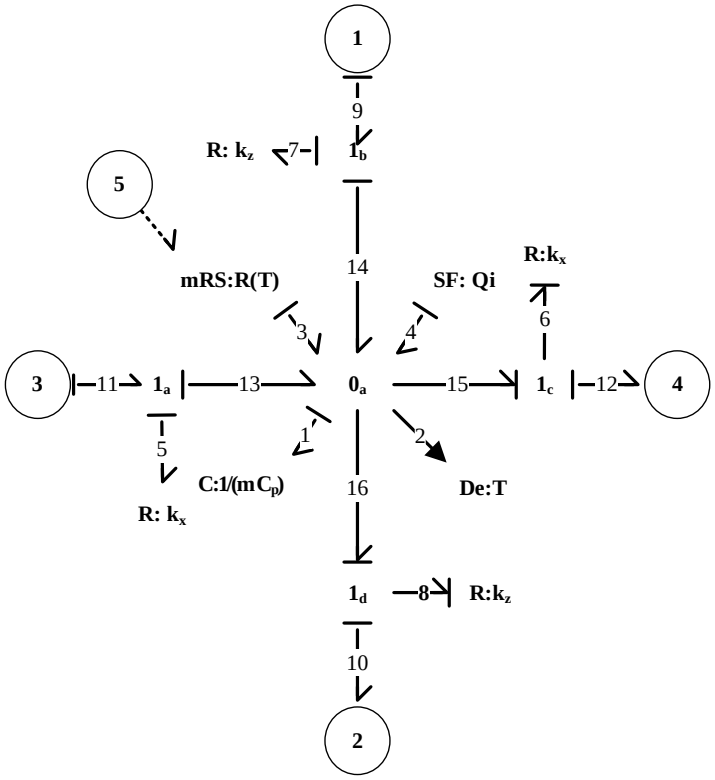

Figure 6.2 The pseudo causal bond graph for the thermal model of a solenoid magnet's single lump. The interface connections ①, ②, ③, ④, ⑤ are used when this model is employed as a sub model and connected to other lumps.

In practice, when using software such as Symbols Sonata, the RS element can be modelled as a modulated source of flow with the magnitude of flow equal to the heat generated (power) in the R-element in the electrical domain. Since the thermal domain is modelled as a pseudo bond graph and the electrical domain is modelled as a true bond graph, the power (w) generated as heat in the electrical domain is equivalent to the flow (f) in the pseudo-thermal bond graph.

Similarly, an effort-activated I element is also connected to the 0-junction to have a 'Detector' element. Since this element is activated, its constituent equations will not appear in the solution. However, an energy variable P is generated for the effort-activated I-element such that the differential of the variable $\dot{P}$ will give the

temperature of the lump. Figure 6.3(a) shows the pseudo causal bond graph for the thermal model of a single lump of a solenoid magnet and (b) indicates the model as represented by a capsule.

When a capsule is generated, the bond graph is not solved, however the constituent equations and the relevant variables are generated. While using the capsule the equations and variables are then reused reducing the size of the model. Moreover, variable can also be defined as global variables and they will be shared between different capsules, further reducing the size and complexity of the model. Global variables can be used for common parameters such as material properties, initialisation values etc.

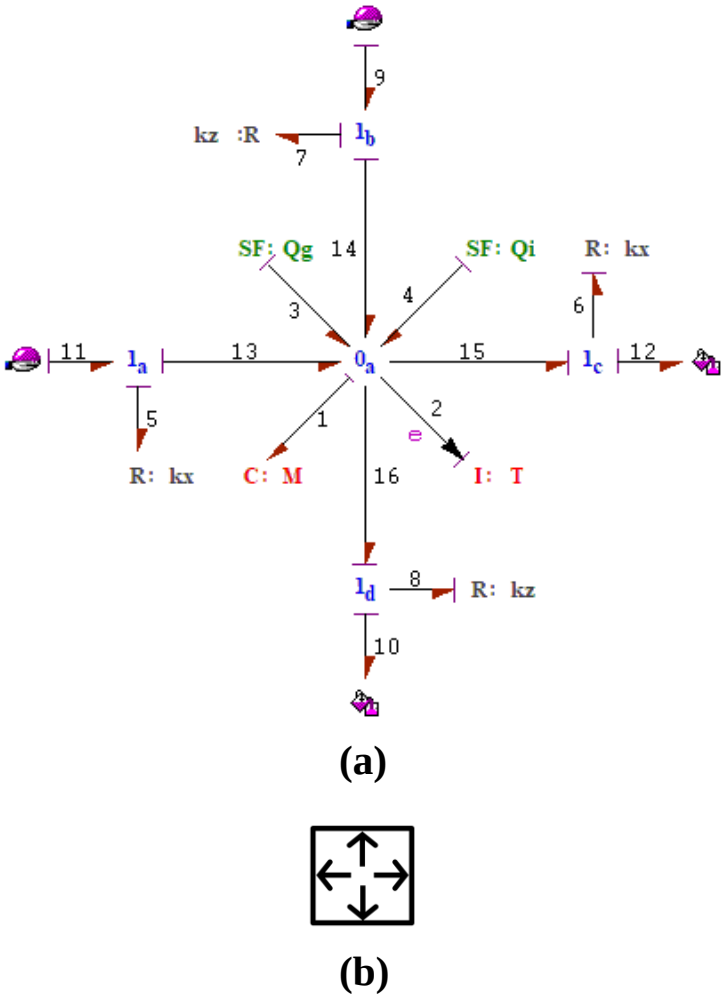

Figure 6.3 The thermal model of a single lump of a solenoid magnet represented as (a) a pseudo causal bond graph and (b) as represented by a capsule

The mathematical equations of the thermal model can be derived from the causaled bond graph. The constitutive equations of the 0-junctions are

$$Junction\ 0_a: \begin{cases} \dot{Q}_1 = f_3 + f_4 + f_9 + f_{11} \\ -f_6 - f_8 \\ \dot{P}_2 = e_1 = e_{13} = e_{14} \\ = e_{15} = e_{16} \end{cases} \tag{6.1}$$

The equations for the 1-junctions are

$$\text{Junction } 1_a: \begin{cases} e13 = e11 - e5 \\ f5 = f11 = f13 \end{cases} \tag{6.2}$$

$$\text{Junction } 1_b: \begin{cases} e14 = e9 - e7 \\ f7 = f9 = f14 \end{cases} \tag{6.3}$$

$$\text{Junction } 1_c: \begin{cases} e15 = e6 + e12 \\ f6 = f12 = f15 \end{cases} \tag{6.4}$$

$$\text{Junction } 1_d: \begin{cases} e16 = e8 + e10 \\ f8 = f10 = f16 \end{cases} \tag{6.5}$$

The bond graph elements can be explained in terms of their constitutive equations as follows.

$$\text{C}_1 \text{ Element: } e1 = K1 \int \dot{Q}\, dt = \frac{Q}{m\, Cp} \tag{6.6}$$

$$\text{R Element: } e_5 = f_{11} * R5 \tag{6.7}$$

$$\text{R Element: } e_7 = f_9 * R7 \tag{6.8}$$

The complete thermal bond graph of the magnet consists of multiple lumps connected together in a grid. In the case of azimuthal direction, the last row of capsules is connected back to the first row, forming a closed loop. In contrast, in the axial

direction, the capsules at both ends are only connected to three neighbouring capsules instead of four. The complete bond graph model of the thermal domain is shown below. The bond ⑤ from the RS element will be connected to the electrical domain when the complete bond graph is modelled. The Figure 6.4 below shows the pseudo causal bond graph for the thermal model of the complete solenoid magnet using the sub-model. The bond interface ⑤ is not connected here and will be connected to the electrical model.

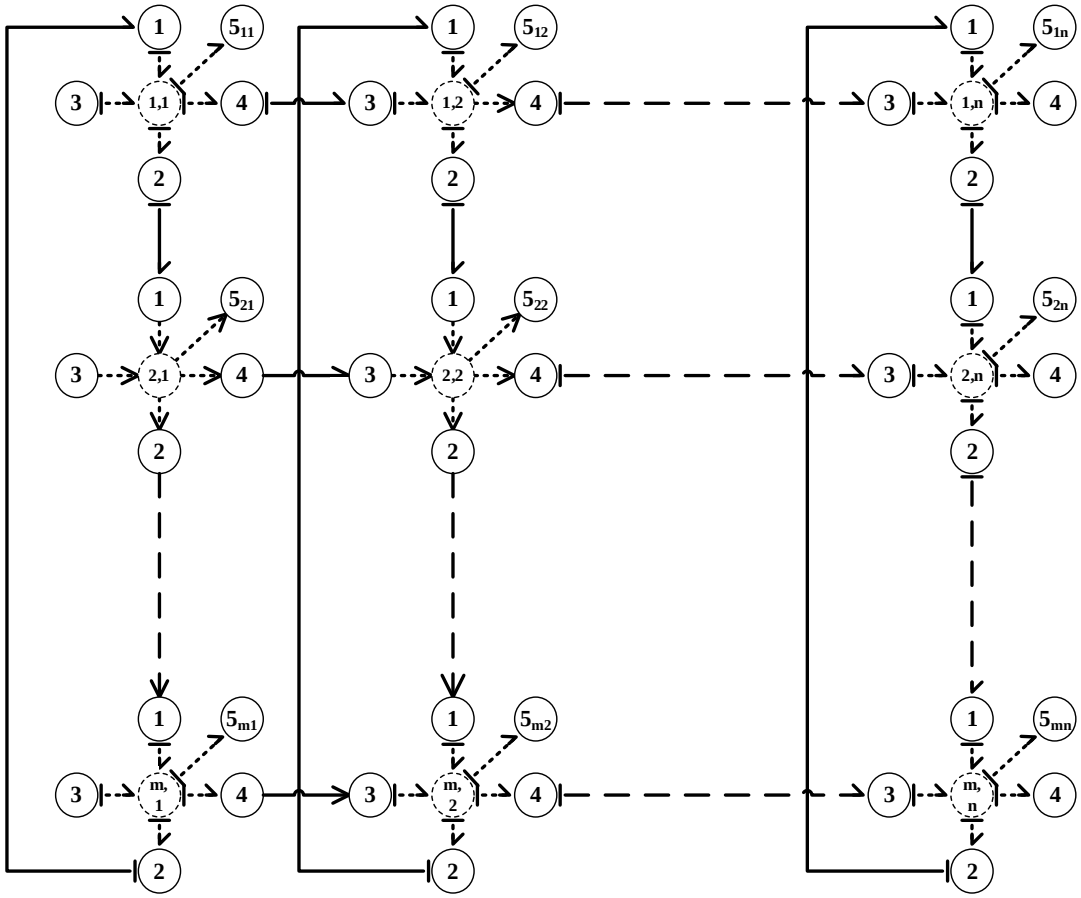

Figure 6.4 The complete thermal model of the solenoid magnet using the pseudo sub-model bond graph of individual lumps. The connection to the electrical model will be through the bond interface ⑤ which is left open in the thermal bond graph.

Once again, other features can be used to simplify the bond graph while using specific software. In Symbols Sonata, a bond graph, in this case, the thermal bond graph of a lump, can be modelled and saved as a capsule. Once a lump is defined with necessary elements, the element is stored as a capsule. It can be saved and reused multiple times. Since this bond graph is made as a capsule, it will not be solved in isolation [16]. Only the constitutive equations for elements and junctions are generated. When the capsule is reused, the same equations are also reused, thereby

reducing the computational cost. The final space state equations will be complex and will be calculated in the final model. In order to model the whole thermal domain, multiple interconnected capsules are used to form a mesh. The complete bond graph model of the thermal domain as modelled in Symbols Sonata is shown in Figure 6.5. Here, connectors represented as bullet points are used instead of curved bond lines. They are placed purely for aesthetic purposes and do not affect the model or final solution. The whole thermal model is then made into another capsule representing the thermal domain, which takes the electrical model's heat generation as input. The capsules output the temperature of each lump, which is used to determine the quenched volume (V_q), i.e. the part of the magnet that has turned normal from a superconducting state. This information will be used in the electrical model. The pseudo causal bond graph for the thermal model of the complete solenoid magnet and the model as a capsule is shown in Figure 6.5 (a) and Figure 6.5 (b) respectively

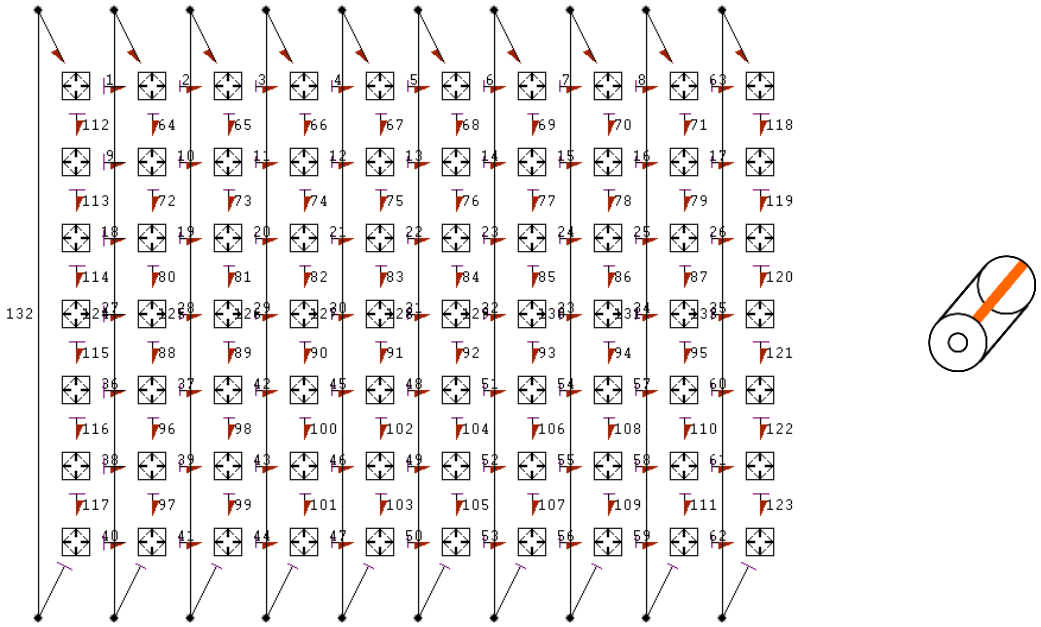

(a) **(b)**

Figure 6.5 The thermal model of the complete solenoid magnet as (a) a pseudo causaled bond graph and (b) the model represented as a capsule

The whole model can be used directly with an electrical bond graph, but in this case, it is further converted to a capsule. This capsule can then be reused to represent a individual solenoid coil in cases where multiple coils that are thermally disconnected but electrically connected, such as those in MRI magnets, are present. The symbol of the capsule is shown in Figure 6.5 (b).

6.3 Bond Graph Model of the Electromagnetic Domain

The electrical circuit consists of a single dump resistor (R_d) placed across the magnet, as shown in Figure 6.6 (a). Here, the magnet is represented by an ideal inductor and a modulated resistor. Since the operation is not at high frequencies, the reactance of the inductor may be ignored. The internal resistance of the magnet is the summation of the resistance of each lump, which may be represented as

$$R = \begin{cases} 0 : T \leq T_c \\ \rho_v(T) \times V_q \ : T > T_c \end{cases} \tag{6.9}$$

Here $\rho_v(T)$ is the temperature-dependent volume resistivity, V_q is the quenched volume, T is the temperature of the lump, and T_c is the critical temperature.

The bond graph for the circuit is shown in Figure 6.6 (b). The thermal model connects to the electrical model via the RS element and ⑤.

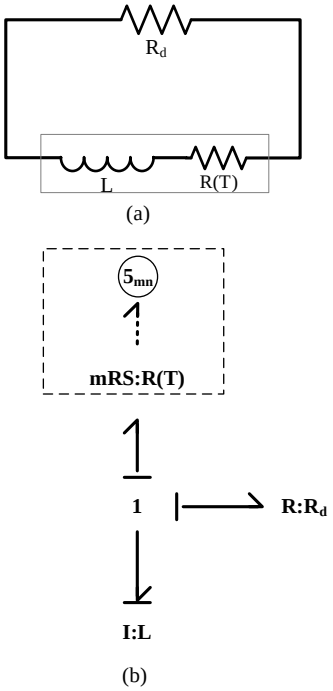

Figure 6.6 (a) The electrical diagram of the solenoid magnet including a with a dump resistor (R_d) placed across it for quench protection and (b) the circuit represented using an electrical bond graph. The thermal sub-model would connect to the electrical model through the interface ⑤ and the RS element.

Once the thermal model is designed, it is essentially applicable to any magnet design, with parameters such as magnet dimensions and material properties being different. The electrical bond graph can be changed accordingly depending on the electrical design. This design can vary from small solenoids to large multi-coil MRI magnets.

The mathematical equations of the electrical model can be derived from the causal bond graph. The constitutive equations of the 1-Junction is:

$$Junction\ 1: \begin{cases} f_1 = f_2 = f_3 = P_2/M_2 \\ \dot{P}_2 = R_1.f_2 - R_3.f_2 \end{cases} \tag{6.10}$$

The space state equation is

$$\dot{P}_2 = \left(\frac{R_1}{M_2} - \frac{R_3}{M_2}\right) P_2 \tag{6.11}$$

When implementing the model through Symbols Sonata, the RS element is represented as a modulated resistor with separate effort and flow detectors are placed to detect the power ($w_1 = e_1.f_1$). In the case of a resistor in the electrical domain, this power will be the heat generated (i^2R). which is passed on to the thermal model as a flow input. The bond graph of the electrical domain as modelled in Symbols Sonata is shown below. The thermal model of the whole magnet is represented as a capsule, with information bonds connecting the capsule and the electrical bond graph. Combined electrical and thermal bond graph of a solenoid superconducting magnet as modelled in Symbols Sonata is given in Figure 6.7.

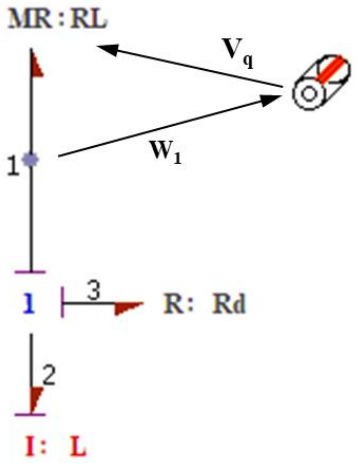

Figure 6.7 The complete physics of the quench of superconducting solenoid magnet as modelled in Symbols Sonata. The model consists of both thermal bond graph, represent as a capsule and electrical bond graph.

6.4 Validation of Bond Graph Model

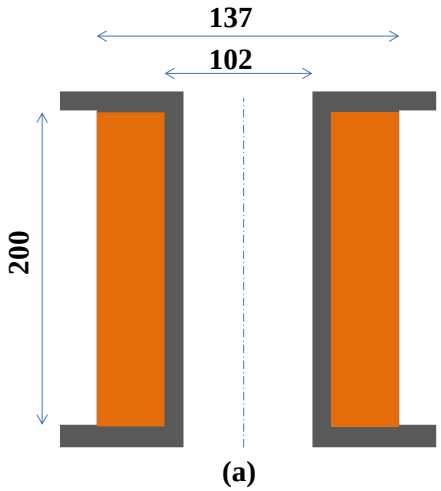

(a)

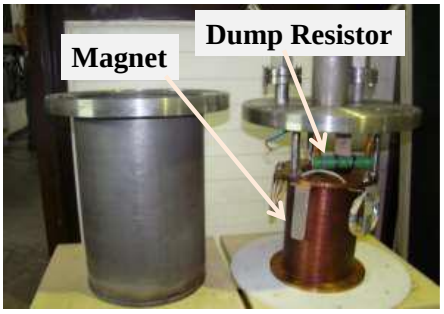

(b)

Figure 6.8 (a) The critical dimensions of the 6 T superconducting solenoid magnet and (b) photograph of the fabricated magnet including its protection circuit.

In order to validate the quench model, the simulation results are compared to the experiment results of the 6 T solenoid magnet operating at 102A current [125]. The schematic and the photograph of the magnet are shown in Figure 6.8. For quench protection of the magnet, a dump resistor placed parallel to the magnet is used, extracting some of the magnet's energy outside. The magnet is conduction-cooled, and the worst-case scenario during operation is considered where the magnet is adiabatic. The details of the magnet are given in Table 6.1

Table 6.1 The major parameters of a superconducting solenoid magnet for a conduction cooled system.

Description	**Value**
Central axial field (B_0)	6T
Operating current	102 A
Inner diameter	104 mm
Outer diameter	137 mm
Winding length	200 mm
Material	OHFC Copper
Mass	11 kg
Inductance	5.5 H
Stored energy	28 kJ
Critical temperature	9 K
Quench initiation temperature	10 K

The magnet studied here is a 6 T solenoid magnet operating at 102 A current. The magnet is placed adiabatically in a vacuum environment and is conduction-cooled below the critical temperature (9K) using a 4.2K cryocooler. The magnet has an inductance of 5.5H. The magnet is wound using a Nb-Ti superconductor

embedded in a copper matrix. The Cu:SC ratio of the wire is 2:1. To validate the bond graph model, the quench of the 6T solenoid is compared against the experimental data. Here, a Cernox® sensor is embedded in the coil, and it can provide the temperature of that coil at that point during quench. It may be noted that, in this case, the quench can initiate at any point in the magnet, and the sensor will not be monitoring the peak temperature.

As a case study, the value of the dump resistor for this magnet is optimised. A range of resistances from 1 Ω to 10 Ω are considered. Here, the model is prepared in Symbols Sonata and compiled using the Boland compiler [126].

The magnet's hot spot temperature and current decay pattern are compared with OPERA FEA, a commercial solver [125]. Here, a 5Ω dump resistor is used for quench protection. Figure 6.9 shows the current decay, temperature rise, voltage rise and resistance growth in the magnet, as simulated by both methods.

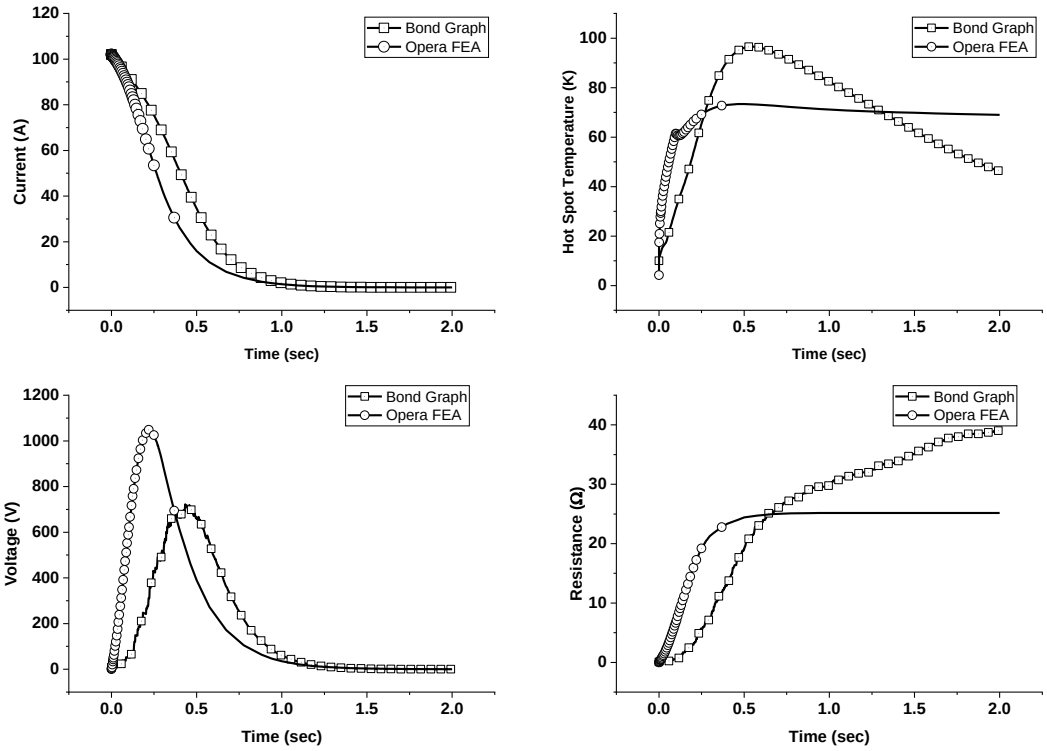

Figure 6.9 The current decay, hot spot temperature, voltage and resistance growth as simulated in a commercial simulation software OPERA FEA [75] compared to the developed bond graph model.

The current decay pattern obtained from the bond graph model agrees with the OPERA results. The hot spot temperature calculated via the bond graph is higher than that of calculated via OPERA, with a difference of ~10K. The hot spot temperature also shows a peak, which then slowly reduces back to a lower value. This variation originates from using a constant specific heat value instead of a temperature-dependent function. Due to the energy-based modelling approach of bond graphs, they natively don't allow a modulated capacitive element as thermal storage elements, [120], [127] which means the specific heat cannot be a function of temperature. So, instead, an average specific heat across the estimated operating temperature range is used. This means that during the initial period, the rise in temperature of individual lumps is slower than it is actually. This also means that the thermal conductivity is lower, which causes heat to accumulate at a point rather than spreading out faster to neighbouring cells. This peak temperature, however, reduces as time goes on since the energy is slowly conducted away to neighbouring cells. The peak voltage also shows a similar pattern, but the absolute values calculated have a difference of ~300V at its peak. Here, the voltage shown is a summation of both the resistive voltage (RI) and the impedance ($L\ \frac{di}{dt}$). As quench propagates, the resistive component of the voltage changes because of the increase in resistance and reduction in current. A combination of these two counterbalancing changes creates a peak voltage that is obtained, which then reduces it to zero.

The variation from the OPERA results can be accounted for mainly by two assumptions made in the bond graph model. Firstly, the bond graph model assumes heat transfer in two directions, azimuthal and axial, while assuming homogenous temperature in the radial direction. However, the FEA mesh-based approach used in OPERA also considers radial heat transfer. Secondly, a thermal capacitor element is described as having a temperature as a function of the integral of the heat flow and involving the constant specific heat. If the specific heat is assumed to be a function of the temperature, an algebraic loop is in play. This would create instability during simulation unless the variation of specific heat is minimal. One method to overcome this would be to use extremely small timesteps such that the variation of specific heat is small. Dynamic models, such as the Karnopp model [128] proposed for modelling coulomb friction or multiport ‘C’ elements, may also be implemented to overcome the instabilities.

Here, an average heat capacity over the operating temperature is considered instead of a temperature-dependent heat capacity. While this doesn't affect

the current decay directly, it can affect the growth of quenched volume. This is also seen in the coil resistance pattern, which initially follows the OPERA results, but while the Opera results quickly attain a constant value, the bond graph model takes much longer to achieve stability as the temperature rise of each lump at low temperatures (4K-10K) is not as fast as it should be. This is due to the assumption of average specific heat which is much higher than the specific heat of copper at 4K.

The results were also compared to the experimental results of the magnet. Figure 6.10 shows the temperature recorded by a temperature sensor compared to the results from the model. It may be noted that it is not practical to record the voltage and resistance growth of a magnet. Here, the temperature recorded by a temperature sensor embedded in the magnet is compared to the results of the bond graph model. It may be noted that the quench may not happen near the temperature sensor; thus, the recording received might not be the peak temperature within the coil.

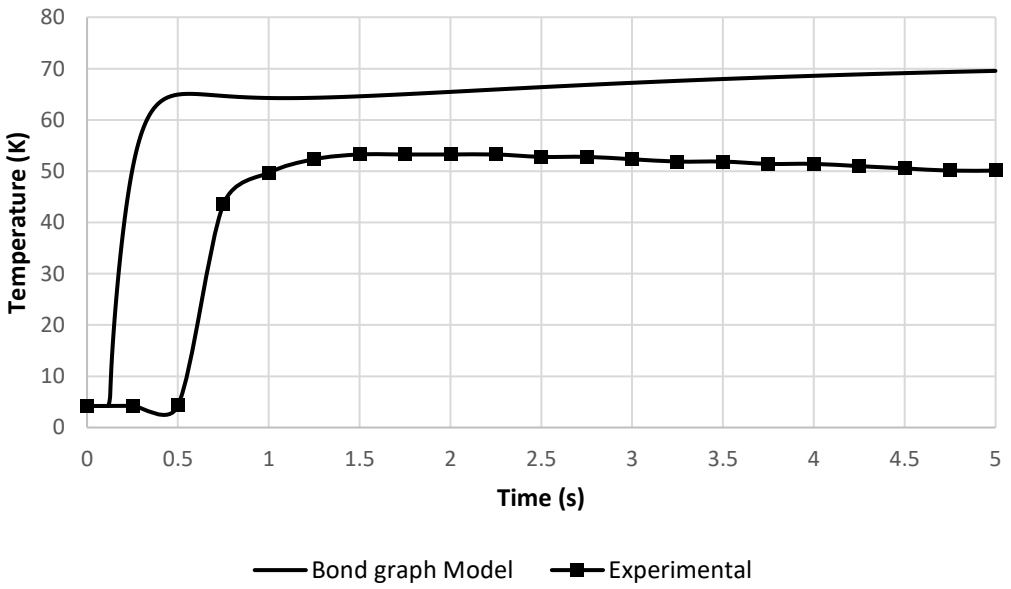

Figure 6.10 Comparison of the temperature rise at a point in the magnet measured during quench.

Using the same bond graph model, parameter optimisation for the value of the dump resistor is done. The results are given in Figure 6.11. The current decay becomes faster as the value of the dump resistor increases and the hot spot temperature also reduces. But this corresponds to a rise in the coil voltage. At low values of the dump resistor, the current decay time is constant since the coil resistance dominates the decay pattern. The same can be observed in the coil resistance plot, where higher

dump resistances remove a large amount of energy from the magnet, reducing the quenched volume and, thus, the coil resistance. In this case, a maximum allowable temperature of 100 K and a maximum voltage of 600 V are considered the safe operating limits [104], [129]. This is derived from the considerations of voltage breakdown of the wire insulation in the magnet and the avoidance of high-temperature gradients inside the magnet during the quench. Based on these limits, a dump resistance in the range of 4 Ω -6 Ω would be ideal for this magnet.

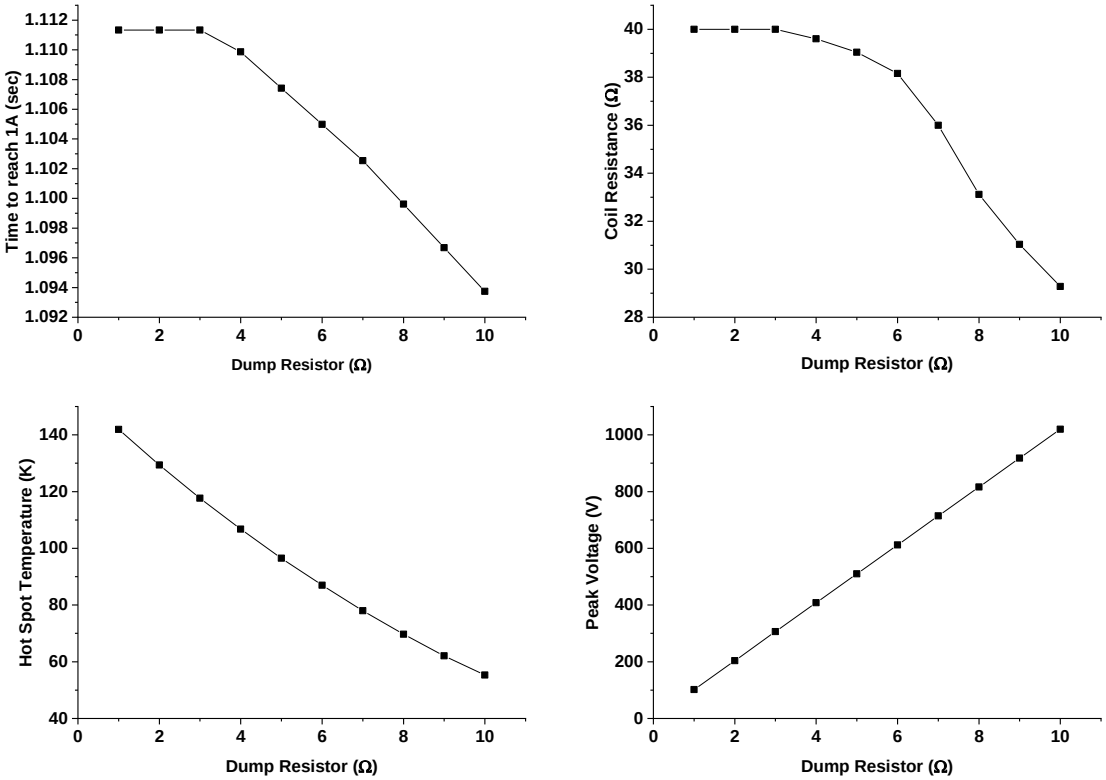

Figure 6.11 The variables, current decay time (from 102 A to 1 A), hot spot temperature, coil resistance, and peak voltage parametrised against various values of dump resistance.

6.5 Bond Graph Model for 1.5T MRI Magnet

Here, a model for the 1.5T MRI magnet is proposed. It uses the same concepts and the proposed bond graph model, but is adjusted to accommodate multiple coils. In order to model a 1.5T MRI multi-coil magnet, various instances of the same thermal model are being used, along with the associated electrical model. The MRI magnet consists of eight solenoid coils connected in series. Ideally, multiple coils connected in series electrically still act as a single coil, and in the bond graph, they

would be modelled as a single inductor. However, in order to simulate the coils individually and to find out the thermal behaviour of each coil, it is necessary to model each coil separately as an ideal inductor and resistor connected in series. This, however, poses a problem in bond graphs as such a configuration would cause one inductor in the set to have integral causality while the rest of the inductors will have differential causality. In order to avoid differential causality, 'pads' are introduced between each coil. In a physical sense, these pads represent the parasitic capacitance of each coil to its surroundings. This impendence, however, is very high and insignificant in the overall electrical design. In this case, the pads consist of a very high-value resistor (50 kΩ) placed in parallel with each coil. Due to the very high resistance of the pads, current will not flow through them, and they have a negligible effect on the circuit. These pads also allow for all the inductor elements to have integral causality. Proposed bond graph model for an eight-coil MRI magnet based on both electrical and thermal domains is shown in Figure 6.12.

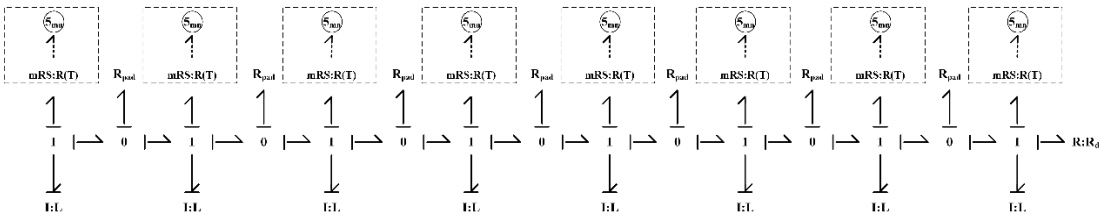

Figure 6.12 Proposed bond graph model for an eight-coil MRI magnet based on both electrical and thermal domains. Pads are added between each coil to electrically isolate the individual coils in bond graph.

While this model is proposed, the current restrictions on the student version of Symbols Sonata restrict solving the model. The commercial version of Symbols Sonata or a similar bond graph generation software, such as 20-sim, Simbus or PyPI may be used to simulate the MRI magnet bond graph model further.

6.6 Conclusion

The thermodynamic domain of a superconducting magnet can be modelled using various approaches. While a true bond graph would be the most ideal solution, a pseudo bond graph will provide various advantages over the true bond graph model. In a pseudo bond graph, the flow variable (f) will be the heat flow (Q), and the effort variable (e) will be temperature ($\underline{T}$).

A thermal bond graph of the superconducting magnet is developed based on lumped model and the electrical domain is modelled as a true bond graph. The model is used to simulate a 6T superconducting magnet and the results are compared to simulated results from OPERA FEA and with experimental results. Further a bond graph model for the whole MRI magnet is also proposed.

CHAPTER 7

CONCLUSIONS, FUTURE SCOPE AND SOCIAL IMPACT

This thesis presents a comprehensive investigation into the development, analysis, and performance evaluation of a 1.5 T active shielded superconducting MRI magnet. The research has addressed key aspects including magnet design, material properties, analytical modelling, force analysis, stress simulation, deformation analysis, and emergency shutdown/quench behaviour. Through rigorous theoretical frameworks and computational simulations, this study has contributed significant insights into the behaviour of the MRI magnet under various operational conditions.

The magnet design, consisting of an eight-coil solenoid configuration, has been developed to meet the requirements. The magnet operates at 420A current in persistent mode and generates 1.5 T centre magnetic with ±5.5 ppm homogeneity in 45 cm of diametrical spherical volume (DSV). One of the fundamental aspects explored in this research is the estimation of composite properties of the coil using a homogenization model based on the Representative Volume Element (RVE) approach. By characterizing properties such as Young's modulus, Poisson's ratio, and shear modulus across the entire operating temperature range (300K-4K), a deeper understanding of the mechanical behaviour of the magnet has been achieved.

Furthermore, an analytical model has been developed to calculate the Lorentz forces acting on the magnet, incorporating the magnetic field distribution calculation using the Elliptic integrals. At 420A, the magnet has a central field of 1.499 T and a peak field of 4.3T. Using the magnetic field values, the Lorentz force density of each coil is calculated as 2D planar state. The axisymmetric design of the magnet then enables the superimposition of the 2D forces to a 3D case. The net axial forces calculated for the magnet 151.5 kN, 330.6 kN, 543.7 kN, and -79.6 kN for coil 2, coil 4, coil 6 and coil 8, respectively. The results along with hoop stress values are compared to a commercial software for verification. This analysis has provided valuable insights into the forces exerted on each coil, enabling a comprehensive assessment of the mechanical stresses experienced by the magnet during operation.

The computational model developed to simulate operational stresses, considering both Lorentz forces and thermal cooldown, has enabled the determination of optimal winding parameters to mitigate the effects of these forces. In order to model the winding process, an APDL based Element Death and Birth method is incorporated to the computational model. By accurately modelling the winding process, parameters such as winding tension and the number of layers of over-bind have been optimized to ensure the structural integrity and performance stability of the magnet. Using the model, the winding tension, number of layers of over-bind, and the winding tension for the over bind are calculated. The parameters are designed so that they will counteract the effects of Lorentz forces and thermal cooldown. Based on the calculations, coil 2, coil 4, coil 6 and coil 8 were wound at 60 MPa, 50 MPa, 50 MPa and 60 MPa, respectively with 10, 10, 5 and 15 layers of over bind. The over binding was wound at 60 MPa tension for Coils 2, 4, and 6, while, for Coil 8 it was wound at 80 MPa.

Moreover, the study investigated the deformation of coils due to operational stresses, revealing implications on magnetic field homogeneity and centre field. Despite meticulous design and optimization efforts, it was observed that operational stresses lead to changes in magnetic field characteristics, necessitating further refinement in design and operational strategies. Due to the operational stresses, the magnet coils deform and the new magnet coordinates based on the deformations are studied. The magnetic field homogeneity deteriorated from ±5.5 ppm to ±278 ppm. The centre field also increased since the contraction of coils reduced the cross-section area increasing the current density of the coils. The central field changed from 1.4999 T to 1.506 T.

Finally, a bond graph-based model has been developed to analyse the magnet's behaviour during emergency shutdown/quench scenarios, considering both thermal and electrical domains. The model's predictions have been validated against commercial software and experimental data, demonstrating its efficacy in predicting critical parameters such as temperature and voltage during emergency situations. The model uses considered both the thermal and electrical domains of the operation. The model is used to simulate the operation of a 6T superconducting magnet and the results are compared to results from a commercial software and with experimental results. The model predicts a temperature of 98 K with a peak voltage of 700 V. The verified model then can be expanded to be used for other types of magnets and more complex quench protection circuits.

In conclusion, this thesis represents a significant contribution to the field of superconducting MRI magnet technology, providing valuable insights into design considerations, operational characteristics, and emergency response mechanisms. The findings presented herein pave the way for further advancements in magnet design, optimization, and operational strategies, ultimately enhancing the performance and reliability of superconducting MRI systems for medical imaging applications.

The research presented in this thesis opens avenues for future investigations and advancements in the field of superconducting MRI magnet technology. One promising direction for further research is the refinement of computational models to more accurately predict the behaviour of magnets under dynamic operating conditions, such as during rapid temperature changes during cooldown or various bobbin designs. Advanced numerical techniques, including finite element analysis and multi-physics simulations, can be employed to capture the complex interactions between mechanical, thermal, and electromagnetic phenomena within the magnet system.

In the realm of quench modelling for MRI magnets using bond graph methodology, there are several avenues for future exploration and refinement. One potential direction is the integration of more comprehensive thermal and electrical models within the bond graph framework to capture the dynamic behaviour of the magnet during quench events with greater fidelity. Incorporating detailed representations of heat transfer mechanisms, such as conduction, convection, and radiation, coupled with sophisticated electrical circuit models, can provide a more

nuanced understanding of the thermal and electrical dynamics governing the quench process.

Furthermore, future research could focus on the development of advanced control strategies and quench protection mechanisms based on insights gained from bond graph modelling. By leveraging real-time monitoring and feedback control systems, it may be possible to proactively detect and mitigate quench events, thereby enhancing the safety and reliability of superconducting MRI magnets. Additionally, exploring novel fault-tolerant designs and materials could mitigate the consequences of quench events, minimizing downtime and maintenance costs associated with magnet failures.

Overall, the integration of bond graph modelling with quench analysis holds promise for advancing the understanding and management of quench events in MRI magnets. Continued research in this area has the potential to yield innovative solutions for enhancing the performance, safety, and longevity of superconducting MRI systems, ultimately benefiting patients, healthcare providers, and researchers alike. The advancements in superconducting MRI magnet technology presented in this thesis have significant implications for healthcare and medical imaging. High-performance MRI systems play a crucial role in diagnosis, treatment planning, and monitoring of various medical conditions, ranging from neurological disorders to cancer. By improving the performance, reliability, and accessibility of MRI technology, this research contributes to enhancing the quality of healthcare delivery and patient outcomes. Moreover, the development of more efficient and cost-effective MRI systems has the potential to expand access to advanced medical imaging services, particularly in underserved communities and resource-limited settings, thereby promoting equity in healthcare access.

Furthermore, the research conducted in this thesis contributes to the broader advancement of science and engineering disciplines, fostering interdisciplinary collaborations and knowledge exchange. By pushing the boundaries of materials science, electromagnetics, and computational modelling, this work not only contributes to the development of state-of-the-art MRI technology but also lays the foundation for innovations in other fields, such as energy storage, transportation, and telecommunications. Ultimately, the societal impact of this research extends beyond the realm of healthcare, influencing various aspects of technology and society, and paving the way for a more sustainable and technologically advanced future.

REFERENCES

[1] C. Westbrook *et al.*, 2011, *MRI in Practice*, 4th ed. Wiley-Blackwell.

[2] M. Parizh *et al.*, 2017, "Conductors for commercial MRI magnets beyond Nb-Ti: requirements and challenges," *Superconductor Science and Technology*, vol. 30, no. 1, p. 014007,

[3] Y. Lvovsky and P. Jarvis, 2005, "Superconducting Systems for MRI—Present Solutions and New Trends," *IEEE Transactions on Applied Superconductivity*, vol. 15, no. 2, pp. 1317–1325,

[4] J. Jung and M. Abdelhadi, "Temperature Dependence of In-Plane Resistivity of Ybco," in *New Challenges in Superconductivity: Experimental Advances and Emerging Theories*, Berlin/Heidelberg: Springer-Verlag, 2005, pp. 79–84.

[5] P. Duthil, 2015, "Material Properties at Low Temperature," in *CAS-CERN Accelerator School: Superconductivity for Accelerators - Proceedings*, France: CERN-European Organization for Nuclear Research, pp. 77–95.

[6] A. Kushino *et al.*, 2008, "Development of Superconducting Coaxial Cables for Cryogenic Detectors," *Journal of Low Temperature Physics*, vol. 151, no. 3–4, pp. 650–654,

[7] P. J. Ray, "Structural investigation of La(2-x)Sr(x)CuO(4+y) - Following staging as a function of temperature," University of Copenhagen, 2015.

[8] O. Gingras, "La supraconductivité non-conventionnelle du ruthénate de strontium : corrélations électroniques et couplage spin-orbite," Universite de Montreal, 2022.

[9] R. G. Sharma, 2015, *Superconductivity: Basics and Applications to Magnets*, 1st ed., vol. 214. in Springer Series in Materials Science, vol. 214. Springer International Publishing.

[10] P. J. Lee, 2001, *Engineering superconductivity*. Wiley-Interscience.

[11] H. M. Paynter, 1961, *Analysis and design of engineering systems*. Boston, MA: MIT Press.

[12] D. Karnopp and R. C. Rosenberg, 1975, *Systems dynamics : a unified approach*. Wiley.

[13] D. C. Karnopp *et al.*, 2012, *System Dynamics*. Wiley.

[14] Jean U. Thoma, 1975, *Introduction to Bond Graphs and their Applications*, First Edit. Elsevier.

[15] J. J. Granda, 2002, "The role of bond graph modeling and simulation in mechatronics systems: An integrated software tool: CAMP-G, MATLAB–SIMULINK," *Mechatronics*, vol. 12, no. 9–10, pp. 1271–1295,

[16] A. Mukherjee *et al.*, 2012, *Bond Graph in Modeling, Simulation and Fault Identification*, Second Edi. Taylor & Francis.

[17] M. W. Garrett, 1963, "Calculation of Fields, Forces, and Mutual Inductances of Current Systems by Elliptic Integrals," *Journal of Applied Physics*, vol. 34, no. 9, pp. 2567–2573,

[18] Steven J . Sackett, 1975, "Calculation of electromagnetic fields and forces in coil systems of arbitrary geometry," *Sixth Symposium on Engineering Problems of Fusion Research*,

[19] D. Melville and P. G. Mattocks, 1972, “Stress calculations for high magnetic field coils,” *Journal of Physics D: Applied Physics*, vol. 5, no. 10, pp. 1745–1759,
[20] V. Arp, 1977, “Stresses in superconducting solenoids,” *Journal of Applied Physics*, vol. 48, no. 5, pp. 2026–2036,
[21] J. Caldwell, 1982, “Electromagnetic forces in high field magnet coils,” *Applied Mathematical Modelling*, vol. 6, no. 3, pp. 157–160,
[22] C. Minas and L. Salasoo, 1991, “Three-dimensional thermal stresses in a superconducting coil assembly,” *IEEE Transactions on Magnetics*, vol. 27, no. 2, pp. 2381–2383,
[23] D. G. Hawksworth *et al.*, 1987, “Considerations in the design of mri magnets with reduced stray fields,” *IEEE Transactions on Magnetics*, vol. 23, no. 2, pp. 1309–1314,
[24] F. J. Davies *et al.*, 1991, “A 2-tesla active shield magnet for whole body imaging and spectroscopy,” *IEEE Transactions on Magnetics*, vol. 27, no. 2, pp. 1677–1680,
[25] M. N. Wilson, 1982, *Superconducting Magnets*, 1st ed. Clarendon.
[26] E. D. Marquardt *et al.*, 2000, “Cryogenic Material Properties Database,” *11th International Cryocooler Conference*, vol. 12, no. 6, pp. 1–7,
[27] T. A. Brandsberg, 2004, “Calculating Smeared Material Properties for a SMES Magnet Coil,” in *International ANSYS Conference*, Pittsburgh, United States: ANSYS, Inc.
[28] J. Chen and X. Jiang, 2012, “Stress analysis of a 7 T actively shielded superconducting magnet for animal MRI,” *IEEE Transactions on Applied Superconductivity*, vol. 22, no. 3, pp. 4903104–4903104,
[29] A. Al Amin *et al.*, 2017, “Computational homogenization of the elastic and thermal properties of superconducting composite MgB 2 wire,” *Composite Structures*, vol. 188, pp. 313–329,
[30] A. Al Amin *et al.*, 2016, “A multiscale and multiphysics model of strain development in a 1.5 T MRI magnet designed with 36 filament composite MgB2superconducting wire,” *Superconductor Science and Technology*, vol. 29, no. 5, p. 055008,
[31] K. Pieterman and H. Postma, 1984, “A 1.5 t superconducting magnet with closed cooling system for spin-imaging: an outline,” *Cryogenics*, vol. 24, no. 2, pp. 59–62,
[32] K. Pieterman *et al.*, “Low Temperature Closed Cooling System for MRI Magnets,” in *Advances in Cryogenic Engineering*, Boston, MA: Springer US, 1986, pp. 533–541.
[33] Y. Iwasa, 1994, *Case Studies in Superconducting Magnets: Design and Operational Issues*, 2nd ed. Springer.
[34] Institute of Cryogenics and Superconductivity Technology, “MICE/MuCool Coupling Magnet Engineering Design,” China, 2008.
[35] L. Wang *et al.*, 2011, “Study on the mechanical instability of MICE coupling magnets,” *IEEE Transactions on Applied Superconductivity*, vol. 21, no. 3 PART 2, pp. 2363–2366,
[36] M. A. Green and S. Q. Yang, “The Coil and Support Structure Stress and Strain the MICE Focusing and Coupling Magnets,” 2004.

[37] L. Wang *et al.*, 2009, “Magnetic and cryogenic design of MICE coupling solenoid magnet system,” in *IEEE Transactions on Applied Superconductivity*, pp. 1344–1347.
[38] S. Q. Yang *et al.*, 2005, “The Mechanical and Thermal Design for the MICE Focusing Solenoid Magnet System,” *IEEE Transactions on Appiled Superconductivity*, vol. 15, no. 2, pp. 1259–1262,
[39] L. Wang *et al.*, 2008, “The engineering design of the 1.5 m diameter solenoid for the MICE RFCC modules,” *IEEE Transactions on Applied Superconductivity*, vol. 18, no. 2, pp. 937–940,
[40] T. Schild *et al.*, 2008, “The Iseult/Inumac Whole Body 11.7 T MRI Magnet Design,” *IEEE Transactions on Applied Superconductivity*, vol. 18, no. 2, pp. 904–907,
[41] T. Schild *et al.*, 2010, “The Iseult/Inumac Whole Body 11.7 T MRI Magnet R&D Program,” *IEEE Transactions on Applied Superconductivity*, vol. 20, no. 3, pp. 702–705,
[42] C. Berriaud *et al.*, 2010, “Conductor R&D for the Iseult/INUMAC Whole Body 11.7 T MRI Magnet,” *IEEE Transactions on Applied Superconductivity*, vol. 20, no. 3, pp. 1408–1411,
[43] C. Berriaud *et al.*, 2012, “Iseult/INUMAC 11.7 T Conductor Production Status,” *IEEE Transactions on Applied Superconductivity*, vol. 22, no. 3, pp. 6001104–6001104,
[44] H. Kanithi *et al.*, 2014, “Production Results of 11.75 Tesla Iseult/INUMAC MRI Conductor at Luvata,” *IEEE Transactions on Applied Superconductivity*, vol. 24, no. 3, pp. 1–4,
[45] T. Schild *et al.*, 2010, “The Iseult/Inumac Whole Body 11.7 T MRI Magnet R&D Program,” *IEEE Transactions on Applied Superconductivity*, vol. 20, no. 3, pp. 702–705,
[46] L. Quettier *et al.*, 2014, “Status of the Shielding Coil Fabrication for the Iseult/INUMAC Whole Body 11.75 T MRI Magnet,” *IEEE Transactions on Applied Superconductivity*, vol. 24, no. 3, pp. 1–4,
[47] L. Quettier *et al.*, 2015, “Status of the Shielding Coils Fabrication for the Iseult/INUMAC Whole Body 11.75 T MRI Magnet,” *IEEE Transactions on Applied Superconductivity*, vol. 25, no. 3, pp. 1–4,
[48] T. Schild *et al.*, 2016, “Iseult/INUMAC 11.7-T MRI Assembly Status,” *IEEE Transactions on Applied Superconductivity*, vol. 26, no. 4, pp. 1–4,
[49] L. Quettier *et al.*, 2016, “Expected Magnetic Field Quality From the Preliminary Measurements Performed During the Manufacturing of the Iseult/Inumac Whole-Body 11.7-T MRI Magnet,” *IEEE Transactions on Applied Superconductivity*, vol. 26, no. 4, pp. 1–4,
[50] L. Quettier *et al.*, 2018, “Manufacturing Completion of the Iseult Whole Body 11.7 T MRI System,” *IEEE Transactions on Applied Superconductivity*, vol. 28, no. 3, pp. 1–4,
[51] L. Li *et al.*, 2012, “Effect of pretension, support condition, and cool down on mechanical disturbance of superconducting coils,” *IEEE Transactions on Applied Superconductivity*, vol. 22, no. 2, pp. 3800104–3800104,

[52] Y. Li *et al.*, 2017, "Design of the superconducting magnet for 9.4 Tesla whole-body magnetic resonance imaging," *IOP Conference Series: Materials Science and Engineering*, vol. 171, no. 1, p. 012105,
[53] L. Li *et al.*, 2017, "Numerical Analysis of Mechanical Behavior for a 9.4-T Whole-Body MRI Magnet," *IEEE Transactions on Applied Superconductivity*, vol. 27, no. 4, pp. 1–5,
[54] Y. Dai *et al.*, 2012, "Structural design of a 9.4 T whole-body MRI superconducting magnet," *IEEE Transactions on Applied Superconductivity*, vol. 22, no. 3, pp. 4900404–4900404,
[55] H. Miyazaki *et al.*, 2016, "Design of a conduction-cooled 9.4 T REBCO magnet for whole-body MRI systems," *Superconductor Science and Technology*, vol. 29, no. 10, p. 104001,
[56] A. A. Amin *et al.*, 2017, "Mechanical Analysis of MgB2 Based Full Body MRI Coils under Different Winding Conditions," *IEEE Transactions on Applied Superconductivity*, vol. 27, no. 4, pp. 2–6,
[57] T. Baig *et al.*, 2014, "Conduction cooled magnet design for 1.5T, 3.0T and 7.0T MRI systems," *Superconductor Science and Technology*, vol. 27, no. 12, p. 125012,
[58] J. Overweg, 2006, "MRI main field magnets," in *Proceedings of the 14th ISMRM*,
[59] Y. Lvovsky *et al.*, 2013, "Novel technologies and configurations of superconducting magnets for MRI," *Superconductor Science and Technology*, vol. 26, no. 9, p. 093001,
[60] Yi Li *et al.*, 2012, "Quench Protection Design of a 1.5 T Superconducting MRI Magnet," *IEEE Transactions on Applied Superconductivity*, vol. 22, no. 3, pp. 4703604–4703604,
[61] Yi Li *et al.*, 2014, "A Passive Quench Protection Design for the 9.4 T MRI Superconducting Magnet," *IEEE Transactions on Applied Superconductivity*, vol. 24, no. 3, pp. 1–5,
[62] Y. Dai *et al.*, 2015, "Design Study on a 9.2-T Nb-Ti Superconducting Magnet With Long-Length Uniform Axial Field," *IEEE Transactions on Applied Superconductivity*, vol. 25, no. 3, pp. 1–4,
[63] R. J. Deissler *et al.*, 2017, "Numerical simulation of quench protection for a 1.5 T persistent mode MgB 2 conduction-cooled MRI magnet," *Superconductor Science and Technology*, vol. 30, no. 2, p. 025021,
[64] R. J. Deissler, 2016, "Variation in strain characteristics for multiscale multi-physics models of a 1 . 5T conduction cooled MRI system based ...," no. June, pp. 5–7.
[65] M. Maciejewski and B. Auchmann, 2017, "Port-Hamiltonian Description of Electro-Thermal Field-Circuit models," in *4th STEAM Collaboration Meeting*, Germany.
[66] M. Maciejewski *et al.*, 2015, "Automated lumped-element simulation framework for modelling of transient effects in superconducting magnets," in *2015 20th International Conference on Methods and Models in Automation and Robotics, MMAR 2015*, Institute of Electrical and Electronics Engineers Inc., pp. 840–845.

[67] E. Ravaioli *et al.*, 2016, “Lumped-Element Dynamic Electro-Thermal model of a superconducting magnet,” *Cryogenics*, vol. 80, pp. 346–356,
[68] J. D. Cockcroft, 1928, “The Design of Coils for the Production of Strong Magnetic Fields,” *Philosophical Transactions of the Royal Society of London. Series A*, vol. 227, pp. 317–343.
[69] G. B. Yntema, 1955, “Superconducting winding for electromagnets,” *Physical Review*, vol. 98, no. 4, pp. 1144–1209,
[70] F. Nunio *et al.*, 2010, “Mechanical Design of the Iseult 11.7 T Whole Body MRI Magnet,” *IEEE Transactions on Applied Superconductivity*, vol. 20, no. 3, pp. 760–763,
[71] W. Voigt, 1889, “Ueber die Beziehung zwischen den beiden Elasticitätsconstanten isotroper Körper,” *Annalen der Physik*, vol. 274, no. 12, pp. 573–587,
[72] A. Reuss, 1929, “Berechnung der Fließgrenze von Mischkristallen auf Grund der Plastizitätsbedingung für Einkristalle .,” *ZAMM - Journal of Applied Mathematics and Mechanics / Zeitschrift für Angewandte Mathematik und Mechanik*, vol. 9, no. 1, pp. 49–58,
[73] R. Hill, 1952, “The Elastic Behaviour of a Crystalline Aggregate,” *Proceedings of the Physical Society. Section A*, vol. 65, no. 5, p. 349,
[74] B. Paul, “PREDICTION OF ELASTIC CONSTANTS OF MULTIPHASE MATERIALS. Technical Report No. 3,” 1959.
[75] Z. Hashin *et al.*, 1962, “On some variational principles in anisotropic and nonhomogeneous elasticity,” *JMPSo*, vol. 10, no. 4, pp. 335–342,
[76] Z. Hashin and S. Shtrikman, 1962, “A variational approach to the theory of the elastic behaviour of polycrystals,” *Journal of the Mechanics and Physics of Solids*, vol. 10, no. 4, pp. 343–352,
[77] Z. Hashin and S. Shtrikman, 1963, “A variational approach to the theory of the elastic behaviour of multiphase materials,” *Journal of the Mechanics and Physics of Solids*, vol. 11, no. 2, pp. 127–140,
[78] J. F. W. Bishop and R. Hill, 1951, “XLVI. A theory of the plastic distortion of a polycrystalline aggregate under combined stresses.,” *The London, Edinburgh, and Dublin Philosophical Magazine and Journal of Science*, vol. 42, no. 327, pp. 414–427,
[79] J. F. W. Bishop and R. Hill, 1951, “CXXVIII. A theoretical derivation of the plastic properties of a polycrystalline face-centred metal,” *The London, Edinburgh, and Dublin Philosophical Magazine and Journal of Science*, vol. 42, no. 334, pp. 1298–1307,
[80] Q. I. Taylor, 1931, “The plastic distortion of metals,” *Philosophical Transactions of the Royal Society of London. Series A, Containing Papers of a Mathematical or Physical Character*, vol. 230, no. 681–693, pp. 323–362,
[81] Z. Hashin, “Theory of mechanical behavior of heterogeneous media,” 1963.
[82] R. A. Schapery, 1968, “Thermal Expansion Coefficients of Composite Materials Based on Energy Principles,” *http://dx.doi.org/10.1177/002199836800200308*, vol. 2, no. 3, pp. 380–404,
[83] V. M. Levin, 1967, *On the Coefficients of Thermal Expansion of Heterogeneous Materials*.

[84] R. Hill, 1964, “Theory of mechanical properties of fibre-strengthened materials: I. Elastic behaviour,” *Journal of the Mechanics and Physics of Solids*, vol. 12, no. 4, pp. 199–212,
[85] G. Dvorak, 2013, “Micromechanics of Composite Materials,” vol. 186,
[86] Y. Takao and M. Taya, 1985, “Thermal expansion coefficients and thermal stresses in an aligned short fiber composite with application to a short carbon fiber/aluminum,” *J. Appl. Mech*, vol. 52, no. 4, pp. 806–810.
[87] J. D. Eshelby, 1957, “The Determination of the Elastic Field of an Ellipsoidal Inclusion, and Related Problems,” *Proceedings of the Royal Society of London. Series A, Mathematical and Physical Sciences*, vol. 241, no. 1226, pp. 376–396.
[88] D. F. Adams, 1970, “Inelastic Analysis of a Unidirectional Composite Subjected to Transverse Normal Loading,” *Journal of Composite Materials*, vol. 4, no. 3, pp. 310–328,
[89] O. Pierard *et al.*, 2004, “Mean-field homogenization of multi-phase thermo-elastic composites: a general framework and its validation,” *Composites Science and Technology*, vol. 64, no. 10–11, pp. 1587–1603,
[90] D. P. Boso, 2013, “A simple and effective approach for thermo-mechanical modelling of composite superconducting wires,” *Superconductor Science and Technology*, vol. 26, no. 4, p. 045006,
[91] NIST Cryogenics Technologies Group, “Cryogenics Material Properties.” Accessed: Jul. 13, 2017. [Online]. Available: https://trc.nist.gov/cryogenics/materials/materialproperties.htm
[92] J. W. Ekin, 2006, *Experimental techniques for low-temperature measurements. Cryostat desgn, material properties and superconductor critical current testing*. Oxford University Press.
[93] N. J. Simon *et al.*, “Properties of Copper and Copper Alloys at Cryogenic Temperatures, NIST Monograph 177,” 1992.
[94] L. Wang *et al.*, 2018, “The Effect of Winding Conditions on the Stress Distribution in a 10.7 T REBCO Insert for the 25.7 T Superconducting Magnet,” *IEEE Transactions on Applied Superconductivity*, vol. 28, no. 3,
[95] M. A. Ranney and G. Fujii, 1981, “The thermal expansion of several materials for superconducting magnets,” *IEEE Transactions on Magnetics*, vol. 17, no. 5, pp. 2316–2319,
[96] N. Bagrets *et al.*, 2015, “Thermal and mechanical properties of advanced impregnation materials for HTS cables and coils,” *IOP Conference Series: Materials Science and Engineering*, vol. 102, no. 1, p. 012021,
[97] O. Taylor *et al.*, 2024, “Characterization of the Mechanical and Thermal Properties, Including Fracture Toughness, of Epoxy Resin System DGEBA, POPDA (D400),” *IEEE Transactions on Applied Superconductivity*, vol. 34, no. 5, pp. 1–5,
[98] V. Mallick, 1989, *Stress Analysis of Metal/Cfrp Adhesive Joints Subjected To the Effects of Thermal Stress*. University of Bristol.
[99] A. Brem *et al.*, 2021, “Elasticity, plasticity and fracture toughness at ambient and cryogenic temperatures of epoxy systems used for the impregnation of high-field superconducting magnets,” *Cryogenics*, vol. 115, p. 103260,

[100] Y. Wang and Z. Jing, 2023, “Multiscale Modelling and Numerical Homogenization of the Coupled Multiphysical Behaviors of High-Field High Temperature Superconducting magnets,” *Composite Structures*, p. 116863,
[101] A. Sharma *et al.*, “Estimation and Experimental Validation of Mean-Field Homogenised Effective Properties of Composite”,
[102] F. Giorgetti, “An Integrated Multi-Physics Tool for the Mechanical Analysis of Fusion Reactors Superconducting Magnets,” UNIVERSITY OF ROME “TOR VERGATA,” 2018.
[103] D. B. Montgomery and J. Terrell, “Some Useful Information for the Design of Air-Core Solenoids (AFOSR-1525),” Massachusetts, 1961.
[104] Soumen Kar, “Electro-Thermal Characterization of Cryogen-Free Superconducting (LTS) Magnet System,” (PhD Thesis) Jawaharlal Nehru University, 2016.
[105] M. W. Garrett, 1951, “Axially symmetric systems for generating and measuring magnetic fields. Part I,” *Journal of Applied Physics*, vol. 22, no. 9, pp. 1091–1107,
[106] B. Breneman, “History, Physics, and Design of Superconducting Magnets for MRI,” pp. 137–156,
[107] B. Breneman, “Magnet Field Shimming and External Ferromagnetic Influences on the Homogeneity and Site Shielding of Superconducting MRI Magnets,” pp. 175–190,
[108] H. Rajainmaki *et al.*, 2013, “The electrical insulation of large superconducting magnets,” *IEEE Transactions on Applied Superconductivity*, vol. 23, no. 3,
[109] M. Evangelos Biancolini *et al.*, 2018, “Mechanical Analysis of the ENEA TF Coil Proposal for the EU DEMO Fusion Reactor,” *IEEE Transactions on Applied Superconductivity*, vol. 28, no. 4, pp. 1–5,
[110] 2019, *Opera-3d Reference Manual*, 19th ed. Dassault Systèmes UK Ltd.
[111] A. Al Amin *et al.*, 2016, “A multiscale and multiphysics model of strain development in a 1.5 T MRI magnet designed with 36 filament composite MgB2 superconducting wire,” *Superconductor Science and Technology*, vol. 29, no. 5, p. 055008,
[112] Y.-H. Zhou *et al.*, 2023, “Review on Progresses and Challenges of Key Mechanical Issues in High-Field Superconducting Magnets,” *National Science Review*,
[113] P. Heng *et al.*, 2010, “Effect of Conductor Winding Pre-stress on stresses in Cold Mass Assembly of MICE Coupling Magnet,” *Atomic Energy Science and Technology*, vol. 44, no. 5, pp. 611–616.
[114] J. W. Ekin *et al.*, 1977, “Effect of Stress on the Critical Current of Nb-Ti Multifilamentary Composite Wire,” *Advances in Cryogenic Engineering*, pp. 449–452,
[115] K. L. Kim *et al.*, 2014, “Effect of Winding Tension on Electrical Behaviors of a No-Insulation ReBCO Pancake Coil,” *IEEE transactions on applied superconductivity : a publication of the IEEE Superconductivity Committee*, vol. 24, no. 3,
[116] H. Brice *et al.*, 2012, “Frictional Behavior of Material Couples in Superconducting MRI Magnet Systems at 4.2 K,” *IEEE Transactions on Applied Superconductivity*, vol. 22, no. 3, pp. 4400204–4400204,

[117] Cobham Technical Services, 2016, *Opera-3d User Guide*, 18R2 ed.
[118] Y. Lvovsky *et al.*, 2013, "Novel technologies and configurations of superconducting magnets for MRI," *Superconductor Science and Technology*, vol. 26, no. 9, p. 093001,
[119] A. Nakrachi and G. Dauphin-Tanguy, 2003, "A Distributed Parameter Pseudo Bond Graph for Heat Conduction Modelling: Notion of Cellular Bond Graph," in *Dynamic Systems and Control, Volumes 1 and 2*, ASMEDC, pp. 911–916.
[120] D. Karnopp, 1978, "Pseudo Bond Graphs for Thermal Energy Transport," *Journal of Dynamic Systems, Measurement, and Control*, vol. 100, no. 3, pp. 165–169,
[121] G. Janevska, 2017, "Bond Graphs Approach to Modeling Thermal Processes," *International Journal of Scientific & Engineering Research*, vol. 8, no. 5, pp. 736–740,
[122] Arun Kumar Samantaray and Belkacem Ould Bouamama, "Bond Graph Modeling in Process Engineering," in *Model-based Process Supervision*, no. 9781848001589, in Advances in Industrial Control. , London: Springer London, 2008, pp. 13–80.
[123] D. L. Margolis, 1985, "A survey of bond graph modelling for interacting lumped and distributed systems," *Journal of the Franklin Institute*, vol. 319, no. 1–2, pp. 125–135,
[124] F. T. Brown, 2010, "Bond-Graph Based Simulation of Thermodynamic Models," *Journal of Dynamic Systems, Measurement, and Control*, vol. 132, no. 6,
[125] S. Kar *et al.*, 2015, "Quench characteristics of 6 T conduction-cooled Nb-Ti magnet system," *IOP Conference Series: Materials Science and Engineering*, vol. 101, no. 1, p. 012077,
[126] Arun Kumar Samantaray, "Symbols Sonata Academic Version." 2005.
[127] L. S. P. S. Smith, "Bond Graph Modelling Of Physical Systems," Glasgow University, 1993.
[128] D. Karnopp, 1985, "Computer Simulation of Stick-Slip Friction in Mechanical Dynamic Systems," *Journal of Dynamic Systems, Measurement, and Control*, vol. 107, no. 1, pp. 100–103,
[129] Y. Wang, 2014, *Fundamental elements of applied superconductivity in electrical engineering*, 1st ed. Wiley.

PLAGIARISM REPORT

Title of the Thesis: Multiphysics Modelling of Operational Stresses in a 1.5 T Superconducting Magnet for Whole-Body Clinical MRI Scanner

Total Pages: 151 **Name of the Scholar:** Sankar Ram T

Supervisors:

1) Prof. Vijay Gautam
2) Dr. Soumen Kar

Department: Mechanical Engineering

This is to report that the above thesis was scanned for similarity detection. The process and outcome are given below:

Software used: Turnitin **Similarity Index:** 8% **Total word count:** 30744

Date:

Candidate's Signature **Signature of Supervisor(s)**